Investigation of the Electronic Structure of Transition Metal-Ions in Solution from Aqua-Complexes to Porphyrins

Inaugural-Dissertation
to obtain the academic degree
Doctor rerum naturalium (Dr. rer. nat.)

submitted to the Department of Biology, Chemistry and Pharmacy
of Freie Universität Berlin

by
Ronny Golnak

Berlin, Germany
November 2015

Thesis written under supervision of

Prof. Dr. Emad F. Aziz

@

Helmholtz-Zentrum Berlin für Materialien und Energie (HZB)

Institute of Methods for Material Development (EM-IMM)

December 2012 - November 2015

1.	Gutachter:	Prof. Dr. rer. nat. Emad F. Aziz
		Freie Universität Berlin
2.	Gutachter:	Prof. Dr. Ing. Christina Roth
		Freie Universität Berlin

Eingereicht: 26. November 2015

Disputation: 10. Februar 2016

Abstract

This thesis reports how, by the development of the vacuum liquid micro-jet technique as well as the flow cell technique for soft X-ray spectroscopy, electronic structure measurements on liquid have advanced to date. My focus is on investigations of solvated transition metals in both simple and complex systems. These transition metal systems are at the heart of current research activities world-wide, in fields including physical chemistry and biology, and aiming at a molecular level to the understanding of the interactions of metal-ligand and metal-solvent. For the transition metal aqueous solutions (simple system) I have systematically compared all possible decay channels upon resonant excitation at the Fe L-edge, including radiative fluorescence yield and non-radiative electron yield both for valence and core-level emissions, in order to discover an undistorted detection method for XAS measurements. Our analysis suggests a new protocol for investigation of X-ray spectra and its implications for the study of transition metal solute-solvent electronic interactions, being important to promote our understanding of the geometric and electronic structure and the rational design of catalytic and functional materials. For complex systems the local electronic structure of hemin has been investigated first by X-ray absorption and emission spectroscopy at the Fe L-edge and N K-edge. The study was performed for hemin in aqueous solution where dimerization occurs and in organic solution where the molecule remains monomer. A local energy gap at the Fe sites was observed for the hemin dimer, with the occupied valence states shifted to lower binding energies, while the unoccupied valence states share the same energies as the hemin monomer. In addition, solute-solvent electronic structure interactions of porphyrin at very low concentrations in liquid solution are presented. For Mn-tetraphenylporphyrin chloride and Mn-octaethylporphyrin chloride distinctive spectral features of metal-to-ligand charge-transfer were observed, when characterized by resonant inelastic X-ray scattering at the Mn L-edge and N K-edge. In the case of Fe-octaethylporphyrin chloride and Fe-tetraphenylporphyrin chloride, it is argued that the Fe center of the Fe octaethylporphyrin is more capable of binding small solvent molecules, than the tetraphenylporphyrin complex in solution. The proposed binding mechanism is through the assistance of the dipole interaction between the porphyrin-ligand system and the solvent molecule, in a situation where the ligand structure and arrangement maximize the binding interactions. Our studies demonstrate that even small ligands, depending on their structure and arrangement, can have considerable effects on the porphyrin metal center chemistry in liquid solution. All studies at the porphyrin complexes are accompanied by the interpretation of density functional theory with restricted open-shell configuration interaction singles (DFT/ROCIS) calculations.

Zusammenfassung

Die vorliegenden, im Rahmen meiner Doktorarbeit durchgeführten Untersuchungen zeigen, wie sich die Röntgenspektroskopie im weichen Röntgenbereich zur Analyse der elektronischen Struktur in Lösung, mittels Mikroflüssigkeitsstrahl und Durchflusszelle im Vakuum, weiterentwickelt hat. Der Fokus meiner Untersuchungen liegt auf gelöste Übergangsmetall-systeme mit sowohl einfachem als auch komplexerem Aufbau. Diese Komplexe sind Gegenstand aktueller, weltweiter wissenschaftlicher Forschungsfelder, wie der physikalischen Chemie und der Biologie. Bei den relativ einfach aufgebauten Übergansmetall-Wasser-Komplexen in Lösung, erfolgte ein systematischer Vergleich sämtlicher elektronischer Wechselwirkungsprozesse, ausgelöst durch resonante Anregung an der Eisen L-Kante. Der Vergleich basiert auf Messungen mittels partieller Fluoreszenzausbeute- und Elektronenausbeutetechniken. Das Ziel ist es, eine Detektionsmethode zu etablieren, die ein störungsfreies Röntgenabsorptionsspektrum (XAS) liefert. Unsere Ergebnisse sind bedeutend für die Interpretation von Röntgenspektren und fördern das Verständnis von elektronischen Wechselwirkungen zwischen den gelösten Komplexen und dem umgebenden Lösungsmittel in katalytischen und funktionalen Materialien. Als komplexeres System wurde zuerst die elektronische Struktur von Hemin in Lösung mittels XAS und XES an der Eisen L-Kante sowie der Stickstoff K-Kante untersucht. Dabei wurde das Molekül als Dimer in wässriger Lösung und als Monomer in organischer Lösung (DMSO) analysiert und verglichen. Für das Dimer wurde eine Energielücke in Valenzzuständen gefunden, wobei die besetzten Valenzzustände zu niedrigeren Energien verschoben sind, während die unbesetzten Valenzzustände die gleichen Energien wie das Monomer des Hemins aufweisen. Zusätzlich werden die Solvat-Solvens-Wechselwirkungen in der elektronischen Struktur von weiteren Porphyrinen bei niedrigen Konzentrationen in Dichlormethan vorgestellt. Die Charakterisierung mittels resonanter unelastischer Röntgenstreuung an der Mangan L-Kante und der Stickstoff K-Kante liefert markante spektrale Kennzeichen für Metall-zu-Liganden-Ladungstransfer in Tetraphenyl- und Oktaethylporphyrinen des Mn(III). Im Fall von Tetraphenyl- und Oktaethyl-porphyrin des Fe(III) tritt eine Interaktion mit den Lösemittelmolekülen auf, welche für den Oktaethylkomplex stärker ausfällt. Der vorgeschlagene Bindungsmechanismus wird dabei von Dipolwechselwirkungen des Porphyrinsystems und den Lösemittelmolekülen gesteuert, wobei die sterische Anordnung der Alkylgruppen des Porphyrins diesen Vorgang begünstigt. Unsere Untersuchungen zeigen somit, dass bereits die Variation in kleinen funktionellen Gruppen des Porphyrinliganden einen messbaren Effekt auf die elektronische Struktur des Metallzentrums in Lösung haben kann. Sämtliche Untersuchungen an Porphyrinen wurden durch die Auswertung theoretischer Berechnungen (DFT/ROCIS) begleitet.

Acknowledgements

It is of general consensus that success of a PhD thesis is not the result of the work of a single person. Many people have contributed to the work presented in my thesis and I feel deeply thankful to all of them. In first place I would like to express my gratitude to my PhD supervisor *Prof. Dr. Emad Flear Aziz* for the strong mentoring and opportunity to develop my scientific career within his group. My work is supported by *Prof. Dr.-Ing. Christina Roth* as well and I would like to thank her for following up my scientific research.

I have still not found the appropriate words to acknowledge my "direct boss" *Dr. Jie Xiao*. With his friendly and easygoing way we have managed to successfully accomplish multiple beamtimes which in the end resulted in my own thesis. Thanks for the inspiration, for the example of successful scientist, for the discussions, for teaching me how to plan and do X-ray experiments, for correcting my manuscripts.

Some special thanks go to *Dr. Kaan Atak*. He is my long-standing companion in the work group. I would like to thank him for the warm discussions, the criticisms, the plenty of time he offered me and for all the support for articles and theoretical calculations.

I am very happy that *Dr. Bernd Winter* joined our work group, without him my experimental experience on liquid would never be extended to PES. I especially want to thank him for the heavy scientific impact upon combination of RPES with RIXS. It was a pleasure to me to work with him and his team, including *Dr. Robert Seidel*, *Dr. Stephan Thürmer* and *Isaak Unger*. These guys were my dear fellow teammates.

Thanks and greetings to the team members who supported me for beamtimes, like *Dr. Antje Neubauer*, *Marvin Pohl*, *Mika Pflüger*, *Munirah Khan*, *Christoph Schwanke* and *Tim Brandenburg* (especially for our exciting beamtime in Japan). I also thank the guys from our laser lab *Alexander Kothe*, *Jan Metje*, *Nicholas Engel*, *Mario Borgwardt* and *Martin Wilke*.

I would like to thank *Prof. Dr. Sven Schröder*, *Dr. Joanna Stevens* and *Adrian Gainar* for the positive collaboration on investigating organic solutes and the hemin N K-edge. In addition I am also grateful for the input of *Prof. Dr. Oliver Kühn* and *Dr. Sergey Bokarev* in our joint analysis of radiative and non-radiative electronic relaxation. Thanks and greetings to *Dr. Julia Melke*, *Igor Derr* and *Joachim Langner* for the great beamtime of measuring the vanadium electrolytes.

Many Thanks to my new teammates *Dr. Marc Tesch* and *Daniela Schön*. I will never forget how we assembled LiXEdrom 2.0 and conducted first experiments - thanks for teaming up with me.

Publication List

Parts of this thesis have been published or submitted as the following articles:

1. Ronny Golnak, Jie Xiao, Kaan Atak, Isaak Unger, Rober Seidel, Bernd Winter, Emad F. Aziz. **Undistorted X-ray Absorption Spectrum Probed by a Core-level Secondary Emission.** *J. Phys. Chem. A (2016),* DOI:10.1021/acs.jpca.6b01699

   Chapter 3.1

2. Ronny Golnak, Sergey I. Bokarev, Robert Seidel, Jie Xiao, Gilbert Grell, Kaan Atak, Isaak Unger, Stephan Thürmer, Saadullah G. Aziz, Oliver Kühn, Bernd Winter, Emad F. Aziz. **Joint Analysis of Radiative and Non-Radiative Electronic Relaxation Upon X-ray Irradiation of Transition Metal Aqueous Solutions.** *Scientific Reports (2016),* DOI:10.1038/srep24659

   Chapter 3.2

3. Kaan Atak, Ronny Golnak, Jie Xiao, Edlira Suljoti, Mika Pflüger, Tim Brandenburg, Bernd Winter, Emad F. Aziz. **Electronic Structure of Hemin in Solution Studied by Resonant X-ray Emission Spectroscopy and Electronic Structure Calculations**. *J. Phys.Chem. B (2014),* DOI:10.1021/jp505129m

   Chapter 4.1.1

4. Kaan Atak, Ronny Golnak, Jie Xiao, Mika Pflüger, Tim Brandenburg, Bernd Winter, Emad F. Aziz. **Co(III) protoporphyrin IX chloride in solution: Spin-state and metal coordination revealed from resonant inelastic X-ray scattering and electronic structure calculations.** *Phys. Chem. Chem. Phys. (2014),* DOI:10.1039/C4CP04703F

   Chapter 4.1.2

5. Ronny Golnak, Jie Xiao, Kaan Atak, Munirah Khan, Edlira Suljoti, Emad F. Aziz. **Local Energy Gap Opening Induced by Hemin Dimerization in Aqueous Solution.** *J. Phys. Chem. B (2015),* DOI:10.1021/jp509966q

   Chapter 4.2.1

6. Ronny Golnak, Jie Xiao, Kaan Atak, Joanna S. Stevens, Adrian Gainar, Sven L. M. Schröder, Emad F. Aziz. **Intermolecular Bonding of Hemin in Solution and in Solid State Probed by N K-edge X-ray Spectroscopies.** *Phys. Chem. Chem. Phys. (2015),* DOI:10.1039/C5CP04529K

   Chapter 4.2.2

7. Ronny Golnak, Jie Xiao, Marvin Pohl, Christoph Schwanke, Antje Neubauer, Kathrin M. Lange, Kaan Atak, Emad F. Aziz. **Influence of outer ligands on metal-to-ligand charge-transfer in solvated Mn porphyrins.** *Inorg. Chem. (2016),* DOI:10.1021/acs.inorgchem.5b01585

   Chapter 4.3.1

8. Jie Xiao, Ronny Golnak, Kaan Atak, Mika Pflüger, Marvin Pohl, Edlira Suljoti, Bernd Winter, Emad F. Aziz. **The Assistance of the Iron Porphyrin Ligands to the Binding Interaction between the Fe Center and Small Molecules in Solution**. *J. Phys.Chem. B (2014),* DOI:10.1021/jp5023339

   Chapter 4.3.2

Content

1 Introduction

Huge efforts have been made in science during the last centuries discovering the secrets of the microscopic world of atoms that determines the macroscopic shape of nature. One substantial step was the discovery of X-rays by Wilhelm Conrad Röntgen in 1895 [1,2]. Since then many structure-sensitive methods have been developed and applied. With these methods it was possible to reveal the microscopic characteristics that are inaccessible by human senses. The knowledge of electronic and geometric structure is of fundamental relevance towards a full understanding of nature. It is therefore important for all aspects in biology, chemistry and physics. Regardless, whether the system is represented by a relatively small molecule like water or by a complex macromolecule like a protein, its function is specified by its composition. The Nobel Prize laureate Francis Harry Compton Crick once said: "If you want to understand function, study structure" [3,4]. More than 400 years ago John Donne and Sir Walter Raleigh wondered: Why is grass green? Why not blue or violet? And why is blood red? These questions remained unanswered for nearly three centuries. Today, we know that the color of grass and blood depends on one class of chemical compounds - porphyrins which derives from the Greek word *porphyra* (meaning purple). The discovery of porphyrins as important building block of life results in the development of the porphyrin chemistry, an important field in the organic chemistry. Since then an interdisciplinary field of research is developing, which connects scientist from multiple areas [5]. Many Studies revealed that porphyrins show strong potential for applications as sensors [6], as catalysts for CO_2 reduction [7], in organic solar cells [8–10], in catalytic solar water splitting [11] and in cancer therapy [12].

In this thesis I focus first on investigations of solvated transition metal ions to gain understanding of the interactions of metal-ligand and metal-solvent. For iron aqueous solutions I have conducted a systematical analysis on the local electronic structure of iron. Our analysis suggests a new protocol for investigation of X-ray spectra and its implications for the study of transition metal solute-solvent electronic interactions, being important to promote our understanding of the geometric and electronic structure and the rational design of catalytic and functional materials. In a second part of my thesis I present my investigations on more complex systems. The local electronic structure of various porphyrins has been investigated by X-ray absorption and emission spectroscopy.

1.1 Porphyrins Role in Nature

In nature the porphyrin systems play a major role as chromophores in a variety of protein complexes. All porphyrins and their derivatives represent highly effective ligands and can bound to many (transition) metals forming complexes and provide a huge diversity of functionality to organisms. Iron porphyrins are often the active centers in many vital proteins, such as cytochromes, peroxidases and oxidoreductases and are involved in the oxygen transport and storage inside cells [13]. Nickel as central atom can be found in methanogens, while cobalt is a vital ingredient in cobalamin (vitamin B_{12}) and its structural derivatives [13]. Magnesium porphyrins act as reaction centers in light harvesting complexes for photosynthesis [13]. Many porphyrin complexes with identical metal centers have distinctive functions, indicating significant roles played by porphyrin ligands. Investigations upon pigment-protein-complexes *in vivo* demonstrated that the chemical environment of porphyrin molecules has a significant impact on the functionality of the chromophores [14]. Proteins perform most of the works in living systems. More than one quarter of all known proteins are metalloproteins, i.e. proteins with embedded metal ions [16]. Metalloproteins participate actively in electron storage and transfer processes, dioxygen binding, storage and activation, and charge transport and catalysis in many biological processes. Many of these activities have to do with the properties of the porphyrin metal centers. Understanding of protein functions with predictive power will advance fields from biology to medicine and bioengineering. Simple protein models are often applied to study fundamental processes. Metalloproteins catalyze reactions in a highly effective way at their active center. This is the reason why they are in the focus of a broad range of spectroscopic investigations. To fully understand the function of these proteins it is necessary to reveal their electronic configuration and atomic compositions under realistic conditions.

Several analytical methods have been applied so far, in which X-ray crystallography is one of the popular spectroscopic methods for structure determination [17]. In 1958 John Cowdery Kendrew succeeded in revealing the protein structure of Myoglobin, wherefore he was granted the Nobel Prize of chemistry in 1962 [18,19]. More investigations followed to reveal structures and effectiveness of these catalysts [13,20]. Figure 1 presents a three-dimensional structure of myoglobin, which was discovered via X-ray crystallography. This analytical method needs a crystalline form of bio-macromolecule. If the protein cannot be crystallized into a periodic structure X-ray diffraction analysis is not feasible.

The same limitation applies for electron or neutron diffraction. Moreover, a crystalline form differs notably from the one in physiological condition (e.g. different pH value, phase, temperature, pressure, etc.) at which the catalytic activity is performed. Additional methods are thus needed to explore amorphous organic molecules under realistic conditions.

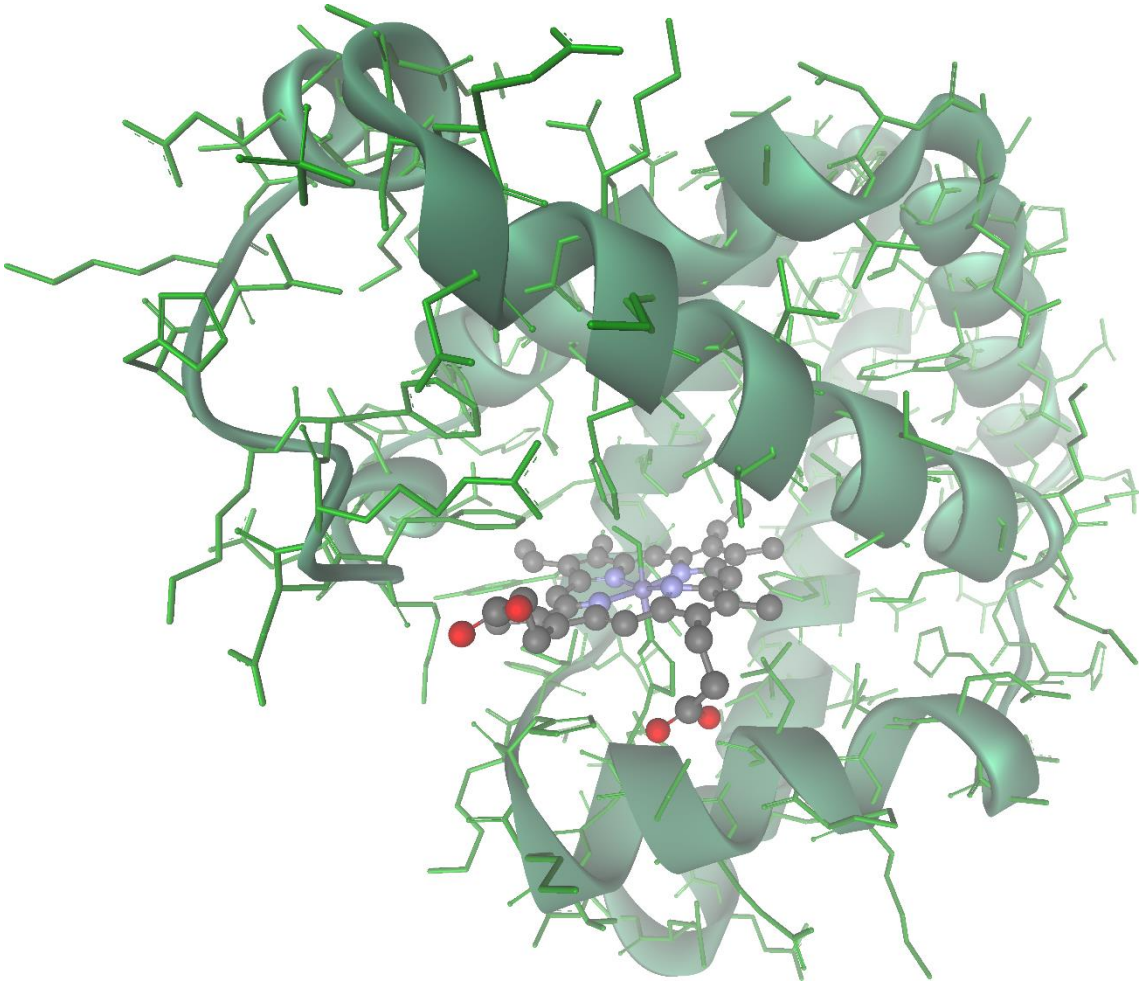

Figure 1. Three-dimensional picture of myoglobin, created by the data set 1MBO from the protein data base [15]. The protein contains a porphyrin complex with an iron center (heme) as a prosthetic group.

1.2 The Study of Solvated Porphyrins

One of the major characters of porphyrins is their chromaticity. Already in 1883 Jacques-Louis Soret found an intensive absorption band around 400 nm wavelength for hemoglobin [21]. This band is typical for all tetrapyrroles with conjugated ring systems. Between 480 and 700 nm wavelength another two to four bands are present. These bands contain information about the kind of substitution and possible central atoms. Another specific characteristic of porphyrins is the high melting point (around 300 °C) and the

very low solubility in organic solvents when compared to other organic compounds. This is due to the big aromatic system hindering the formation of solvation shell, combined with the tendency of self-organization into a stacking formation. Multiple methods for the characterization of organic compounds have been applied for porphyrins, such as NMR-spectroscopy [22,23] and X-ray diffraction [24]. More than 2500 tetrapyrroles were analyzed and one came to the conclusion that the porphyrins do not belong to the typical aromatic systems and should be regarded as chemical compounds with an exceptional position/-rank/-class according to their constitution. Influence of conformation is inherent upon chemical reactivity and physicochemical properties for tetrapyrroles [25–28]. Conformation can be effected by substitutes, central metal axial ligands and protein conditions in biological relevant macromolecules.

X-ray spectroscopy is an ideal tool for probing element-specific electronic structure. Recent developments in the vacuum liquid-microjet technique have extended the applicability of soft X-ray spectroscopy to highly volatile liquid solutions. This technique offers *in situ* access to the electronic structure of atomic and molecular solutes. Hence, solute-solvent interactions as well as short-lived chemically reactive intermediates produced upon X-ray excitation or ionization can be studied in great detail [29–32]. Among the prominent applications is the investigation of aqueous transition-metal (TM) ions, in particular iron-water complexes, which play a key role in biological and physical-chemical processes [33–39]. Numerous proteins contain metalloporphyrins as functional groups, with transition metals in the porphyrin-ring center, allowing for a wide range of biological functions. The latter include oxygen storage and transport (hemoglobin and myoglobin), electron transport (cytochrome oxidase), and energy conversion (chlorophyll), demonstrating photosensitive and catalytic properties [5,40–42]. Porphyrin studies also extend to applications in the activation of human immunodeficiency virus [43]. Due to the diversity of their functions, metalloproteins remain subject of current spectroscopic investigations, porphyrin research continues to be an active field, and there is a focus on the configurational details, bonding, and spin states of the metal center [40,44]. A startling feature of biological iron (such as in ferri-hemoglobin or ferri-myoglobin) is its flexibility and adaptability of electronic properties which is less common in inorganic iron complexes. This unique feature originates from the small energy differences between different spin-state configurations [40,44,45]. There is a strong correlation between molecular geometric structure and spin state, and the N-Fe-N bond angle is found to be dependent

on the spin multiplicity of these porphyrin complexes [45]. Depending on the chemical environment, different spin states can coexist, and additionally the spin state may change (spin crossover) [46] as a function of ligand coordination [47]. Understanding these mechanisms is extremely important for unraveling the transport properties of these biomolecules [41]. For a description of the local electronic structure governing these properties, the orbital mixing between the transition metal ion and the surrounding porphyrin ligand has to be investigated. From the experimental side, soft-X-ray spectroscopy is ideally suited for this purpose, providing an unprecedented sensitivity to local electronic structure, and is applicable for in situ investigations [48,49]. At the core of the functionality of Metalloporphyrin systems lie the fast electron dynamics and efficient energy transfer between the transition metal center and its coordinated nitrogen ligands determining the efficiency of various chemicals, including catalytical reaction [42,50]. Charge transfer (CT), in the form of metal-to-ligand (MLCT) or ligand-to-metal (LMCT), is mediated by the metal-ligand orbital mixing (chemical bond) that binds the metal center and its N ligands [47,50–53]. Therefore, understanding the mechanism of the MLCT as well as the corresponding chemical bond, or even further altering it artificially in Metalloporphyrin system is desirable in order to design new functional materials with improved activity. The most straightforward way to alter the porphyrin functionality is to substitute the porphyrin center with various transition metals since the porphyrin metal center generally serves as the functional site which determines the porphyrin functions directly. However, such substitutions usually lead to drastic changes in porphyrin functionality, and more moderate tuning for function improvements are thus needed. The porphyrin outer ligands located around the periphery of porphyrin complexes have been reported to exhibit significant influence on the electronic structure of the metal center [54]. Mn porphyrins, for example, play significant roles in Mn-dependent oxygen evolution in green-plant photosynthesis [55,56], oxidation catalysis [56,57], and oxidative DNA cleavage [58–61]. This rich variety of functions essentially originates from the variation of the outer ligands as these porphyrins may also form complexes with fullerenes [62], functioning as tumor seeking MRI contrast agents [63] or regulators in the removal of superoxide anions in mammalian cells [64,65]. Artificial design of the outer ligands is therefore a promising way to alter (improve) the electronic structure as needed without interfering the chemical composition in the porphyrin central part - the metal center and its coordinated N ligands.

1.3 Brief Introduction of the Thesis Content

Chapter 2 introduces the experimental as well as the theoretical methods used in this thesis. Section 2.1 focuses on X-ray based spectroscopic methods, section 2.2 describes experimental apparatus employed in our experimental investigations. In Section 2.3 I explain in detail the recently developed techniques, required to introduce liquid samples into vacuum chambers. The sample preparation is discussed in section 2.4. The last section of chapter 2 introduces briefly the theoretical package ORCA used for our calculations of X-ray absorption spectra.

In Chapter 3 I investigate a simple system - iron chlorides in aqueous solution - by utilizing X-ray spectroscopic methods. In section 3.1 multiple decay channels, radiative and non-radiative, upon X-ray excitation at the iron L edge are studied separately, in order to find out a detection method that is free of various distortion effects in X-ray absorption spectroscopy. Section 3.2 compares photon emission with electron emission to gain complementary information on occupied states. The iron chlorides are used here as a simple prototype, demonstrating the strength and advantages of soft X-ray spectroscopy on solvated transition metal studies.

In Chapter 4 I present the soft X-ray spectroscopy results of porphyrins in solution. Section 4.1 contains the discussion and results of the study of monomeric iron protoporphyrin IX and cobalt protoporphyrin IX in dimethyl sulfoxide (DMSO) as well as the corresponding theoretical calculations for both systems. By changing the solvent to water the iron protoporphyrin IX (hemin) forms dimers. The nitrogen K edge and iron L edge X-ray spectra of hemin dimer are presented in section 4.2. The section 4.3 is dedicated to the investigation of the porphyrin outer ligand effects on the electronic structure of central metal ions in solution. The samples used here are iron octaethyl porphyrin chloride, iron tetraphenyl porphyrin chloride and manganese octaethyl porphyrin chloride, manganese tetraphenyl porphyrin chloride.

Chapter 5 concludes the whole study of solvated transition metal complexes with a brief summary and outlook.

2 Experimental and Theoretical Methods

2.1 X-ray Spectroscopies

2.1.1 X-ray Interaction with Matter

The X-rays were first observed by Wilhelm Conrad Röntgen in 1895 when performing experiments with a high voltage discharge tube in a darkened room [1,2]. The name X was given because of the unknown nature of emitted radiation. Today it is known as an electromagnetic radiation with wavelength in the range of Ångstrom to nanometer and has become an essential instrument for the investigation of the structure and properties of matter. As an electromagnetic wave, X-rays show wave-particle duality, which can be described by the relationship between quantized energy and wavelength:

$$E = h\nu = \frac{hc}{\lambda_{ph}} \qquad (1)$$

where E is the energy of the photon, h Planck's constant, c the speed of light, and ν and λ_{ph} the frequency and wavelength of the wave. The wave-particle character is also a phenomenon observed with electrons. Several kinds of interactions of X-ray with matter can occur. The most relevant interactions are absorption and scattering.

X-ray scattering events can be observed when X-ray photons are deflected from their original direction of propagation, after interaction with matter. Elastic (Thompson) scattering happens when a photon with specific frequency ω and momentum $\vec{k}$ impinges on a sample, interacts with the electrons, and a photon of the same frequency but different momentum direction $(\vec{k})$ is emitted. From a classical point of view, an incident electromagnetic wave causes the electrons bound to an atom to oscillate back and forth, and these electrons generate their own secondary wave field that has the same frequency as the incident wave. Inelastic scattering differs from elastic scattering in that the frequency of the emitted photon is not the same as the incident photon, but lower, *i.e.*, lower energy. The energy difference between the scattered and incident photon is transferred to the sample, usually causing valance excitations.

An X-ray photon can be absorbed as well by an atom where the photon may cause an electronic excitation from core level to valence level or above. The process is known as

photoelectric absorption. Two dominant processes occur subsequently after the X-ray absorption: radiative X-ray fluorescence and non-radiative Auger electron emission.

In X-ray fluorescence, the excess energy released by the excited atom after the relaxation process is carried away by an X-ray photon. In contrast, Auger electron emission is a non-radiative process, in which the excess energy is carried away by a secondary electron. Auger electron emission and X-ray fluorescence are competitive processes [66,67]. The rate of spontaneous fluorescence is proportional to the third power of the energy difference between the upper and lower states involved in the relaxation transition.

2.1.2 X-ray Absorption Coefficients and Cross-Sections

The absorbing power of a material is usually measured by the absorption coefficient μ, which describes the intensity attenuation of an incident X-ray beam passing through a medium. Formally, μdz is the attenuation of the beam through an infinitesimal thickness of sample dz. The X-ray intensity I after such a path is:

$$-dI = I(z)\mu dz \tag{2}$$

which can be solved by simple integration, leading to the Lambert-Beer law:

$$I(z) = I_{0}e^{-\mu z} \tag{3}$$

where I_0 is the incoming X-ray intensity.

The absorption coefficient μ depends on the types and distributions of atoms constituting the medium and the nature of their bonding and magnetism. The polarization and wavelength of the incoming X-rays also play a role. By measuring the incoming and transmitted X-ray intensities, and knowing the exact sample thickness d, the absorption coefficient can be experimentally determined using $\mu = ln(I/I_0)/d$.

The absorption coefficient is essentially an indication of the mobile electron density in material when the excitation energy is far away from resonant absorption edges where the absorption coefficient increases abruptly. One can, equivalently, describe the X-ray absorption effect using a more detailed parameter than μ, namely the *atomic absorption cross-section* of the element σ_a. The relationship between σ_a and μ is given by:

$$\mu = \rho_a \, \sigma_a = \left(\frac{\rho_m N_A}{A}\right) \sigma_a = c_{mol} N_A \sigma_a \qquad (4)$$

where ρ_a, N_A, ρ_m, A, and c_{mol} are the atomic number density, Avogadro's number, the mass density, the atomic mass and the molecular concentration, respectively. The absorption cross-section has units of area and often the $Barn$ is used. One $Barn$ is defined as $10^{-28} m^2$ and is approximately the cross sectional area of a uranium nucleus. The absorption coefficient μ is element-specific and has a strong dependency on the X-ray energy. An example is shown in Figure 2 for the element iron, together with the elastic (Thomson) and inelastic (Compton) scattering contributions [68–70]. This example illustrates the dependency of the absorption cross-section on the X-ray energy and the presence of some discontinuities (absorption edges) at specific energies. These discontinuities occur at energies for which an X-ray photon has sufficient energy to resonantly excite an electron from a core electronic orbital to upper unoccupied orbital, which gives rise to a sudden increase of the absorption cross-section. The presence of these absorption edges is the fundamental phenomenon exploited in X-ray absorption spectroscopy (XAS) experiments.

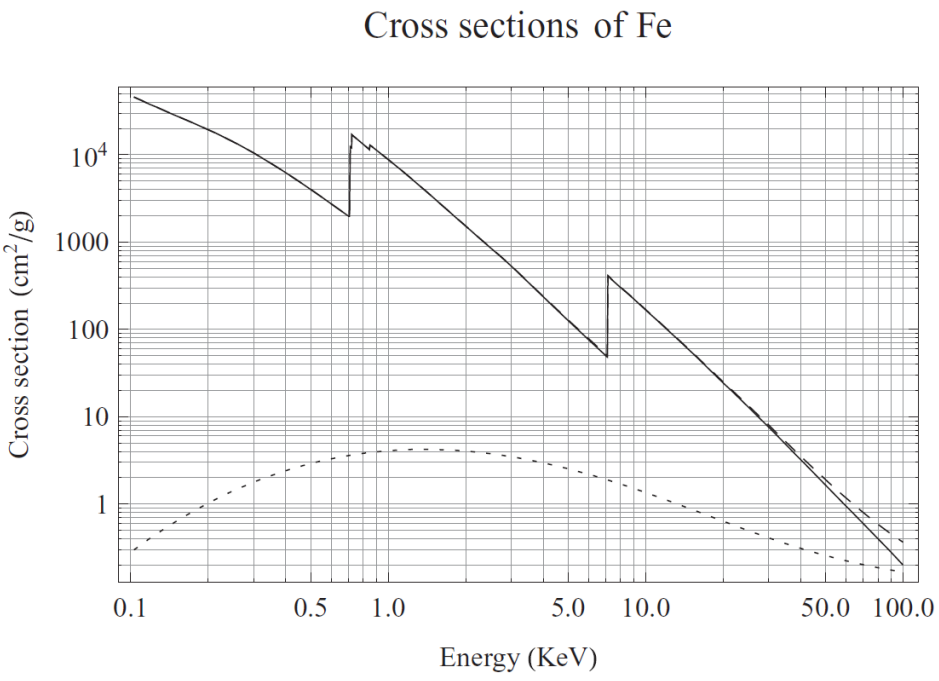

Figure 2. Photoelectric absorption (solid), elastic and inelastic scattering (dotted), and total (dashed) cross sections of Fe, taken from *Bunker*, p. 18 [71].

In quantum mechanics, the bound electron occupies a series of discrete energy levels or orbitals whose wave functions and eigenvalues are solutions to the Schrödinger equation.

Each of these levels is characterized by a series of quantum numbers, specifying the electronic state. The states are classified according to their principal quantum number $\boldsymbol{n}$, being labelled as K for $\boldsymbol{n = 1}$, L for $\boldsymbol{n = 2}$, M for $\boldsymbol{n = 3}$, … According to the Sommerfeld notation, X-ray absorption edges are named in order of increasing energy. For example the K edge corresponds to an absorption from the $\boldsymbol{(1s)^2}$ level; whereas the L_1-, L_2- and L_3-edges arise from the absorption at $\boldsymbol{(2s)^2}$, $\boldsymbol{\left(2p_{1/2}\right)^2}$ and $\boldsymbol{\left(2p_{3/2}\right)^4}$, respectively.

A scheme of the atomic energy levels and the nomenclature used to label the X-ray absorption edges is shown in Figure 3. The specific energies at which the absorption edges occur are unique to each element, serving as the fingerprint of the atomic species present in a material [72].

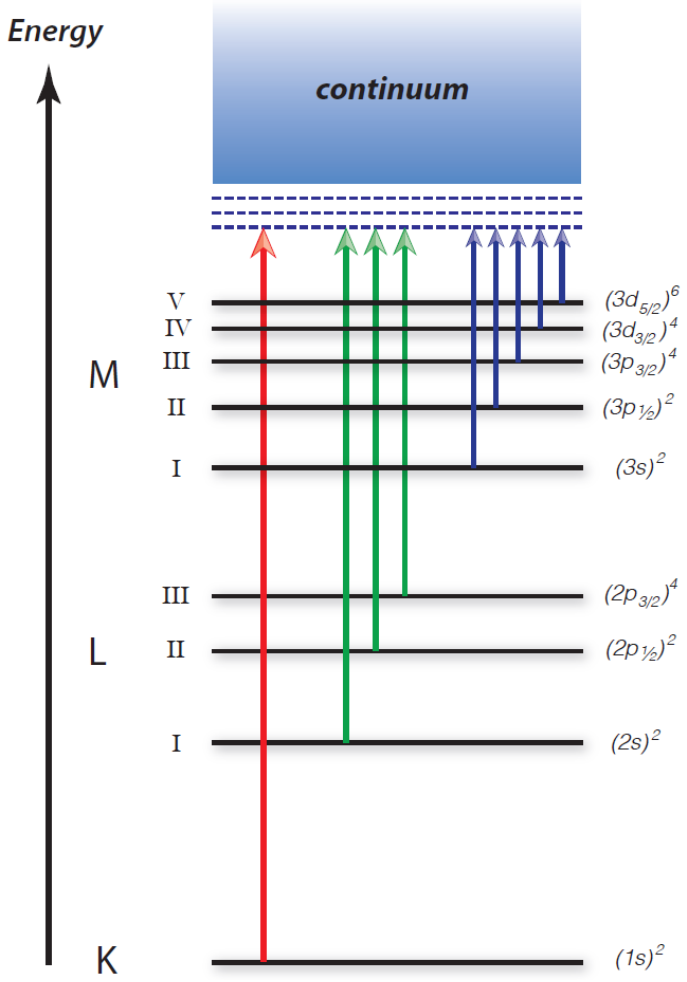

Figure 3. Schematic drawing of the atomic energy levels and the nomenclature used to label the X-ray absorption edges. Redrawn and adapted from [72].

2.1.3 Radiative and Non-Radiative Decays

The filling of an inner shell vacancy (core hole) by an outer shell electron after the absorption of an X-ray photon can produce X-ray fluorescence (Figure 4), whose energy is equal to the energy difference between the two shells. The nomenclature for the X-ray fluorescence lines is somewhat more complex than that for absorption and is covered extensively in the literature [66,73]. The reason is that X-ray fluorescence involves two bound orbitals, contrary to the absorption where only one bound orbital is involved. The K-series involves transitions where the electron relaxes to the K- (or *1s*) state. Likewise, fluorescence L-lines have L-states (n = 2) as the final destination in the electronic relaxation process, and so on. The fluorescence lines can split due to the spin-orbit interaction.

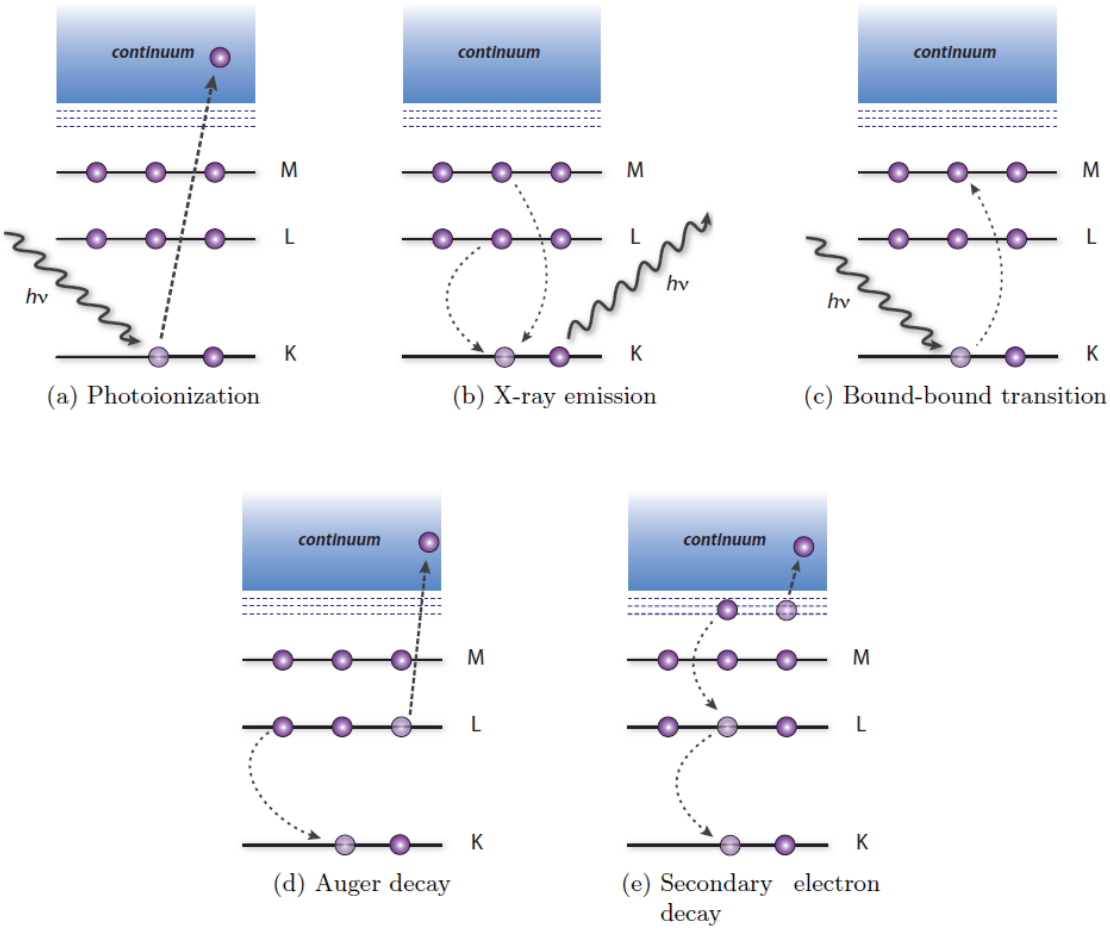

Figure 4. Schematic of the energy level diagrams of atomic excitation and relaxation processes. For clarity only the three electronic shells are shown. Adapted from [72].

The fluorescence yield (or radiative probability) is defined as the ratio of the emitted X-rays to the number of primary vacancies created. The function increases monotonically

with the atomic number Z, and is larger for K edge than for L and higher edges. The measured X-ray fluorescence intensity is proportional to the incoming X-ray intensity, the fluorescence yield probability and the absorption coefficient. X-ray fluorescence can therefore be used to obtain electronic information about the material under study. Non-resonant X-ray emission spectroscopy (XES) provides information on occupied electron orbitals in the valence shell. Experiment is done by tuning the incident photon energy to an absorption edge and observing the specific X-ray emission lines.

As stated previously, after the absorption of an X-ray photon the atom is in an excited, unstable state. Apart of X-ray fluorescence, the other major de-excitation process is the Auger effect. Auger emission (Figure 4d) is a non-radiative, two-electron process occurring when an outer shell electron relaxes to the core-hole followed by the ejection of a second electron carrying away the energy produced in the relaxation process [66]. The non-radiative Auger processes competes with the (radiative) fluorescence yield. The relative yields depend on the atomic number Z [66,67]. The fluorescence is extremely small especially for elements with small atomic number, as shown in Figure 5.

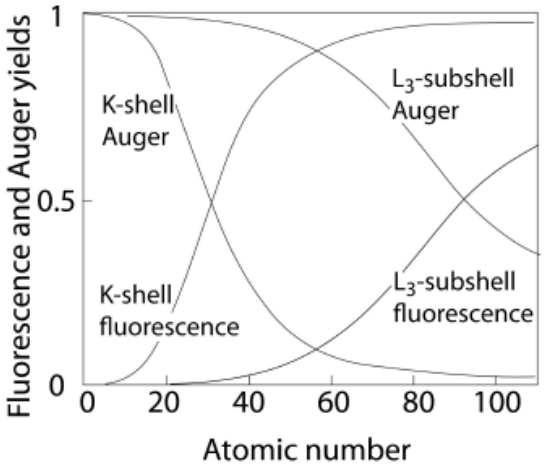

Figure 5. Fluorescence vs. Auger yields for K and L_3 shells in dependence of the atomic number. Adapted from [74].

2.1.4 X-ray Absorption Spectroscopy (XAS)

The attenuation coefficient from equation (3) contains the information of the absorption cross section. In order to do XAS one would ideally measure I and I_0 accurately and simultaneously. Such a transmission experiment is difficult for several reasons though. Soft X-rays for example are strongly attenuated within a few micrometers of almost any

kind of condensed matter. The transmitted intensity to be detected is thus very weak. Therefore the sample must be very thin which is, however not applicable for most of samples.

As pointed out above the core hole that is created in an X-ray absorption process will be filled by an electron from upper energy level and the released energy will be transferred to an Auger electron or a photon. In principle, detecting either of those emitted particles gives a measurement of the absorption cross section since their respective emission strength should depend on the amount of core holes created. The two techniques based on this reasoning are the total electron yield (TEY) and the total fluorescence yield (TFY) where emitted electrons or photons of all energies are detected and summed up to obtain a measurement of the absorption. Total yield is used as a term to distinguish from partial yield (PY) methods where electrons or photons are discriminated based on their energies. While energy dispersion reduces the overall signal strength it can reduce background signal as well, simplifying interpretation and enhancing sensitivity. PY can also be used to discriminate scattered light and only detect actual fluorescence, as done by *Jaklevic et al.* [75].

TEY is a surface sensitive method due to the shallow escape depth of electrons from matter [76]. This limits its feasibility to probe bulk properties. Fluorescence based methods, however, is bulk sensitive and can be used with the presence of magnetic or electric fields. The disadvantage of FY is that it suffers more saturation effects due to its longer penetration depth than electron yield.

Achkar et al. [77] proposed a method termed inverse partial fluorescence yield (iPFY) that is argued to be free of saturation effects. Utilizing this technique requires two transitions in the sample. One of the transitions is the resonant excitation of the element of interest, the other comes from another element in the sample system with lower excitation energy which will be excited non-resonantly throughout the experiment. Since all photons are absorbed in the sample, the amount of the non-resonant excitations is in direct competition with the resonant one. In the example of Fe_2O_3 one would observe a signal drop of the oxygen K edge emission when scanning the iron L edge. The drop in the oxygen fluorescence can then be directly related to an uptake in the iron absorption. Inversion of this oxygen K edge PFY signal gives rise to the normal Fe L edge XA peaks which show direct linear proportionality to the attenuation coefficient. Due to the non-resonant character of the detected photons, iPFY is free of saturation effects that are

common in TFY and PFY measurements. A constant cross section for non-resonant emission is assumed, which can be easily justified [75,77]. For aqueous solutions of transition metals the iPFY is especially suited. Oxygen from the water is present at a high concentration and its K edge fluorescence with a threshold energy of about 540 eV can be used to monitor for instance the iron L edge absorption between 700 eV and 730 eV.

2.1.5 X-ray Emission Spectroscopy (XES)

XAS probes element-specific unoccupied states. Off-resonance X-ray emission spectroscopy (XES), on the other hand, measures occupied states, providing a complementary picture to XAS. A core ionized atom will emit fluorescence when an electron from an occupied state relaxes into the core hole. The energy of the emitted photons corresponds to the energy difference between the valance level and core holes and thus the energetic structure of the occupied orbitals can be deduced from X-ray emission spectra (see Figure 4). Such explanation of X-ray emission is referred to as two step model described in the previous sections. Excitation of a core electron happens in a first step and a second decoupled step gives rise to the emission spectrum. Such a picture can be considered correct if the intermediate, core hole state relaxes before the emission, meaning one photon excites one distinct intermediate state before emission occurs [78]. For resonant excitations, where a core-electron is promoted to an unoccupied bound state, the two step model fails to explain experimental observations in some cases though. In a photon-in photon-out experiment the intermediates can be undefined virtual states and the experiment is more accurately described within the framework of scattering theory. Because the experiment is viewed as an inelastic scattering process, it is termed Resonant Inelastic X-ray Scattering (RIXS). Scattering theory describes the system in terms of a ground-state $\langle g|$, final state $\langle f|$ and intermediate state $\langle i|$. The major contributions to the scattering spectrum for an incident photon of frequency (ω_{in}) and a scattered photon of frequency (ω_{out}) are given by the resonant second order part of the Kramers-Heisenberg formula [79,80]:

$$F(\omega_{in},\omega_{out}) \propto \sum_f \left| \sum_i \frac{\langle f|T|i\rangle\langle i|T|g\rangle}{E_g + \hbar_{\omega_{out}} - E_i + i\Gamma_i} \right|^2 \times \frac{\Gamma_f}{\left(E_f + \hbar_{\omega_{out}} - E_g - \hbar_{\omega_{out}}\right)^2 + {\Gamma_f}^2} \tag{5}$$

where E_g, E_f and E_i are the energies of the corresponding system eigenstates and Γ_i and Γ_f their life time widths. T is the optical transition operator; the dipole approximation can be used to isolate the dominant transitions. The total scattered amplitude contains higher order contributions beyond equation (5), but they are off-resonant terms and negligible with respect to the resonant contributions in eq. (5).

Some of the unique features of RIXS should become evident directly from the scattering formula. The energy difference between excitation and scattered photons corresponds to the difference in ground and final states of the atom. Because the dipole operator acts twice, the ground to final state transition does not need to be dipole allowed and transitions with zero change in angular momentum are thereby accessible. In consequence the information on electronic transitions from RIXS is complementary to the information obtained from optical UV-Vis spectroscopy, similar in the way that Raman-spectroscopy is complementary to infrared absorption for vibrations. Furthermore, the spectral linewidth of RIXS is determined by the lifetime Γ_f of the valance excited final state which is much longer than that of the core-hole involved final state (initial state) in XAS (XES). Therefore RIXS can often exhibit well-resolved features even when the XAS or XES peaks are broad.

While the above features can also be explained in a more elaborate two step model, the most fundamental difference between the two and one step models lies in the cross terms of different intermediate states arising from the squared sum in equation (5). If the spacing of intermediate states is smaller than their lifetime broadening, multiple intermediate states are excited in a quantum mechanical superposition of the wave functions and interference occurs [81]. Normal emission (constant emission photon energy) and inelastic scattering (constant energy loss with respect to incident energy) will both contribute in an actual experiment and which description fits better depends on the system. A correlated, localized valance electronic system will exhibit strong RIXS features as for d or f electrons, while a delocalized valance system, as for s or p electrons, usually gives rise to normal emission features. The extreme case of a quick electron delocalization is photo-ionization in which the core-electron is completely removed from the atom. Therefore, in off-resonant excitation the emission spectrum does not change with excitation energy.

2.1.6 Resonant Photoelectron Spectroscopy (RPES)

The fluorescence decay is more favorable in high-Z atoms with deep inner shells excited by X-rays. For the low-Z atoms or outer shell excitations, Auger process is dominant in relaxation processes, as shown in Figure 5 [82]. Our particular focus here is the intensity enhancement of certain valence features in the valence photoelectron spectroscopy when the excitation photon energy reaches some core-level absorption edges [30,83], which is in general called resonant photoelectron spectroscopy (RPES). The signal enhancement is realized when the kinetic energy of the direct photoelectron matches that of the Auger electron, as shown in Figure 6A. The Auger decay and the direct photoemission leads to a resonant photoelectron spectrum where the intensity is not just the sum of these two processes. Instead, both add their electron wave functions together coherently, resulting in so-called *Fano*-resonance spectral profiles in PE spectra [84]. Several variants of the Auger process can occur, depending on charge transfer and depending on whether or not the resulting core-hole remains localized on initial species, within the timescale of the Auger process. Although the most relaxation processes are of subordinate relevance for the iron complexes I will discuss in my thesis, it is still useful to briefly introduce them in order to demonstrate the complexity of electronic relaxation processes in aqueous solutions.

For the transition metal complexes in water energy and charge transfers can occur in various relaxation channels, as shown in Figure 6. A localized spectator electron can be produced at valence level upon resonant excitation, whose presence will raise the kinetic energy (KE) of the Auger electron due to its screening of the core hole, as compared with the situation of delocalized (transferred away) excited electron, as illustrated in Figure 6B. This local event can be utilized to detect ultrafast electron delocalization of an excited core electron. The lifetime is usually very short, e.g., ~ 4 fs for Oxygen *1s* core-hole [83]. Changes in the resonant Auger spectrum as a function of photon energy (or e.g., for a set of different hydration configurations) can hence reveal detailed information of the exact nature of the relaxation process. This so-called core-hole clock technique has been used for instance to determine charge-transfer-to-solvent excited-state energies of aqueous chloride ions [30] and to probe the dependence, in neat water, of the ultrafast electron delocalization from a core-excited H_2O molecule on hydration configuration [85].

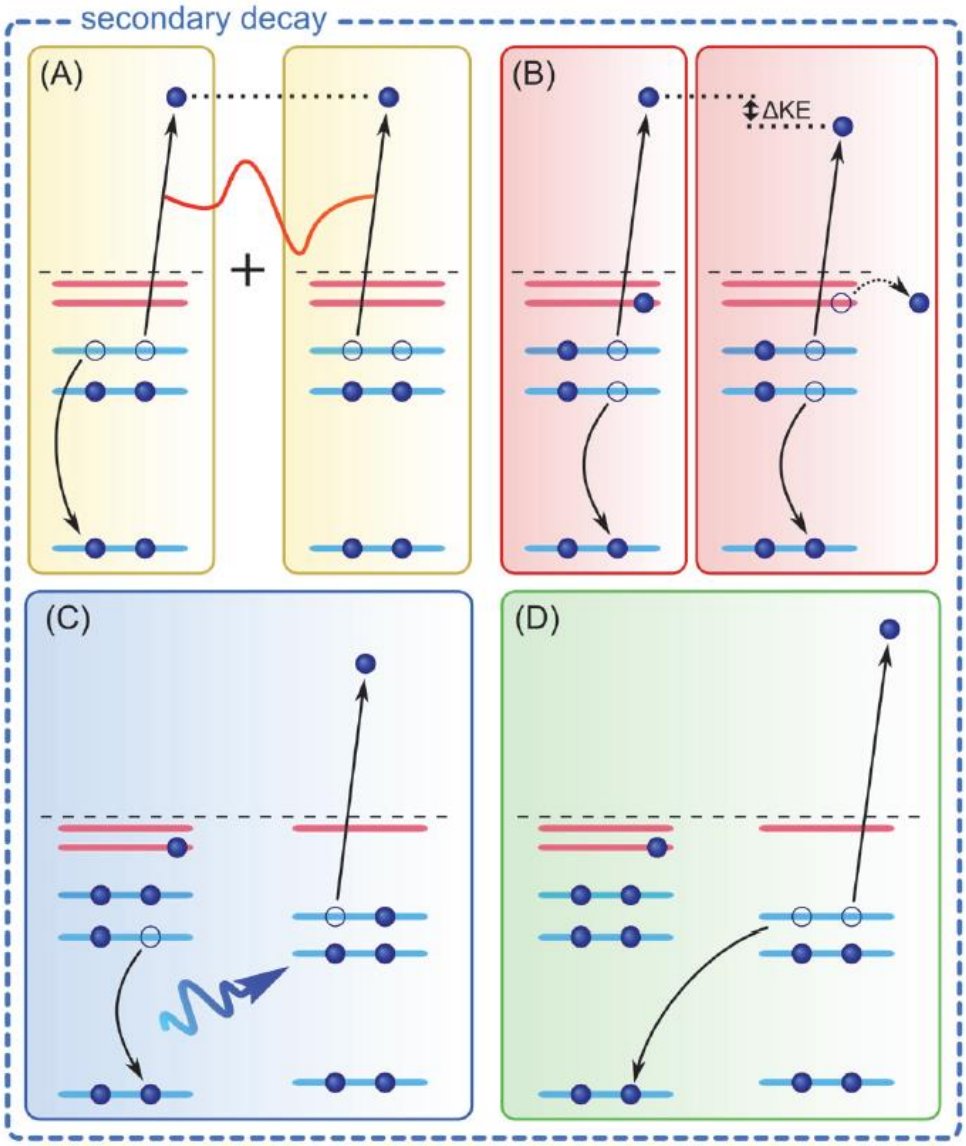

Figure 6. Schematic energy-level diagram for the electronic excitation and relaxation processes, (A) Resonant PE process; (B) Auger decay with spectator electron (left) and with delocalized excited electron (right); (C) Intermolecular Coulombic decay, ICD; (D) Electron-transfer mediated decay, ETMD. In case of (B-D) promotion of a core electron to an empty state is assumed. In case (A) promotion of a core electron to a partially filled valence orbital is assumed [86].

Sometimes an electronically excited system relaxes via a non-local type of Auger process. This is the case when the final Auger state contains one hole in the initial atom and another in a neighboring atom, which is different from the regular two-hole final state in one local site. The so called two-site Auger decay involves an energy changer from the core-hole excited site to the neighboring site, which can be monitored in weakly bonded systems. This process is termed Intermolecular Coulombic Decay (ICD) [87,88] and is presented in Figure 6C. In this particular case, a lower Coulomb repulsion energy is reached, compared to the two-hole final state in normal Auger decay. In aqueous solution, ICD has been

proposed for the hydroxide anion in water [30]. Furthermore another decay process is conceived, as shown in Figure 6D where an electron transfer between two sites might occur. So far, the electron-transfer-mediated decay (ETMD) has not yet been observed in aqueous solution. Auger processes occur within the very short lifetime of the core hole. Electronic relaxation dynamics, including charge and energy exchange between solute and solvent, can thus be studied at the very early time after the initial excitation.

2.2 Experimental Methods and Setups

2.2.1 Synchrotron Facility - BESSY II

Synchrotron radiation is the electromagnetic radiation which is emitted when relativistic charged particles change directions in a magnetic field. The synchrotron radiation was already predicted theoretically in 1945 when the Nobel Prize winner J. S. Schwinger developed a mathematical description of radiation from accelerated relativistic electrons [89]. Amongst others, this theory describes that for relativistic electrons the typical dipole radiation pattern is transformed to a strongly forward concentrated distribution which gives synchrotron radiation its highly collimated property. Inquiring the reason of energy losses, the predicted synchrotron radiation was for the first time visually observed in 1947 at a betatron (a magnetic-induction electron accelerator) of the General Electric Research Laboratory in Schenectady, New York [73]. Recognizing its high potential, scientists soon moved from the initial parasitic operation at high energy facilities into storage rings which were dedicated to the creation of synchrotron radiation. A further development to the so called third generation synchrotron facility took place when storage rings were optimized for insertion devices like wigglers and undulators. An undulator as schematically shown in Figure 7 is an array of closely spaced vertically oriented dipole magnets of alternating polarity. An electron beam passing through this array of magnets is forced by the magnetic field on a slalom course. The radiation cones that are emitted at each turn of the trajectory interfere with each other, leading to a highly collimated beam with a spectrum of a few energetically narrow peaks. The advantage of the synchrotron radiation from an undulator is its high photon brilliance (photon flux per area of radiation source, per solid angle of the radiation cone).

The BESSY II synchrotron, at which the experiments of this thesis were carried out, is a facility of the third generation. Free electrons are created via a hot cathode and then accelerated by an anode voltage up to 100 keV. Further acceleration takes place after injection into the orbit of the microtron which contains two deflection magnets of constant magnetic field strength and a high frequency linear accelerator. The energy gain by passing through the linear accelerator leads to a larger turning radius of the electrons in the field of the deflection magnets. When the electrons reach an energy of 50 MeV they are passed into the synchrotron, where they are further accelerated to the final energy of 1.7 GeV by alternating fields of a cavity resonator. The field strength of the magnets, which hold the electrons on the synchrotron orbit, is continuously adapted to the increasing kinetic energy of the electrons. Through a transfer channel the electrons are afterwards injected into the storage ring, where bending magnets, wigglers, and undulators are inserted for the creation of the synchrotron radiation. There are about 50 beamlines and experimental stations at BESSY II. The measurements presented in this work were carried out at the undulator beamline U41-PGM (plain-grating monochromator), which will be introduced in the following section.

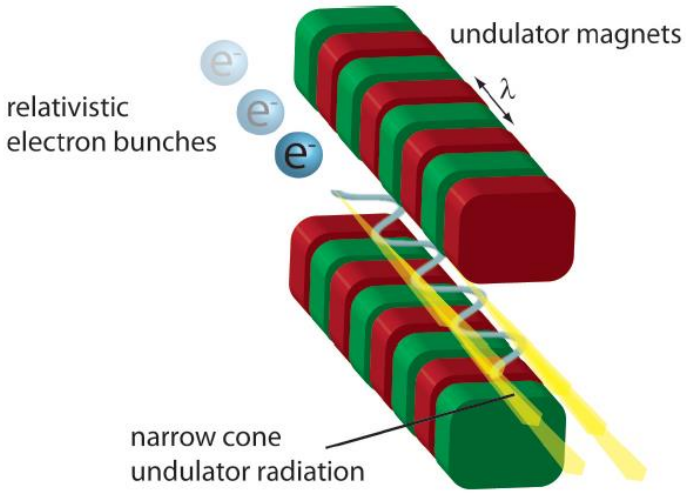

Figure 7. Schematic depiction of the creation of synchrotron radiation within an undulator, taken from [90].

2.2.2 Beamline - U41-PGM

In order to measure diluted liquid samples from a micro-jet of around 20 µm diameter, an intense X-ray source with small focus is required. The micro-focus beamline U41-PGM

(see the schematic in Figure 8), at which the experiments presented in this thesis were carried out, meets the requirements [91]. The beamline undulator has a magnetic array of 80 units with period length of 41 mm, producing horizontally linearly-polarized light. It is installed at a low beta section of the storage ring where the electron beam is generally more focused. Monochromatization of the light is achieved by a combination of a plain grating (600 lines per mm) and a plain mirror which allow, upon varying the fix- focus constant c_{ff} , to obtain either a high photon flux or a high energy resolution, according to the experimental requirements. Photon energies ranging from 170 up to 1800 eV can be provided. At 540 eV an energy resolution of approximately 180 meV can be obtained at 20 µm exit slit for high photon flux. A cylindrical mirror focuses the monochromatic collimated beam vertically onto the exit slit. The size of the exit slit can be varied between 20, 40, 100, 200, 500, 2000 and 3000 µm. Since the resolution increases with decreasing slit-size, all X-ray absorption measurements presented in this work were carried out with a 20 or 40 µm slit only. After the exit slit, a toroidal mirror refocuses the synchrotron radiation to the experimental chamber. By this a spot size of 23 µm (hor.) x 12 µm (ver.) with a flux of 10^{13} photon/s can be achieved (ring current: 300 mA; c_{ff} value: 0.65; slit: 40 µm; energy 480-800 eV @ 1st and 3rd harmonic) at the experiment. Upon measuring the current on the refocusing mirror, variations in the incoming flux can be normalized for the measured data.

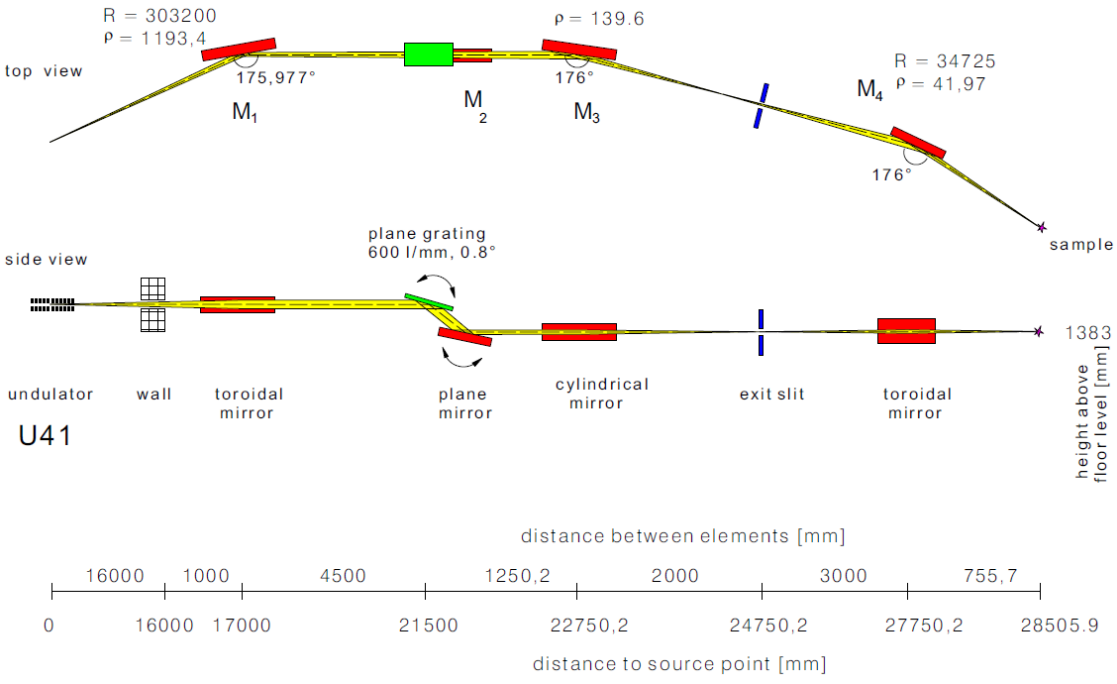

Figure 8. Layout of the U41-PGM beamline at the BESSY II synchrotron facility [92].

2.2.3 Experimental Station - LiXEdrom

H. A. Rowland worked out a solution for minimizing the aberrations of a spherical grating almost a hundred years ago [93]. For a spherical grating of radius 2R if the grating and the source lie on a circle of radius R most higher expansion terms vanish and focusing will occur along this circle of radius R, called the Rowland circle (shown in Figure 9) [94,95]. Sagittal focusing will not be achieved on the circle though, leading to a wavelength dependent astigmatism [95]. The wavelength dispersion along the circle can be used to select a wavelength as a monochromator or to acquire an energy resolved spectrum, via imaging the diffraction pattern. Rowland's design significantly reduces the amount of optical elements and in consequence the photon losses during the energy dispersion. A spherical reflective grating is the only optical element needed for a Rowland circle design, serving as a diffracting as well as focusing device simultaneously.

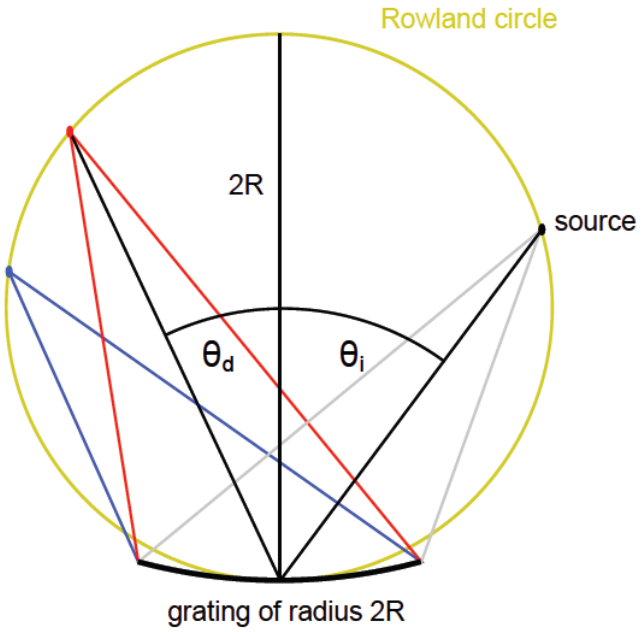

Figure 9. Illustration of a Rowland circle: White light originates from a source on the circle of radius R, gets diffracted by the grating of radius 2R and the different colors come into the different focal points along the circle of radius R [96].

The detection of the energy-resolved photon signal is realized in an experimental station named LiXEdrom as shown in Figure 10. The monochromatized synchrotron radiation is focused on the sample which acts as a point-like light source, from which light is emitted and hits the grating. The dispersion occurs along the Rowland circle where a movable detector assembly is used to image the diffraction pattern. By moving the detector a large energy range in different diffraction orders can be covered. The detector is oriented

tangentially to the circle. Although the detector is flat, its surface area is very small compared to the size of Rowland circle (grating radius of 7.5 m, detector active area 5 x 5 cm), which minimizes the influence of not being perfectly on the circle.

The detector consists of a deflection plate, two micro-channel plates (MCP), a phosphorous screen and a CCD camera (see Figure 11). Photons create electrons through the photoelectric effect when they hit the first layer of the MCP. The MCP then acts as a position resolved electron multiplier. It consists of many small tubes (the micro-channels) between two plates under high electrical potentials. The tubes are lined with a high resistance semiconductor material, producing avalanche of secondary electrons when an electron collides with a micro-channel wall. All ejected electrons are then accelerated towards the bottom of the MCP and finally reach the phosphorous screen due to the potential, resulting in fluorescence images, which is photographed by the CCD camera. The negatively-biased deflection plate located above the MCP pushes back the secondary photo-electrons that travel towards the plate in order to enhance signal.

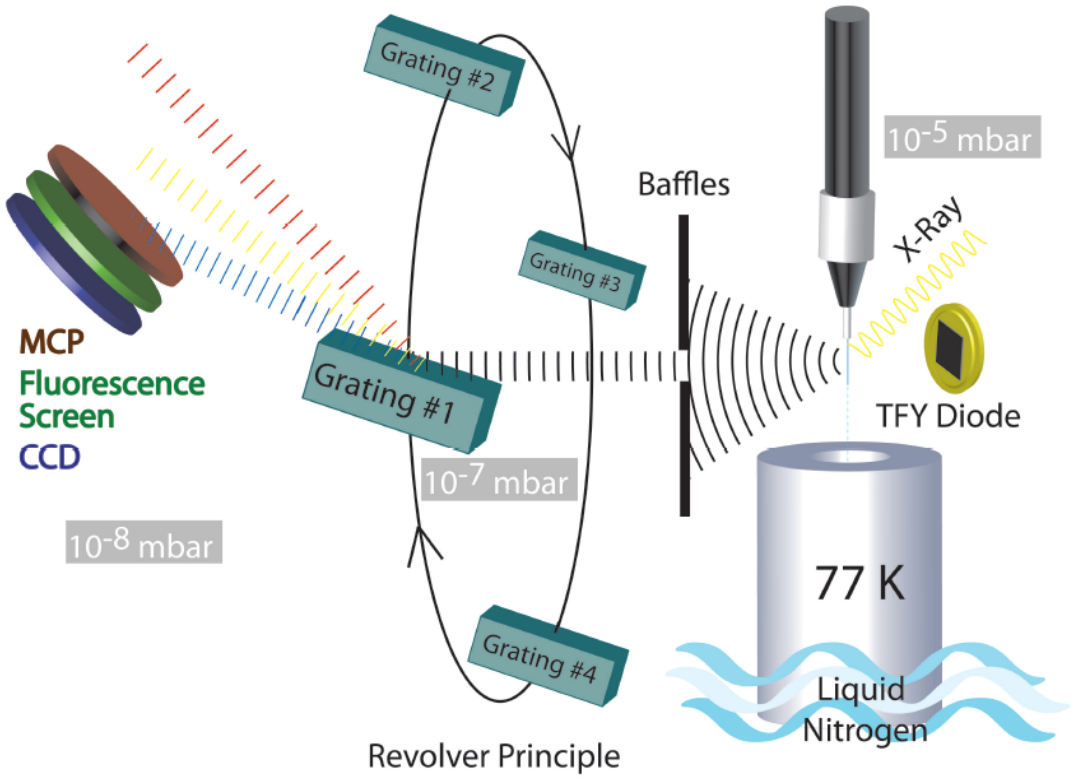

Figure 10. Schematic drawing of the LiXEdrom setup [31]. The liquid sample is delivered via micro-jet and trapped inside a container cooled by liquid nitrogen. The emitted light is collected via total fluorescence yield (TFY) mode for XAS measurements or partial fluorescence yield (PFY) mode for XAS and RIXS with the help of four rotatable gratings.

Four gratings are mounted on a revolver-like holder, covering 50-1.000 eV energy range for emitted photons. An appropriate grating can be selected by rotation of the holder, as illustrated in Figure 10, depending on the requirements of experiments. Emitted light from sample travels horizontally towards the grating chamber until it hits the grating. Having each grating mounted at a different angle the Rowland circle geometry is realized for different grating radii by moving the detector accordingly without the need to alter source and grating position.

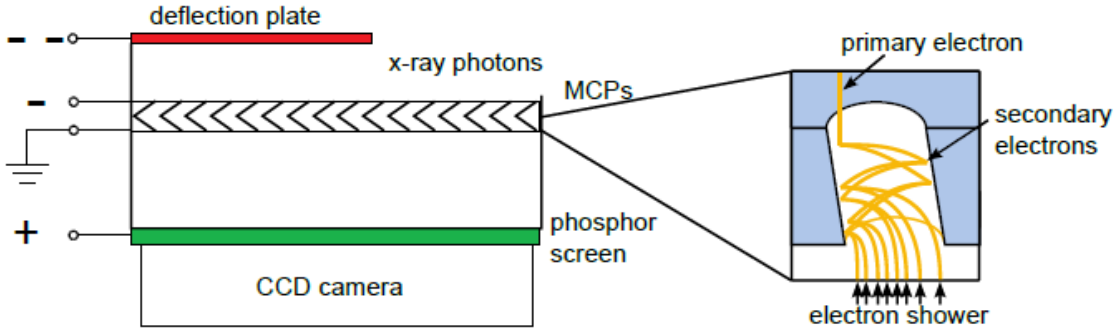

Figure 11. Detector assembly in the LiXEdrom and the principle of electron multiplication in the micro-channels [96].

2.2.4 Liquid in Vacuum - Micro-Jet

Soft X-rays are very strongly absorbed in any kind of matter. Penetration depth in air at ambient pressure is only a few millimeters, and considerably reduced to the order of micrometers if in condensed matter. Therefore, to utilize soft X-rays spectroscopy a vacuum is required, which complicates the application of liquids. In vacuum any liquid will evaporate until its equilibrium vapor pressure is achieved (e.g. 6.1 mbar at the triple point of water at 0.01 °C) [97]. During the process of evaporation the liquid becomes cool and eventually freeze.

The liquid micro-jet provides the possibility of introducing a liquid samples into vacuum, whilst maintaining an acceptable vacuum pressure. To this end a small stream of liquid with micrometer diameter, the jet, is shot into the vacuum. After traveling a short distance in vacuum where the sample can be probed by X-rays, the major portion of the liquid is contained by freezing or a recovery mechanism [98]. Since the frozen liquid, i.e. solid, usually have very low vapor pressure and the liquid travels only a short distance in vacuum with a small surface area exposed (due to the micro-sized jet), the amount of

evaporated liquid can be much reduced [99]. With a sufficient turbo molecular pump speed a vacuum at 10^{-4} ~ 10^{-5} mbar can be maintained. The liquid sample is continuously refreshed, thus heating and radiation damage by X-rays can be eliminated.

The liquid jet is created by pressing a liquid through a glass nozzle with a micrometer opening. The liquid is pumped at a constant rate of flow, with pumps originally developed for high performance liquid chromatography (HPLC) from Techlab GmbH. Through a double piston mechanism the pump provides a steady flow, with very limited pulsation from the piston movements. Typical nozzle openings used in the experiments are between 10 and 30 µm. The liquid jet ejected at high speed from a nozzle initially forms a laminar flow and then decays into small droplets [100,101]. The laminar-jet, while being smooth and cylindrical, narrows down by approximately 10 to 30% after exiting nozzle. The region of laminar flow is used for X-ray probing because it provides a region of bulk liquid with a defined surface and low vapor pressure. The length of the laminar region varies with the speed of the jet and has a typical length of a few millimeters. The jet speed u can be calculated via limit case of Bernoulli-flow for cone-shaped liquid nozzles:

$$u = \sqrt{2p/\rho} \tag{6}$$

The liquids viscosity is irrelevant, u depends only on inlet pressure p of the nozzle and the liquids density ρ. In case of running water ($\rho = 1000kg \cdot m^{-3}$) with a pressure of 40 bar the exit velocity accounts to $u = 89m \cdot s^{-1}$. After the laminar flow disintegration of the liquid jet into the formation of droplets sets in, depending on surface tension, viscosity and nozzle diameter. A nozzle shooting a liquid jet, along with the decay of the laminar flow, is shown in Figure 12.

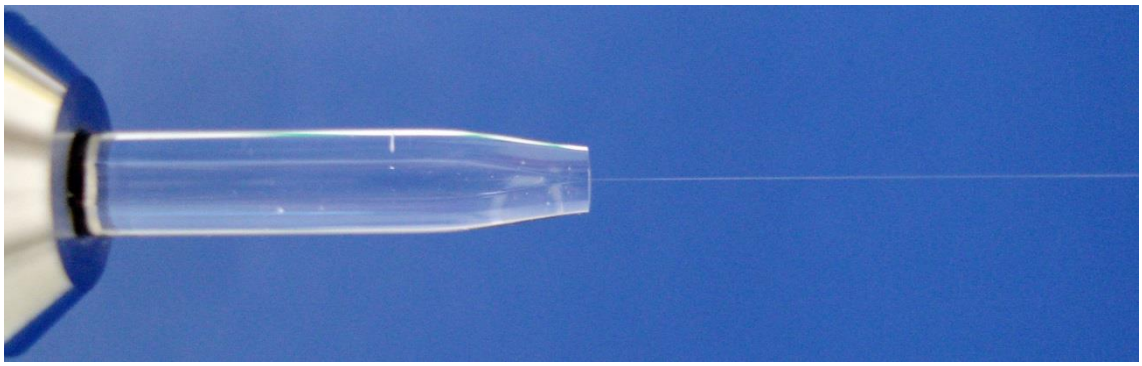

Figure 12. Liquid micro-jet of water from an 18 µm (inner diameter) nozzle. The glass capillary is 3 mm in outer diameter.

After freezing the liquid sample it is generally not reusable. It is possible to recover the liquid sample by collecting the jet in a liquid trap. In such a design the liquid jet is shot through a pinhole of a liquid trap, instead of freezing. The pinhole restricts the airflow from the trap to the sample chamber and therefore a higher pressure in the trap can be maintained. If the vapor pressure is high enough for the liquid to condense, recovered sample can be removed periodically. Such a construction poses significant challenges, as the pinhole must be small enough to restrict airflow while it must be possible to be aligned with the jet. At the same time the jet must be strong enough to overcome the gas stream coming out of the trap. Such practical difficulties have so far prevented the implementation of a recovery system into our measurement scheme. The micro jet system we used originates from Microliquids GmbH [102].

2.2.5 Liquid in Vacuum - Flow Cell

The utilization of a flow cell is another technique to investigate liquids in vacuum with soft X-rays. In such a cell the liquid remains separated from the vacuum by the use of a membrane. The membrane has to be very thin in order to apply photon-in photon-out measurements. So far most of the X-ray investigations on liquid were done by the utilization of a static cell with no flowing liquid [78,103–105], enclosed in a small container cell. The application of flow cells with flowing liquid, is relatively new. For instance, *Fuchs et al.* probed the oxygen K edge of H_2O in flow cell [106]. The flow cell technique has two major advantages. On the one hand, local temperature rise close to the membrane when using intense X-rays is suppressed and on the other, decomposition of molecules is largely avoided by constant refreshing of the liquid [106].

During my PhD study, I developed a flow cell (appendix 8.13), applicable in the LiXEdrom station. The cell is mounted inside the chamber at 45° angle with respect to the incident X-ray beam. Two types of the cell were produced in the workshop of the Helmholtz-Zentrum Berlin. One was made of polyether ether ketone (PEEK). The other one was made of steel 1.4562 (X1NiCrMoCu32-28-7) which is an alloy containing high amounts of nickel and chromium in order to make it durable against pitting corrosion. Sealing rings are made of Viton, a fluorinated rubber which guaranties high chemical resistance. During operation the membranes were pressed mechanically against the cell body. In the main chamber the vacuum of $1 \cdot 10^{-6}$ to $5 \cdot 10^{-7}$ mbar was normally maintained. In case of membrane rupture the LiXEdrom is equipped with an interlock system that

closes the valves autonomously if a pressure rise sets in. The grating chamber, beamline and turbo molecular pumps remain protected. A peristaltic pump (*ISMATEC* IP65) was used to push the liquid during the measurements. A minimum of 5 ml sample volume is required for the measurements. The membrane windows are of vital importance for the performance of the experiments. Due to the utilization of soft X-ray they have to be thin and free from contamination. In addition they need to provide sufficient stability to withstand the pressure difference (~1 bar). The membrane windows are made of silicon nitride (Si_3N_4, *Silson Ltd.*, United Kingdom) or silicon carbide (SiC, *NTT Advanced Technology Corp.*, Japan). Both materials are very hard ceramics and feature an excellent thermal tension resistance (Thermowechselbeständigkeit) and high fracture toughness. The dimension of silicon nitride membranes was 1.0 x 0.5 mm width and 100 nm thickness. The silicon carbide ones were 1.0 x 1.0 mm width and 150 nm thick. Both window types are manufactured onto silicon wafers of 10 x 10 mm width and a thickness of 350 - 500 µm. Figure 13 presents calculated transmission curves for soft X-rays through both materials [107]. When flow cell tilted to 45° the transmission is reduced further by 10-20 %.

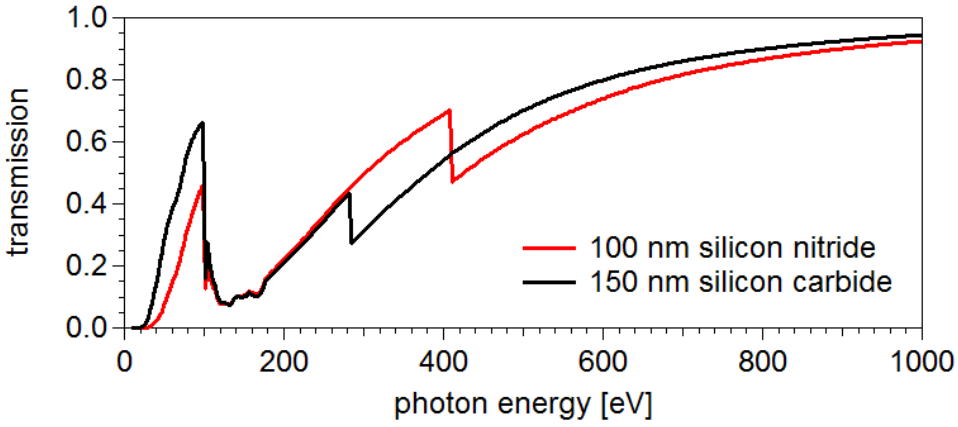

Figure 13. Transmission curve of soft X-rays through the membrane windows.

Total fluorescence yield (TFY) is measured with a gallium arsenide phosphide (GaAsP) photodiode mounted close to the membrane window. For very low concentrated samples, e.g. porphyrins in solution with typical concentrations in the range of a few millimolar, data acquisition time is much extended due to the general low signal strength. Additional interactions with the membrane, like hydrophobic or hydrophilic effects or chemical reactions need to be considered. One advantageous feature of a flow cell measurement, compared to micro jet technique, is the very small amount of required sample since the liquid can be recycled in a closed loop system.

2.3 Sample Preparation and Measurement Considerations

2.3.1 Aqueous Ferric Solution

For our experiments discussed in section 3.1 $FeCl_3$ hexahydrate salt (CAS: 10025-77-1) was purchased from Sigma Aldrich Chemie GmbH with > 99% purity. 64.9 g salt was dissolved in 200 ml de-ionized water ($\Omega \geq 1.8 \cdot 10^7$) and 40 ml fuming HCl to make one molar aqueous solution (≈290 ml). The solution was stirred for 10 minutes and then filtered with a Machery-Nagel 619eh filter, providing a retention capacity of at least 4 µm. Filtering is essential to remove undissolved residual particles because large particles can easily block the micrometer opening of the nozzle. The measured pH value was -0.60. Most of the complex might not be hexaaqua coordinated but, due to the addition of hydrochloric acid, condensation was suppressed and the solution remained stable [108,109]. One has to keep in mind, that chloride ions and water may exchange themselves quite frequently due to their high spectro-chemical similarity. The solution was prepared shortly before measurement and subsequently filled into a tubing system equipped with a HPLC pump. From the tubing the solution was introduced by pushing with an HPLC pump into vacuum chamber by micro-jet technique through a 20 µm diameter glass nozzle. The electron and photon signals were taken from the laminar area of the jet which was approximately 2~3 mm in length starting from the nozzle head.

2.3.2 Aqueous Ferrous Solution

For our experiments in section 3.2 $FeCl_2$ tetrahydrate salt (CAS: 13478-10-9) was purchased from Sigma Aldrich Chemie GmbH with > 99% purity. It was later dissolved in de-ionized water ($\Omega \geq 1.8 \cdot 10^7$) to make one molar aqueous solution: The solution was stirred for 10 minutes and then filtered with a Machery-Nagel 619eh filter, providing a retention capacity of at least 4 µm. The measured pH value was 2.75. The color of solution was pale-lime and clear, while the molar ratio of $[Fe(H_2O)_5Cl]^+$ and $[Fe(H_2O)_6]^{2+}$ species is ~77/23 [108,109]. The solution was prepared shortly before measurement and subsequently filled into a tubing system equipped with a HPLC pump. From the tubing the solution was introduced by pushing with an HPLC pump into vacuum chamber by micro-jet technique through a 20 µm diameter glass nozzle. The electron and photon signals were taken from the laminar area of the jet which was approximately 2~3 mm in length starting from the nozzle head.

2.3.3 FePPIX-Cl in DMSO

Both iron(III) protoporphyrin IX chloride (hemin, FePPIX, CAS: 16009-13-5) from bovine (purity > 90%) and the dimethyl sulfoxide solvent (purity > 99%; DMSO) were obtained from Sigma-Aldrich Chemie GmbH. RIXS measurements at the Fe $L_{3,2}$ edge were performed from a solution of 50 mM FePPIX-chloride dissolved in DMSO.

The LiXEdrom endstation equipped with a liquid flow cell [41,110] at the U41-PGM undulator beamline of BESSY II, in Berlin was used. The flow cell incorporates a 100 nm thick Si_3N_4 membrane separating the solution from the vacuum. The energy resolution for the present experiment was set to approximately 0.5 eV at photon energy of 700 eV.

2.3.4 CoPPIX-Cl in DMSO

Co(III) protoporphyrin IX chloride (CoPPIX-Cl, CAS: 102601-60-5) with >98% purity was obtained from Frontier Scientific Inc., and dimethyl sulfoxide (DMSO), >99% purity, was purchased from Sigma-Aldrich Chemie GmbH. A 50 mM solution was prepared by dissolving CoPPIX-Cl in DMSO. This solvent was chosen because higher CoPPIX-Cl concentrations can be achieved than in water which enhances the detected photon-signal intensity. In addition, porphyrin dimerization, which is common in aqueous solution, can be prevented [111,112].

RIXS (and the resulting XA) spectra at the Co L edge were recorded using the LiXEdrom experimental station, equipped with a liquid-flow cell. Total acquisition time for the full $L_{3,2}$ edge XA spectrum was approximately 400 min, and includes measurement of 280 RIXS spectra in the 760-800 eV photon emission range (corresponding to 3d-2p transitions), for 775-803 eV excitation photon energy (at step width of 0.1 eV). In addition, several individual RIXS spectra were recorded at much increased collection time (40 min per spectrum) for improved signal-to-noise which allows identification of specific decay channels. A 100 nm thick Si_3N_4 membrane, which is part of the flow cell, separates the liquid solution from the vacuum inside the main experimental chamber. The energy resolution was set to approximately 0.5 eV, at 775 eV photon energy.

2.3.5 FePPIX-Cl in NaOH

FePPIX-Cl (hemin, CAS: 16009-13-5) from bovine (purity >90%) was obtained from Sigma-Aldrich Chemie GmbH, and further dissolved in 0.5 M NaOH solution to make 0.1 M hemin aqueous solution. The high pH value (from NaOH) helps increase the hemin solubility in water. The porphyrin solution was continuously circulated through a flow cell mounted inside a vacuum chamber during the X-ray measurements to avoid possible beam damage. A 100 nm thick Si_3N_4 membrane was used as the flow cell window to allow X-rays to penetrate in and out [54,106]. UV-vis measurements were carried out on the sample solutions before the electronic structure investigations were conducted by X-ray spectroscopy, to confirm the hemin oligomer structure in liquid (compare Figure 14).

The photons emitted from the sample were collected along the polarization direction of the incident photon beam (to suppress the elastic peak) through a pinhole and subsequently dispersed by a spherical grating with 1200 lines/mm and 7.5 m radius. Finally, the dispersed photons were detected by a microchannel plate (MCP)/fluorescence screen/CCD camera assembly [31]. The flow cell was mounted with its membrane surface at 45° with respect to the incoming and outgoing photon directions. The sample, grating, and photon detector are arranged in a Rowland circle geometry for accurate focusing. The grating and detector chamber was kept at a pressure of 10^{-8} mbar or lower to protect the grating and MCP surfaces from contamination, while the sample chamber was at 10^{-7} mbar. Partial fluorescence yield (PFY) was adopted for XAS measurement in order to reduce self-absorption and saturation effects which are common for total fluorescence yield (TFY) detection [32,113]. The incident photon energy was tuned to the Fe $L_{2,3}$ edge, while only the Fe 3d → 2p transitions were selected for the detection of the emitted photon in both PFY-XAS and XES measurements. The first diffraction order of the grating was chosen due to the low fluorescence yield signal. Since an intense photon flux was focused to a tiny beam spot on the flow cell membrane, thermal effects were inevitable in a long-time exposure of the same sample spot to X-ray [106]. We found though that the spectra remained unchanged if the measurement from a given spot did not exceed 20 min. All spectra presented here are the sum of the measurements obtained from different membrane positions with each having less than 20 min exposure to X-ray.

In order to collect data from the nitrogen K edge the same sample was measured with the micro jet technique. To do so, the hemin powder was dissolved in 0.5 M NaOH aqueous solution and dimethyl sulfoxide (DMSO) solvent to make 0.1 M and 0.05 M hemin

solutions, respectively. The hemin solutions were introduced into a vacuum chamber by liquid micro-jet technique for the X-ray measurements [31,114]. Possible sample damage by intense X-ray beam was effectively avoided since the liquid sample was constantly refreshed. Further data was taken from the solid powder. The powder was spread across a double-sided adhesive copper tape attached to a copper plate which was mounted at 45° with respect to the incident photon beam in the vacuum chamber. The possible radiation damage to the solid samples was minimized by reducing incident photon flux and frequent changing of the measurement spots.

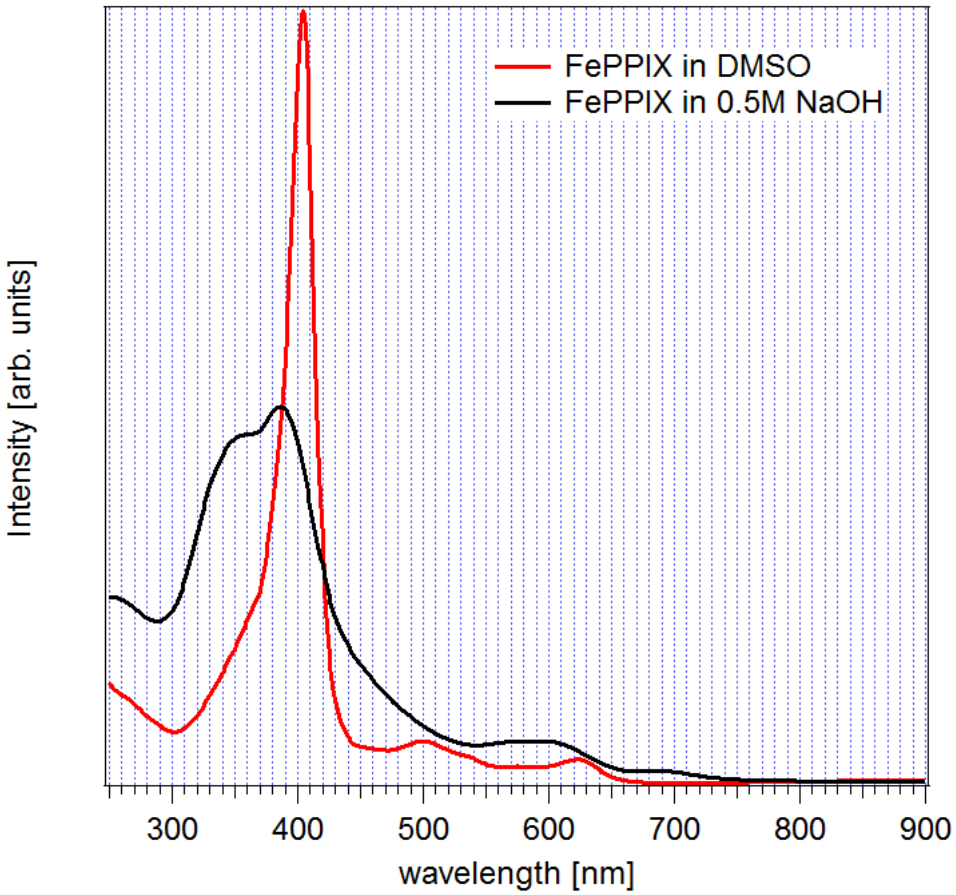

Figure 14. UV-Vis spectra of hemin in DMSO (monomer) and hemin in 0.5 M NaOH aqueous solution (dimer).

2.3.6 MnOEP-Cl and MnTPP-Cl in DCM

For the Experiment in section 4.3 MnTPP-Cl (CAS: 32195-55-4) with 95% purity and MnOEP-Cl (CAS: 28265-17-0) with 97% purity and CH_2Cl_2 (DCM) with ≥ 99.8% purity were purchased from Sigma-Aldrich Chemie GmbH. The porphyrin solutions were

prepared by dissolving MnTPP-Cl and MnOEP-Cl in DCM to reach 50 and 40 mM concentrations, respectively.

The liquid samples were introduced into the vacuum system by the flow-cell technique. A 150 nm thick SiC membrane, which is the window of the flow-cell allowing X-rays to penetrate in and out, separates the liquid solution from the vacuum. RIXS and the resulting PFY-XA spectra at the Mn L edge and N K edge were obtained using the LiXEdrom experimental endstation at the U41-PGM undulator beamline. The energy resolutions of RIXS were approximately 0.8 eV at the Mn L edge and 0.4 eV at the N K edge.

2.3.7 FeOEP-Cl and FeTPP-Cl in DCM

For the Experiment in section 4.3 FeOEP-Cl (CAS: 28755-93-3) and FeTPP-Cl (CAS: 16456-81-8) powder samples with 98% purity purchased from TriPorTech GmbH were dissolved in solvent dichloromethane (DCM) with >99,9% purity from Sigma-Aldrich Chemie GmbH to prepare the solutions of 15 and 25 mM concentrations, respectively.

The porphyrin solution was continuously circulated through a flow cell during the measurements to avoid possible beam damage. A 100 nm thick Si_3N_4 membrane from Silson Ltd was used as the flow cell window to allow X-ray to penetrate in and out. The experiment was carried out at the U41-PGM undulator beamline and the LiXEdrom endstation at the synchrotron facility BESSY II, Berlin.

Partial fluorescence yield (PFY) was adopted for XAS measurements in order to reduce self-absorption and saturation effects which common for total fluorescence yield (TFY) detection [32,113]. The incident photon energy was tuned to the Fe $L_{2,3}$ edge, while only the Fe 3d → 2p transition was selected for the detection of the emitted photon in both XAS (PFY) and RIXS measurements. The first diffraction order of the grating was chosen due to the low fluorescence yield signal. Since intense photon flux was focused to a tiny beam spot on the flow cell membrane, thermal effects were inevitable in a long time exposure of the same sample spot of X-ray. It was found though that the spectra remained unchanged if the measurement from a given spot did not exceed 20 minutes. All spectra presented here are the sum of the measurements obtained from different membrane positions with each less than 20 minutes exposure to X-ray.

2.4 Theoretical Modeling - ORCA Program Package

2.4.1 $[Fe(H_2O)_6]^{3+}$ Complex

Theoretical calculations were carried out for $[Fe(H_2O)_6]^{3+}$ cluster using ORCA program package [115]. Molecular geometry optimizations were performed using the B3LYP density functional method with the def2-TZVP(-f) basis set [116–118]. The geometry calculation had no symmetry constraint, but an octahedral symmetry O_h was reached when the calculation was converged.

Transition energies and moments for the Fe L edge were calculated with density functional theory/restricted open shell configuration interaction singles (DFT/ROCIS) using the same basis set. For DFT/ROCIS calculations, the B3LYP functional together with the parameters c_1 = 0.18, c_2 = 0.20, and c_3 = 0.40 was applied [119]. During the calculations, the resolution of identity approximation was used employing the TZV/J auxiliary basis set [120–123]. Numerical integrations during the DFT calculations were performed on a dense grid (ORCA grid4). The Fe L edge absorption spectrum was simulated by applying a 1.1 eV Gaussian-type broadening on each transition moment and summing up. Vibronic effects were not taken into account in the calculations. The molecular geometries and orbitals were visualized using the Avogadro software [124].

2.4.2 $[Fe(H_2O)_6]^{2+}$ Complex (MOLCAS 8.0)

The calculations for the hexaaqua iron(II) complex were carried on exclusively by the *Molecular Quantum Dynamics Group* of Prof. Dr. Kühn at Rostock University. They used a locally modified MOLCAS 8.0 code [125].

Theoretical calculations were performed for $[Fe(H_2O)_6]^{2+}$ and $[Fe(H_2O)_5Cl]^{+}$ clusters using the restricted active space self-consistent field (RASSCF) method [126] with the relativistic ANO-RCC basis sets [127,128] of triple-zeta quality. The second order perturbation theory correction (RASPT2) was applied on top of RASSCF to account for dynamic correlation. The active space for XAS, RIXS, and PFY calculations included 2p in the RAS1 space (1 hole allowed) and 3s together with 3d orbitals in RAS2 space (full CI). The resulting configuration space includes dipole-allowed 2p → 3d excitations and 3d → 2p and 3s → 2p radiative relaxation transitions. Spin-orbit coupling was treated in

the *LS*-coupling limit [129] taking into account 75 quintet (*S*=2) and 375 triplet (*S*=1) directly interacting states.

RIXS and PFY spectra were evaluated using the Kramers-Heisenberg expression properly including coherence effects and polarization dependence (for details, see Bokarev *et al.* [130]). Valence photoelectron spectra were obtained using the Dyson orbital approach as described by Grell *et al.* [131] with the active space including only 3d orbitals in RAS2 space. A single quintet initial state for $[Fe(H_2O)_6]^{2+}$ and 1 sextet (*S*=5/2), 24 quartet (*S*=3/2), and 75 doublet (*S*=1/2) final states coupled via spin-orbit coupling were included for $[Fe(H_2O)_6]^{3+}$.

2.4.3 Porphyrin Complexes

The porphyrin calculations were carried out with the ORCA program package [115]. Molecular geometry optimizations were performed using the B3LYP [116,117] DFT method together with the def2-TZVP(-f) basis set [118].

Transition energies and moments for $L_{3,2}$ edges were calculated with DFT/ ROCIS using the same basis set. For DFT/ ROCIS calculations, the B3LYP functional together with the parameters $c_1 = 0.18$, $c_2 = 0.20$, and $c_3 = 0.40$ was applied [119]. These three universal parameters are to be distinguished from the empirical parameters in semi empirical molecular-orbital theories. During the optimization calculations, the resolution of identity approximation [120–122,132,133] was used by employing the def2-TZV/J basis set [123]. Numerical integrations during the DFT calculations were performed on a dense grid (ORCA grid4). $L_{3,2}$ edge absorption spectra were obtained from the calculated transition moments by applying a Gaussian-type broadening of 1 eV.

The geometry calculations implied no symmetry. However, for simplicity, the results will be analyzed in terms of square-planar and octahedral point symmetry groups. Vibronic effects were not taken into account in the calculations. The molecular geometries and orbitals were visualized using the Avogadro software [124].

3 Iron Chlorides in Aqueous Solution - a Simple Model System

3.1 Undistorted XAS Probed by Core-Level Emission

Ronny Golnak, Jie Xiao, Kaan Atak, Isaak Unger, Robert Seidel, Bernd Winter, Emad F. Aziz. **Undistorted X-ray Absorption Spectrum Probed by a Core-level Secondary Emission.** *J. Phys. Chem. A (2016)*, DOI:10.1021/acs.jpca.6b01699

Synchrotron radiation based X-ray absorption spectroscopy (XAS) is a powerful experimental technique widely adopted in many scientific disciplines to reveal information of element-specific unoccupied states [83,134]. Secondary emissions, fluorescence yield (FY) or electron yield (EY), are often detected for XAS measurements when primary absorption processes cannot be probed directly in transmission mode [75,83,134,135]. The final XA spectra obtained in this way are in principle the results of the convolution of primary absorption with secondary emission processes, which inevitably brings alterations to the absorption coefficients. Detection of undistorted "true" X-ray absorption spectra is a great challenge due to various distortion effects inherent in the secondary emission measurements that undermine the proportionality of detected signals to absorption coefficients [77,136–138].

The saturation effect, also known as self-absorption effect in the case of FY, is one of the major contributors to the XAS distortions, which has been well recognized and extensively investigated [77,136–140]. This effect is essentially the sample disturbance to the emitted photons or electrons after the completion of relaxation processes in the resonantly excited atoms. EY normally suffers much less saturation distortion than FY due to the very short escape path of electrons when compared with that of X-ray photons in most sample configurations [141]. Multiple solutions have been proposed to mitigate or even completely eliminate the saturation effect. For example, varying the incident and emission angles (for solid samples with a defined surface) or the concentrations of the elements of interest in sample will help reduce the saturation effect for both FY and EY [137]. Alternatively, measuring non-resonant FY from an element that is not resonantly excited in sample, namely inverse partial fluorescence yield (iPFY), is supposed to completely avoid saturation effect [77,136]. In contrast to the extensive studies on the saturation effect which deals with post-relaxation distortions, the relaxation transition itself, radiative or non-radiative, which generally entangles with the absorption process

in the resonant excitation region, is much less investigated for XAS distortions and therefore becomes the focus in section 3.

A few experimental investigations and theoretical analyses have been carried out on the PFY-XA spectra taken from $FeCl_2$ and $FeCl_3$ aqueous solutions in order to reveal the mechanisms during relaxation processes that could lead to XAS distortions [142–146]. The dynamics of the delocalized valence electron and the local atomic effect were both proposed to account for the observed intensity variations at certain XA peaks. However, no solution has been, to my best knowledge, offered so far to reduce or avoid this relaxation distortion. Therefore, it is of interest in this study to unequivocally demonstrate the effect of various relaxation channels on experimental XA spectra, and further propose an experimental method that is free of both relaxation distortion and saturation effect.

In this work, $FeCl_3$ aqueous solution in micro-jet was chosen as a model system to study the XA distortions. Multiple relaxation channels upon the Fe 2p core-hole excitation, including both FY and EY, have been investigated separately. The various radiative and non-radiative decay channels probed experimentally are illustrated in Figure 15. The Fe 2p core-hole after the resonant excitation at the Fe L edge can be filled by all upper occupied orbitals, resulting in emissions of PFY (3s → 2p) and PEY (Auger 3p3p2p, or $L_3M_{2,3}M_{2,3}$) with only core-level orbitals involved in the relaxation processes, and PFY (3d → 2p) and PEY (Auger 3d3d2p, or L_3VV) involving valence orbitals. The 3s3s2p Auger decay is not considered because of a too low signal. The incident photons that resonantly excite the Fe L-edge can certainly excite the O K-edge non-resonantly as well, leading to the so-called iPFY (O 2p → 1s) with spectral dips representing the absorption features at the Fe L-edge. O (2p → 1s) transition, instead of Cl (3p → 2s), is selected as the detection element based on the consideration of the oxygen abundance in the solution which can give rise to intensive signals.

The liquid sample system applied in this study has several advantages over commonly adopted solid films. First of all, the fluidity can significantly unify atomic composition throughout sample surface and bulk, so that the spectral differences between FY and EY, if observed, can be easily attributed to the different decay channels, without considering these two detection techniques being bulk sensitive and surface sensitive, respectively. The surface sensitivity issue is often the complication for solid samples, especially when the solid surface is reconstructed or contaminated [135,147]. The second advantage is that strong orbital overlapping has been demonstrated previously in $FeCl_3$ aqueous solution

between solvated Fe^{3+} ions and their surrounding water shell, which provides an ideal system for the investigation of possible valence electron dynamics [148–150]. Significant variations are expected for the detections of the valence orbital involved emissions when compared to other channels involving core-level orbitals only, as indeed observed in Figure 16 (discussed below). Note that the valence electron dynamics involves both solvated Fe and its coordinated O atoms from water solvent. Consequently, the measured iPFY may be affected as well by the potential charge transfer between Fe 3d and O 2p orbitals since the O valence 2p orbitals are involved in the secondary emissions of iPFY detection. The third advantage is the application of the micro-jet technique that introduces liquid sample into vacuum chambers. The fast refreshing of liquid samples can reduce the surface charging effect significantly. The accumulation of charging is another complication which can cause additional distortions to the EY-XA spectra, as has been already demonstrated previously in solid insulating materials [151].

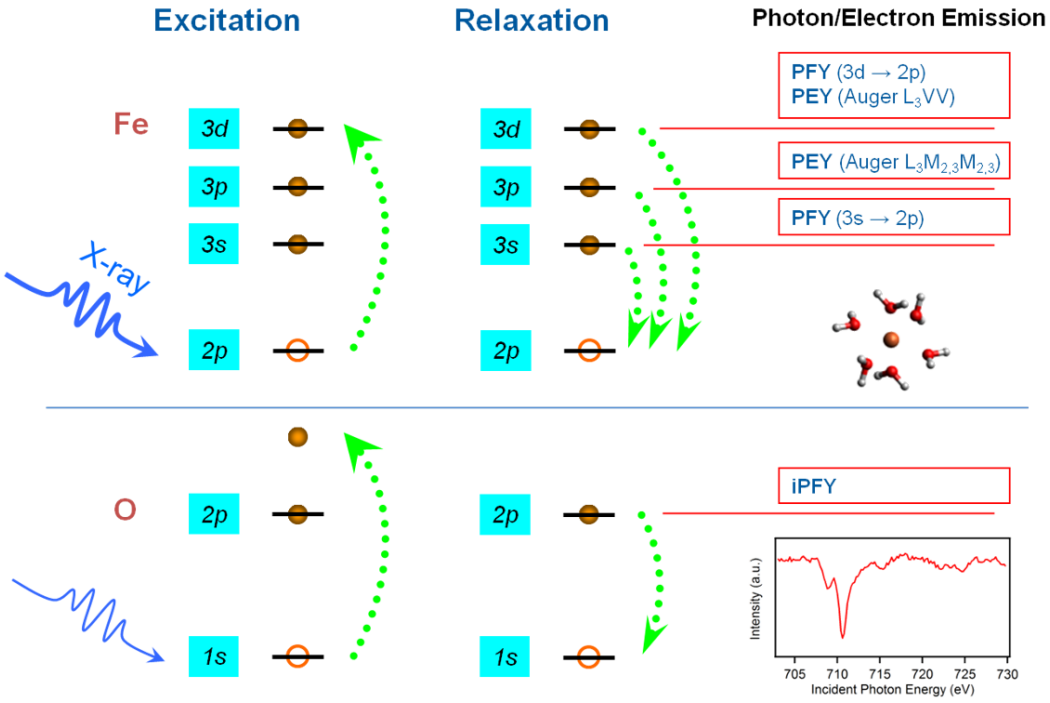

Figure 15. Various secondary emission channels upon resonant X-ray excitation at the Fe L edge and non-resonant excitation at the O K edge in $FeCl_3$ aqueous solution. The solvated Fe^{3+} ion is coordinated by six water molecules in solution, as illustrated in the inset, forming an approximate O_h symmetry. The acquired iPFY spectrum with spectral dips before the data inversion is presented.

The different decay channels can be classified according to the nature of the involve orbitals (core- or valence-level) and emitted particles (electron or photon). Since there are two variables – FY/EY and valence/core – that both influence the final XA spectra, the

comparisons of the XA spectra measured from various secondary emission channels are thus organized into four groups so that in each group the effect only from one variable is manifested, as shown in Figure 16. The differences between valence and core emissions are exhibited in Figure 16a and b by PFY and PEY detections, respectively. The intensity reductions of the first absorption feature at around 709 eV and enhancements of the L_2 edge from the valence emissions (PFY 3d → 2p and PEY 3d3d2p) are apparent in both PFY and PEY measurements when compared to the XA spectra taken from the core-level emissions (PFY 3s → 2p and PEY 3p3p2p). The L_2 edge enhancements, or relatively the intensity reduction at the L_3 edge, of the valence emissions are due to the saturation effect which always reduces the intensity of the most intense peak. The energy carried by the emitted photons or electrons originating from the 3d → 2p relaxation transitions is able to resonantly excite other Fe atoms leading to 2p → 3d absorption, while the emitted photons originating from 3s → 2p transition with the energy of 615 - 630 eV (or electrons generated from 3p3p2p Auger process with the energy of 660 - 675 eV) cannot be re-absorbed resonantly by any elements in the sample. This character makes the non-resonant (core-level) emissions exempt from the saturation effect. The intensity variations of the first absorption feature at 709 eV, on the other hand, exhibit opposite shifts with respect to those at the L_2 edges, implying a very different origin from the saturation effect for this variation. Multiple mechanisms have been proposed to interpret this variation at 709 eV, including delocalized electron dynamics upon X-ray excitation and localized atomic effect [142–145]. Both proposed mechanisms require the involvement of the frontier Fe 3d orbitals in the relaxation processes that causes the intensity reduction at 709 eV and thus leads to the XAS distortion during the relaxation processes.

The above-discussed comparisons for Figure 16a and b have demonstrated the advantages, in both PFY and PEY detections, of core-level emissions over commonly-adopted valence-level emissions for XAS measurements. The following comparisons in Figure 16c and d, on the other hand, uncover the characteristic differences between PFY and PEY in both valence and core regions. Besides being surface sensitivity and high decay probability for PEY when compared to PFY, detection of the valence-involved PEY suffers much less saturation effect than that of the valence-involved PFY, as shown clearly in Figure 16c where PEY (3d3d2p) has much lower intensity at the Fe L_2 edge than PFY (3d → 2p). Coster-Kronig transitions further increase the L_2 edge intensity of the PFY-XA spectrum, making PFY detection less favorable than PEY in the valence

region due to the L_3/L_2 ratio distortion [32]. The post-L_3 edge feature at 712 - 716 eV is related to the Fe 2p spin-orbit coupling (SOC) (confirmed below with the help of the theoretical calculations). Both valence-involved PFY (3d → 2p) and PEY (3d3d2p) in Figure 16c exhibit identical intensity of the first absorption feature at 709 eV, which is not completely unexpected since both detections involve the highly delocalized Fe 3d orbitals [142,148,150]. The delocalized 3d electrons have lower probability to fill the 2p hole within the core-hole lifetime (valence electron dynamics), resulting in state-dependent intensity reductions according to the extent of delocalization [142].

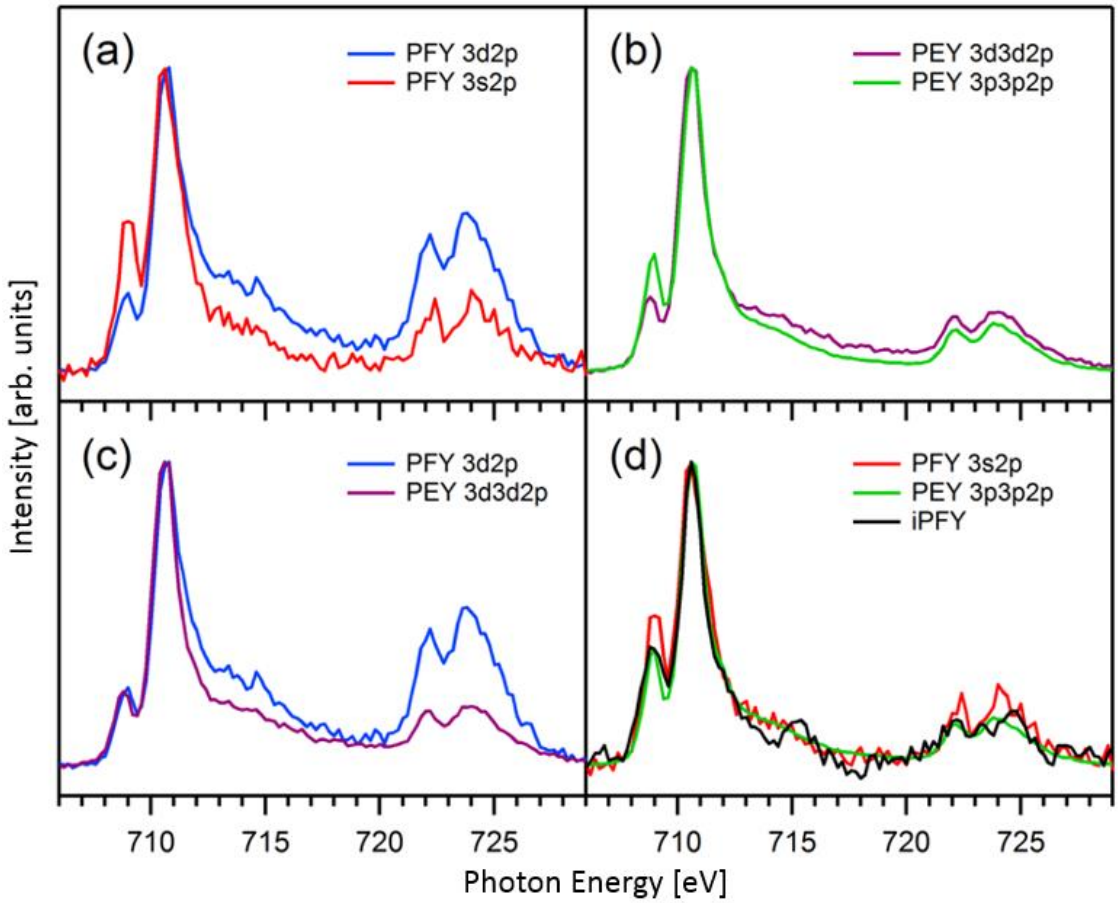

Figure 16. Comparisons of the XA spectra probed by PFY detections from valence and core levels emissions (a), PEY from valence and core levels emissions (b), PFY and PEY both from valence level emissions (c), and PFY and PEY both from core level emissions, as well as iPFY (d).

The valence-related distortion effects (valence electron dynamics and saturation effect) are naturally eliminated in the core-level PFY and PEY which both may be good candidates representing true XA spectrum. The core-level emissions PFY (3s → 2p) and PEY (3p3p2p) exhibit, however, intensity variations at 709 eV and L_2 edge, as shown in Figure 2d, suggesting one of the detection channels might be superior than the other. For the valence-involved emissions, a state-dependent electron delocalization has been

argued previously to account for this intensity reduction at 709 eV, and the intensity of the first absorption feature at 709 eV can, therefore, be regarded as a characteristic indicator signifying the extent of the valence electron dynamics [142]. However, this explanation raised some controversies which argued the local atomic effect from the different emission channels, instead of the delocalized electron dynamics, was responsible for the observed intensity differences at 709 eV and L_2 edge, based on the semi-empirical calculations performed on valence-involved PFY processes [143,144]. For the valence-involved emission processes, these two mechanisms may actually coexist and their respective contribution is still debatable. For the core-level emissions in Figure 16d, local effect must be invoked to account for the observed intensity variations. Since the Fe 3p orbital has non-zero orbital angular momentum, the multiplet effect due to the angular momentum coupling between Fe 3p and 2p can further modulate the final transition cross-sections in the PEY (3p3p2p) process causing additional spectral distortion [130]. The PFY (3s → 2p), on the other hand, can avoid such a distortion due to the s orbital with zero orbital angular momentum and therefore give rise to a true XA spectrum without any distortions.

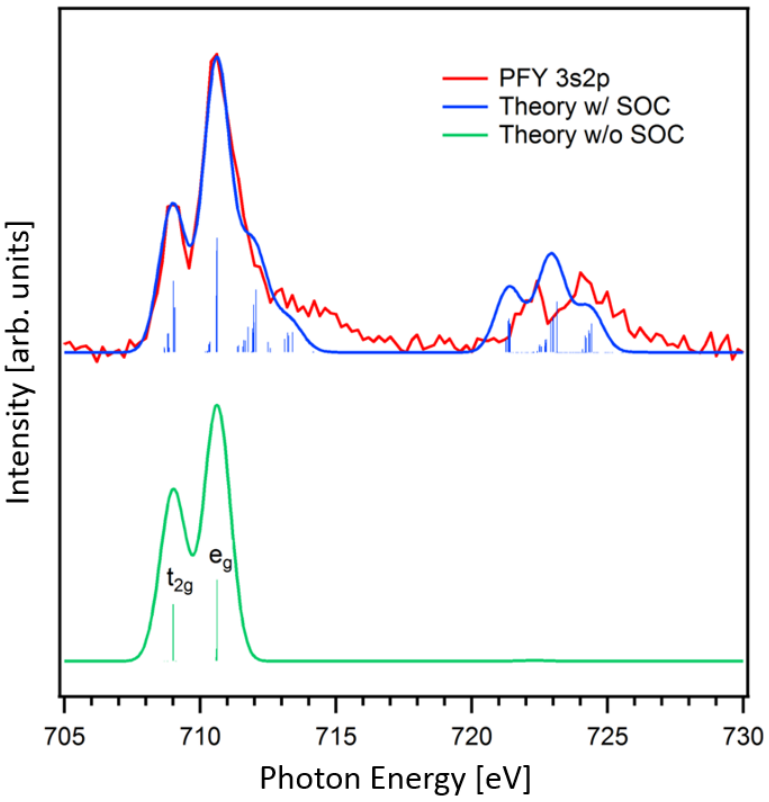

Figure 17. The PFY (Fe 3s → 2p) spectrum (red) compared with the DFT-simulated XA spectra with spin-orbit coupling (SOC) included (blue) and excluded (green). Two major absorption features originating from t_{2g} and e_g orbital contributions are identified by SOC-excluded theoretical analysis.

It is instructive to include iPFY in Figure 16d for further comparison since iPFY was considered previously as the best undistorted detection method [77,136]. The iPFY-XA spectrum is in a good agreement with the spectrum measured by PEY (3p3p2p), and consequently deviates from the PFY (3s → 2p) spectrum at 709 eV as well. Although both iPFY and PEY (3p3p2p) have reduced peaks at 709 eV, the origins of these reductions are quite different. It is the local multiplet effect for the PEY (3p3p2p) as discussed above, while delocalized electron dynamics for the iPFY since the O 2p orbitals in the Fe solvation shell have significant overlap with Fe 3d orbitals [148,150]. The valence-involved iPFY can also distort XA spectrum when some of the valence orbitals of the detected element, O in this case, have strong interactions with the targeted element, *i.e.* Fe, even though the majority of the O atoms in solvent water have no direct interaction with the solvated Fe.

The advanced DFT/ROCIS calculations which simulate the Fe L edge XA spectrum shown in Figure 17 further support the speculations above that suggest the detection channel PFY (3s → 2p) can represent the undistorted XA spectrum at the Fe L edge of the $FeCl_3$ aqueous solution. The theoretical calculations involve only the absorption process between the Fe 2p core level and 3d valence level. The very good agreement between the experimental spectrum and the theoretically simulated one with SOC included (blue trace), especially the agreement of the intensity ratio of the first two leading absorption features at 709 and 710.5 eV, strongly suggests that the PFY (3s → 2p) emission process has no distortion superimposed on the absorption process and therefore can truthfully represent the XA spectrum. The theoretical simulation without SOC (green trace), although comprising much fewer transition moments when compared with the one with SOC, still largely preserves the major absorption features at the Fe L_3 edge, which helps identify the origin of each absorption peak. The comparison between the SOC included and excluded spectra indicate that the post-edge features at around 712 - 716 eV originate from the Fe 2p spin-orbit coupling. The experimental spin-orbit splitting between L_3 and L_2 edges is underestimated in the theoretical calculation, which was reported by Reoemelt *et al* who introduced the DFT/ROCIS method [119]. This effect has, however, no relevance for the interpretation of the current experimental spectrum. As indicated in the SOC excluded spectrum, the first absorption feature at 709 eV originates from the t_{2g} orbitals, while the second feature at 710.5 eV mainly has e_g orbital contributions in an iron-hexaaqua complex with octahedral symmetry O_h. The electron

dynamics and multiplet effect of these different symmetric orbitals are, however, not simulated by DFT method due to our limited computation capability. Despite these drawbacks, the excellent agreement between the experimental data and theoretical simulation in Figure 17 nevertheless provides a strong evidence that the detection of PFY (3s → 2p) emission channel is able to represent the undistorted X-ray absorption spectrum at the Fe L-edge for the prototypic $FeCl_3$ aqueous solution.

The next section 3.2 discuss similar study on $FeCl_2$, but the major focus in the $FeCl_2$ study is on the complementary electronic information uncovered by the combined applications of RIXS and RPES, instead of their integrations as XA spectra discussed in this section.

3.2 Metal-Ligand Interactions Revealed by Combined Probing of RIXS and RPES

Ronny Golnak, Sergey I. Bokarev, Robert Seidel, Jie Xiao, Gilbert Grell, Kaan Atak, Isaak Unger, Stephan Thürmer, Saadullah G. Aziz, Oliver Kühn, Bernd Winter, Emad F. Aziz. **Joint Analysis of Radiative and Non-Radiative Electronic Relaxation Upon X-ray Irradiation of Transition Metal Aqueous Solutions.** *Scientific Reports (2016)*, DOI:10.1038/srep24659

In L edge soft X-ray spectroscopy of TMs, the excitation and ionization of 2p core electrons gives insight into chemical bonding and functionality due to the dipole-allowed probing of frontier d-orbitals. Upon absorption of a soft X-ray photon a 2p core hole is created at the metal center accompanied by the ionization of the solvent, for instance, from the 1s orbital of oxygen in case of aqueous solutions. Subsequent radiative decay channels comprise 3d→2p and 3s→2p pathways, which represent about 1% of the total decay probability for the third-period TMs [152]. The majority channel is due to Auger and other autoionization processes.

In pioneering studies [106,142,153–156], L edge X-ray absorption spectra (XAS) from aqueous TM ions have been reported, based, however, solely on the detection of the total fluorescence yield (TFY). The TFY detection mode corresponds to an action spectroscopy. It enjoys popularity since the direct transmission XAS measurements are challenging for a liquid-jet with a typical diameter of 10-20 µm [29,157–160]. In a TFY measurement, a photodiode is used that integrates the signal from all possible radiative decay channels including the solvent background. However, individual relaxation

channels have not been explored separately, with the 3d→2p being an exception [146,156]. In general, the assumption that the detected TFY signal intensity is proportional to the number of initially absorbed X-ray photons at a given excitation photon energy is not valid [140,161]. There are X-ray optical effects responsible for the deviation between TFY and true XAS signals such as concentration-dependent self-absorption and saturation as well as signal/background ratio variation [150,156]. On a more fundamental level, in order to resemble the first-order XAS the corresponding second-order fluorescence must follow an incoherent two-step model [162], giving the signal as a product of absorption and emission spectra. This holds true only when the interference effects between different radiative decay channels and non-trivial dependence on the polarization of incoming and detected photons can be neglected. This assumption was found to be violated in several studies [163,164]. Moreover, the state-dependent electron delocalization to the neighboring ligands after core-excitation could influence the fluorescence intensity [142,150,156]. Such charge migration processes may occur on a timescale comparable to the few femtosecond lifetime of the core hole [165]. These effects together and our lack of understanding of the role of various decay channels have caused a fair amount of speculations about the electronic structure which often is calculated by semi-empirical theoretical models [83].

Disentangling individual channels requires to resolve the energy of the emitted second-order electrons and photons. This is possible through resonant photoelectron (RPE) spectroscopy for the electron channels and via resonant inelastic X-ray scattering (RIXS) spectroscopy for photon decay channels. In the present contribution, RIXS and RPE experimental techniques are applied together with high-level theoretical calculations in order to explore the complementary character of photon- and electron-emission spectra for the exemplary case of $FeCl_2$ aqueous solution. The focus is on the interplay of the decay channels, which is addressed by detecting state-dependent pathways involving 3d valence orbitals versus stronger-bound 3p and 3s iron orbitals.

The joint analysis of experimental and theoretical spectra provides two key results: First, the question is answered under which conditions partial-yield photon and electron detection can give an accurate measurement of the true X-ray absorption from TM aqueous solutions. Partial fluorescence yield (PFY) and partial electron yield (PEY) spectra are obtained by integration of a signal within photon and electron channel-dependent energy ranges. Second, the basis for back-to-back analysis of RPE and RIXS measurements from the same $FeCl_2$ aqueous solution is established, providing the

assignment of the decay channels and energies of the respective electronic states. It is shown that the joint interpretation of RIXS and RPE spectra for the 3d → 2p channel can considerably contribute to our understanding of solute-solvent interactions.

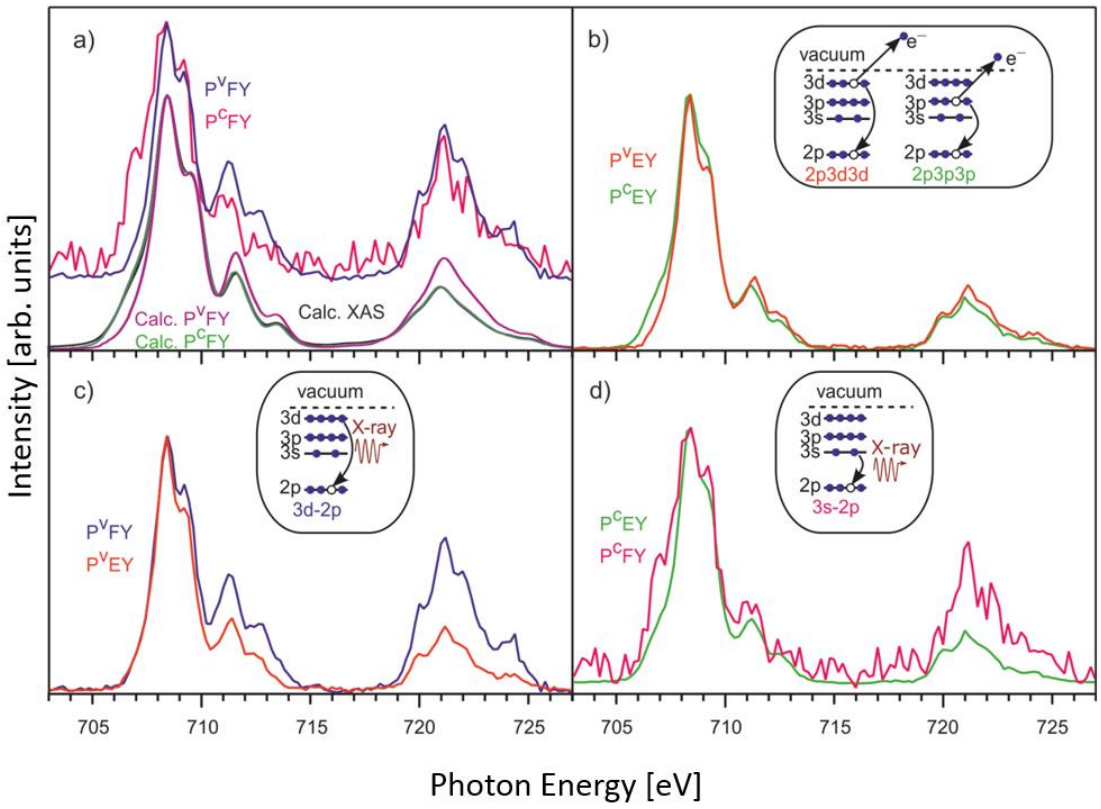

Figure 18. X-ray absorption spectra recorded in PEY and PFY modes for different decay channels. Comparison of a) valence spectra involving 3d core-hole refill; b) core spectra due to 3p (P^cEY) and 3s (P^vFY) relaxations; c) valence and core PEY; d) experimental valence and core PFY versus theoretical XAS and PFY spectra. The corresponding relaxation channels are depicted as insets. All spectra are normalized to the intensity of the highest peak at 708.4 eV to ease comparison.

In general, the XAS obtained in different partial-yield modes contains L_3 (706-715 eV) and L_2 (719-726 eV) edges arising from the spin-orbit coupling of the 2p core-hole created by X-ray excitation. Figure 18 summarizes the PFY and PEY spectra, obtained for the various decay channels as indicated in the insets.

The assignment of the different Auger-electron channels is presented in the appendix 8.1. The specific relaxation channels differ with respect to the refill of the core-hole which can be either from valence- or core-shells. For photon detection, the signal from Fe 3d → 2p and 3s → 2p relaxation channels was integrated over the emitted photon energy within the channel-dependent energy range. Analogously, photoelectron spectra from 2p3d3d and 2p3p3p Auger decay channels were integrated to give PEY spectra.

The different decay channels can be classified according to the nature of the involved orbitals. In PFY (Fe 3d → 2p) and PEY (2p3d3d) the electron, which fills the core hole comes from a Fe 3d valence orbital (spectra are denoted as $P^{v}FY$ and $P^{v}EY$). These 3d orbitals contain the effect of mixing with ligand-centered orbitals. In contrast, in PFY (Fe 3s → 2p) and PEY (2p3p3p) the core-hole refill is by deeper (semi-core) Fe orbitals which do not appreciably participate in the interaction with ligands (spectra are denoted as $P^{c}FY$ and $P^{c}EY$).

The calculated $P^{v}FY$, $P^{c}FY$, and transmission XAS shown in Figure 18 a will serve as reference for the following discussion. The two PFY spectra show distinct differences, i.e. the pre-edge, near 707 eV excitation photon energy is lower while the post-edge at 709-714 eV and L_2 edge is more intense for $P^{v}FY$ than for $P^{c}FY$. The calculated XA and $P^{c}FY$ spectra are essentially indistinguishable from each other. Notice, however, that the calculations did not take into account the X-ray optical effects mentioned above. Nevertheless, both, $P^{v}FY$ and $P^{c}FY$ spectra are in very good agreement with the experimental results that are also shown in Figure 18a.

The difference in the L_3/L_2 edge intensity ratio is usually attributed to several effects. These include self-absorption as well as Coster-Kronig transitions, both enhancing the photon emission at the L_2 edge [32]. The fact that these effects are not included into the calculation points to yet another reason for the difference in the spectra, i.e., the spin-orbit coupling. For the two radiative relaxation channels (3s → 2p and 3d → 2p) core-excited intermediate states are mixtures of the wave functions with different multiplicities due to the strong 2p core-hole spin-orbit coupling, whereas valence initial and final states almost do not mix, and represent pure quintet and triplet states. Thus, the second-order fluorescence process initial → intermediate → final can be described as quintet (ground) → mixed → quintet and triplet, for details see Bokarev *et al.*[130]. This leads to appearance of the new formally spin-forbidden radiative channels for L_3 post-edge and L_2 bands, where spin-orbit coupling is stronger than for the lower energy wing of the L_3 edge [130,142,146]. Since spin-orbit coupling has no effect for 3s orbitals and is notable for 3d orbitals, it leads to distortions of $P^{v}FY$ as compared to the XAS, whereas $P^{c}FY$ is not affected. In the following discussion the focus will be on the L_3 edge only, including its post-edge region.

Compared to the PFY, the $P^{v}EY$ and $P^{c}EY$ spectra (Figure 18b) show similar although less pronounced differences; see also panels c and d of Figure 18. The analysis of the

spin-orbit coupling issue is more involved in case of PEY, since one should consider transitions between mixed intermediate states of Fe^{2+} ion and final valence spin manifolds of the ionized Fe^{3+} system. However, these effects are not considered here.

Another source of differences between PEY/PFY spectra with respect to transmission XAS is the electronic interactions of TM ion with the environment, i.e., solvation-shell water molecules. The excited electron can be further involved in other relaxation processes such as electron delocalization and energy transfer [146,166]. The delocalized excited electron has lower probability to refill the 2p hole within its lifetime (sub-10 fs), and hence the indirect PEY/PFY probe should be state-dependent according to the extent of delocalization and should not track the true X-ray absorption probability [142]. The observed behavior in Figure 18 thus correlates with the orbital extensions: core 3s and 3p orbitals are strongly localized, and are not or barely involved in Fe-ligand orbital mixing. Thus core orbitals have less sources of distortion since delocalization and also spin-orbit channels are of minor importance, while both channels are essential for 3d shell, since 3d and water lone-pair orbitals are considerably mixed. This behavior seems to be generally valid, for another example see Refs. [142,156].

The foregoing discussion has demonstrated the different sensitivity of valence- and core-level relaxation channels to electron delocalization and spin-orbit coupling. Hence, it is not surprising that P^cEY and P^cFY detection (Figure 18c) yields the spectra which are more closely reflecting the true X-ray absorption.

In the following the focus will be on the particular electron- or photon-energy resolved channel involving frontier Fe 3d orbitals. The RPE and RIXS spectra measured at the Fe 2p → 3d resonance are shown in Figure 19a and b, respectively, in a two-dimensional (2D) signal versus incoming photon energy representation. Panels c and d of Figure 19 display four cuts through the 2D spectra in the L_3 edge region at those excitation energies which correspond to main absorption features (Figure 18).

For reference, the RPE spectrum is assigned with the help of the well-understood off-resonant photoelectron spectrum obtained at 705 eV excitation energy (see Figure 19c and Figure 20a). It represents mostly the neat water PE spectrum [167,168] with the features at 11.2, 13.5, 17.3, and 31.0 eV binding energies (BE) being due to ionization from the $1b_1$, $3a_1$, $1b_2$, and $2a_1$ water valence orbitals (blue labels in Figure 20a), respectively. A very weak signal from Fe 3d at 7.09 eV [149] determining the lowest ionization energy of the solution can be also seen.

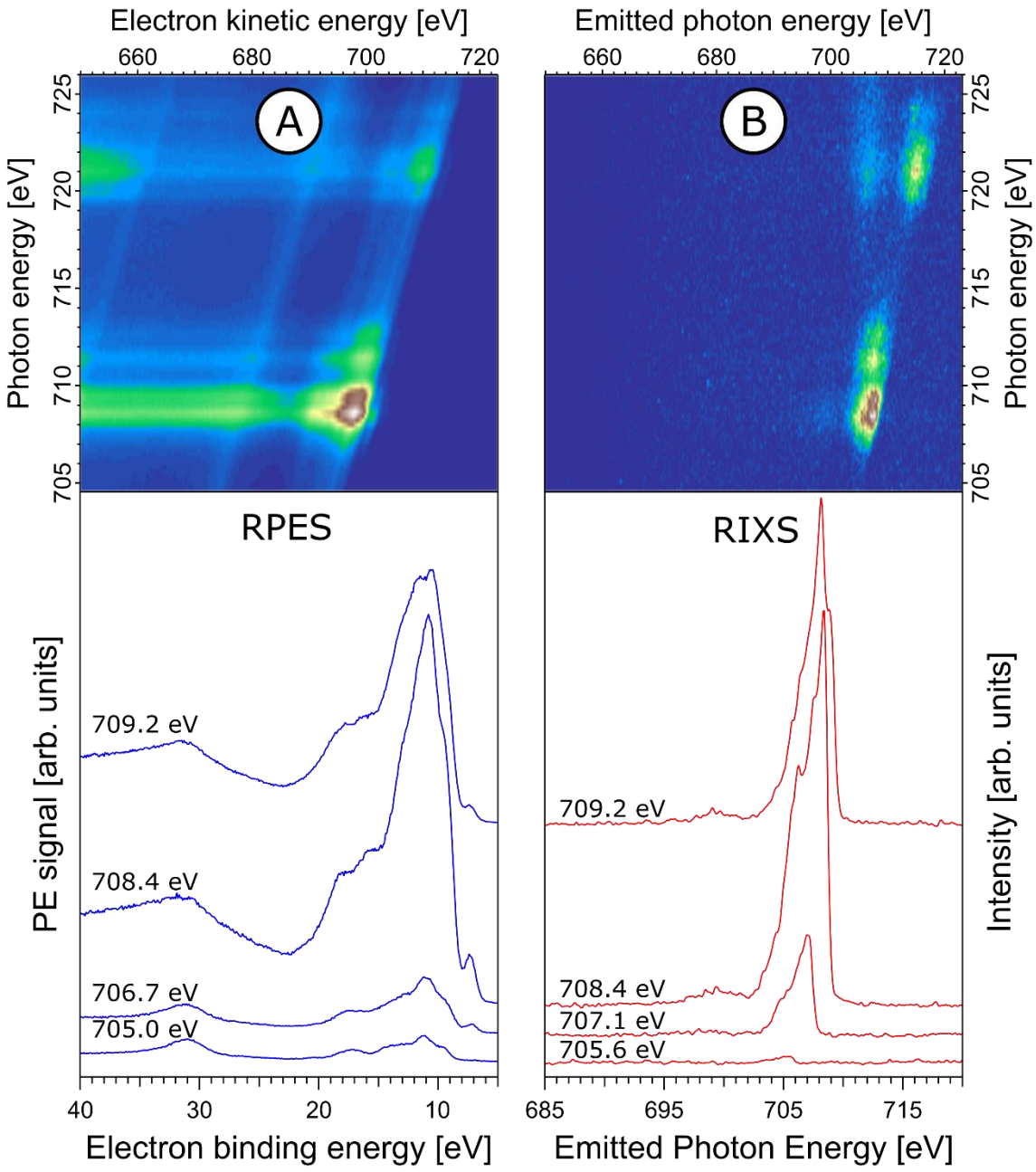

Figure 19. RPE and RIXS due to Fe 3d → 2p relaxation channel. a) 2D RPE as a function of electron kinetic energies; b) 2D RIXS; c) 1D RPE cuts for the selected excitation energies, the electron binding energy is used to facilitate comparison with the RIXS spectra; d) 1D RIXS cuts for the selected excitation energies.

Since the energetic structure of the valence levels does not depend on the excitation energy, it is sufficient to consider resonant spectra measured at maximum absorption, *i.e.*, at 708.4 eV, shown in Figure 20a. The large Auger signal in the ~8-20 eV BE range, occurring for the Fe L_3 edge excitation, mainly arises from the 2p3d3d Auger transition. The Fe 3d orbitals of weakly tetragonally distorted Jahn-Teller d^6 system of approximate D_{4h} point group symmetry split into four components as shown in Figure 20b. According

to the theoretical photoelectron spectrum, the Fe transitions (red labels in Figure 20a) group in three bands: a distinct feature due to ionization of a spin-down (β) electron from the lowest $b_{2g}(\beta)$ orbital at 7.09 eV BE, a broad band comprising numerous main and combination transitions of spin-up (α) electrons from $a_{1g}(\alpha)$, $b_{1g}(\alpha)$, and $e_g(\alpha)$ orbitals overlapping in energy and being centered at 9.5 eV BE, and from $b_{2g}(\alpha)$ at 12.24 eV BE. The $b_{2g}(\beta)$ electron occupying the deepest 3d orbital has the lowest ionization energy because the orbital binding energy is compensated by pairing (exchange) energy. The chloride 3p valence ionization (green labels in Figure 20a) leads to a small contribution around 9 eV BE [168] coinciding with Fe $a_{1g}(\alpha)/b_{1g}(\alpha)/e_g(\alpha)$ feature as well as with the low-binding energy side of the water 1_{b1} orbital signal. The feature at 15.3 eV is most probably due to first-solvation shell water 3_{a1} orbitals, which form σ-bonding combinations with Fe a_{1g} and b_{1g} (d_{z^2} and $d_{x^2-y^2}$) orbitals. Note that the 1_{b2} water signal is also shifted to higher binding energies upon such interactions.

For the resonant excitation at 708.4 eV, the overall RPE signal intensity dramatically increases in comparison to off-resonant region. Moreover, signal increase occurs at the energies of the water peaks 1_{b1}, 3_{a1}, and 1_{b2}, and of the Fe 3d peaks. Such a strong signal enhancement results from the interference of the outgoing electron waves from two simultaneous electron emission processes sharing the same final state (see Figure 20c), and leading to identical kinetic energies of the emitted electrons [82,148]. One process is the direct ionization of the valence orbitals excited by the 708.4 eV energy photon. The other process is the 2p3d3d Auger-electron releasing a 3d electron from the valence level with the same kinetic energy. This interference effect is a clear qualitative and unequivocal evidence of the mixing between iron and water valence orbitals. In case of no mixing, only the Fe 3d signal should be enhanced.

A comparison of RPE and RIXS spectra requires a proper alignment of both spectra on the energy axis. As a consequence of strong correlation effects and pronounced spin-mixing this requires switching from the one-electron orbital picture to the many-electron states picture as illustrated in Figure 20c. The lowest-energy peak in the RPE spectrum is due to the transition between ground states of initial Fe^{2+}(aq) and ionized Fe^{3+}(aq) systems for direct ionization or between the X-ray core-excited state of Fe^{2+}(aq) and the ground state of Fe^{3+}(aq) as shown by blue arrows in Figure 20c. This corresponds to elastic scattering in RIXS when the same core-excited state relaxes back to the ground state of Fe^{2+}(aq) (green arrow in Figure 20c).

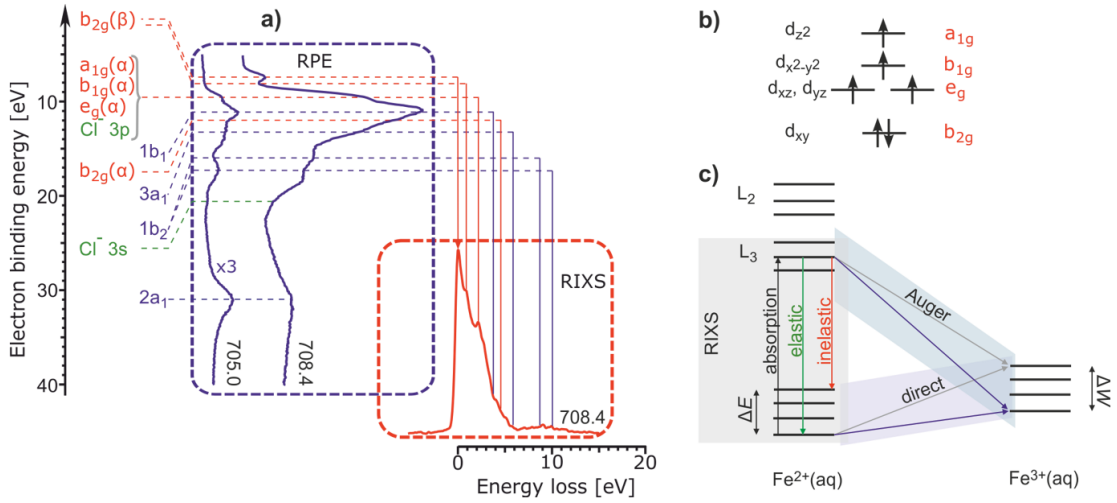

Figure 20. Assignment of RPE and RIXS. a) Aligned RPE and RIXS spectra. Red, blue, and green labels correspond to Fe, H_2O, and Cl^- transitions, respectively. b) Sketch of Fe 3d orbital symmetries for weakly Jahn-Teller distorted system. c) Scheme connecting the corresponding transitions in RIXS (elastic, inelastic) and RPE (both direct and Auger ionization channels).

The alignment of the lowest binding energy RPE feature with the elastic RIXS peak, as is done in Figure 20 a, establishes a common energy reference which allows to connect other features of the two spectra. Let us consider a particular valence excited state. In RPE, it corresponds to the transition to final valence excited state of Fe^{3+}(aq) with the excitation energy ΔW (cf. grey arrows in Figure 20c). Analogously, the inelastic RIXS transition (red arrow) ends up at the valence excited state of Fe^{2+}(aq) with excitation energy ΔE. If electronic relaxation upon ionization $Fe^{2+}(aq) \rightarrow Fe^{3+}(aq) + e^-$ is small and $\Delta E \approx \Delta W$, the present alignment allows the back-to-back comparison and assignment of RPE and RIXS.

According to the suggested alignment, the feature at 2.13 eV loss energy in RIXS is connected with the broad band at 9.5 eV BE in RPE, and thus can be assigned to predominant radiative relaxation from a1g, b1g, and eg orbitals. The RIXS shoulder at around 5.13 eV in accordance with 12.24 eV shoulder in RPE can be ascribed to relaxation from b_{2g} orbital, and a weak band at around 9.0 eV loss energy to weak charge-transfer transitions from first solvation shell water orbitals. The charge-transfer transitions again evidence the orbital mixing between metal and ligand. Remarkably, the 0.9 eV RIXS feature arises from the relaxation of the same $b_{2g}(\beta)$ electron as in the first RPE peak. The energy shift of 0.9 eV can be explained taking into account that in RPE the $b_{2g}(\beta)$ electron is removed from the system completely and its corresponding Coulomb

and exchange energies contribute to ionization energy. In contrast, in RIXS the energy of the final state is determined by the change of the corresponding terms due to excitation of this electron from b_{2g} to other orbitals.

Since RPE and RIXS spectra have different selection rules, having the common reference in energy does not imply that the intensities are the same. This explains the absence of prominent RIXS transitions involving water orbitals. Thus, the intensity differences provide information on the rate of different radiative and non-radiative transitions following the core-excitation.

An assignment of the higher-energy excitations particularly near 712 eV, where the PEY and PFY spectra exhibit substantially different intensities (Figure 18), cannot be made based on the spectra. According to theoretical analysis, this region corresponds to strong mixing between states of different multiplicities and thus is difficult to analyze taking into account different influence of spin-orbit coupling onto electron- and photon-out events.

4 Metalloporphyrins in Solution - a Complex System

4.1 Solvated Metalloporphyrin Monomers

Numerous proteins contain metalloporphyrins (MP) as functional groups, with transition metals in the porphyrin-ring center, allowing for a wide range of biological functions. The latter include oxygen storage and transport (hemoglobin, myoglobin), electron transport (cytochrome oxidase), and energy conversion (chlorophyll), demonstrating photosensitive and catalytic properties [5,40,42]. Due to the diversity of their functions, MPs remain subject of current spectroscopic investigations, porphyrin research continues to be an active field, and there is a focus on the configurational details, bonding, and spin states of the metal center [40,44]. Heme, containing a Fe^{2+} ion in the molecular center, is one of the most important MPs in biological systems, which makes heme an interesting target in porphyrin researches.

For hemin in ethanol total fluorescence yield (TFY) X-ray absorption measurements at the iron L edge [41] (corresponding to electron promotion from Fe 2p to 3d level) revealed that the complex is in a high spin state with iron being five-coordinated by nitrogen (equatorial) and chlorine (coaxial). In the present work, we explore the explicit radiative relaxation channels of core (2p) excited hemin in dimethyl sulfoxide (DMSO) solution. The respective resonant X-ray emission (or often referred to as resonant inelastic X-ray scattering, RIXS [83]) spectra, when integrated as a function of excitation photon energy yield approximately the aforementioned X-ray absorption (XA) spectra. Hence, the RIXS spectra, which contain additional information on the electronic structure of the core-excited solute, are one of the keys for a proper interpretation of XA spectra, solely based on experiment. The other complementary method would be based on the detection of the respective electron-out channel, but such resonant photoelectron studies from low-concentration hemin solutions are yet elusive. In addition to explicitly studying the photon-out channels, we also performed post-Hartree-Fock restricted open-shell configuration interaction singles calculations (ROCIS) combined with density functional theory (DFT/ROCIS method) [119], on the *ab initio* level. As it will be shown, the computational results confirm several key electronic-structure details of the hemin-solvent interactions already identified in a previous TFY-XA study [41]. A major experimental challenge in performing RIXS measurements from hemin in solution is to obtain a reasonably large signal-to-noise ratio given the low solubility of hemin in many

solutions. Yet, larger concentrations are needed to compensate for the several experimental factors associated with using a spectrometer, leading to a reduction of the detected photon signal as compared to a TFY-XA measurement. In the latter case a sensitive photodiode can be positioned at a very short distance from the sample which strongly increases the number of detected photons. The obtained partial fluorescence yield (PFY) XA spectra in the present work require the measurement of many RIXS spectra (over several hours).

In the case of heme the experimental studies are hampered by the instability of the Fe^{2+} ion which may be easily oxidized. Although condensed phase heme can be prepared in situ on metal substrates under ultra-high vacuum condition [169,170], heme molecule in solution eventually oxidizes, forming hemin. From experimental feasibility point of view the substitution of Fe^{2+} by Co^{3+} would arguably be an alternative candidate to study since both ions have $3d^6$ electronic configuration [171,172]. Note that the metal center functionality mainly originates from the valence orbitals at the metal sites. Indeed, cobalt(III) protoporphyrin IX chloride has a rather similar ligand structure as heme, except for the extra chloride attached to the cobalt ion. The local electronic structure of the porphyrin metal centers of Fe protoporphyrin IX chloride (FePPIX-Cl, hemin) and Co protoporphyrin IX chloride (CoPPIX-Cl) in liquid solution will be studied in sections 4.1.1 and 4.1.2, respectively.

4.1.1 FePPIX-Cl in DMSO

Kaan Atak, Ronny Golnak, Jie Xiao, Edlira Suljoti, Mika Pflüger, Tim Brandenburg, Bernd Winter, Emad F. Aziz. **Electronic Structure of Hemin in Solution Studied by Resonant X-ray Emission Spectroscopy and Electronic Structure Calculations**. *J. Phys.Chem. B (2014),* DOI:10.1021/jp505129m

There is a strong correlation between molecular geometric structure and spin state, and the N-Fe-N bond angle is found to be dependent on the spin multiplicity of the porphyrin complexes [45]. Depending on the chemical environment, different spin states can coexist, and additionally the spin state may change (spin crossover) [46] as a function of ligand coordination [47]. Understanding these mechanisms is extremely important for unraveling the transport properties of these biomolecules [41].

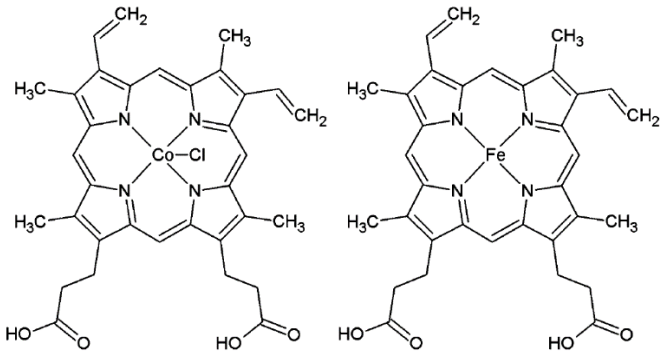

Figure 21. The structural formula of CoPPIX-Cl (left) and the heme (right).

For a description of the local electronic structure governing these properties, the orbital mixing between the transition metal ion and the surrounding porphyrin ring has to be investigated. From the experimental side, soft-X-ray spectroscopy is ideally suited for this purpose, providing an unprecedented sensitivity to local electronic structure, and is applicable for in situ investigations [48,49]. For hemin in ethanol total fluorescence yield (TFY) X-ray absorption measurements at the iron $L_{3,2}$ edge [41] (corresponding to electron promotion from Fe 2p to 3d level) revealed that the complex is in a high spin state with iron being five-coordinated by nitrogens (equatorial) and chlorine (coaxial). The present experiment investigated the explicit radiative relaxation channels of core (2p) excited hemin in dimethyl sulfoxide (DMSO) solution. The structural formula of the FePPIX-Cl (heme) and CoPPIX-Cl are shown in Figure 21. The respective resonant X-ray emission (or often referred to as resonant inelastic X-ray scattering, RIXS [83]) spectra, when integrated as a function of excitation photon energy yield approximately the aforementioned X-ray absorption (XA) spectra. Hence, the RIXS spectra, which contain additional information on the electronic structure of the core-excited solute, are one of the keys for a proper interpretation of XA spectra, solely based on experiment. The other complementary method would be based on the detection of the respective electron-out channel, but such resonant photoelectron studies from low-concentration hemin solutions are yet elusive. In addition to explicitly studying the photon-out channels, post-Hartree-Fock restricted open-shell configuration interaction singles calculations (ROCIS) combined with density functional theory (DFT/ROCIS method) [119], on the ab initio level were performed. As it will be shown, the computational results confirm several key electronic-structure details of the hemin-solvent interactions already identified in a previous TFY-XA study [41]. A major experimental challenge in performing RIXS measurements from hemin in solution is to obtain a reasonably large signal-to-noise ratio

given the low solubility of hemin in many solutions. To this end, dimethyl sulfoxide solvent is a compromise, as it can be obtained 50 mM concentrations which is more than 15 times larger than in our total-yield study of reference [41]. Yet, this larger concentration is insufficient to compensate for the several experimental factors associated with using a spectrometer, leading to a reduction of the detected photon signal as compared to a TFY-XA measurement. In the latter case a sensitive photodiode can be positioned at a very short distance from the sample which strongly increases the number of detected photons. In fact, the obtained partial fluorescence yield (PFY) XA spectrum in the present work, which requires the measurement of many RIXS spectra (over many hours), is not as well-resolved as the TFY-XA spectrum of reference [41].

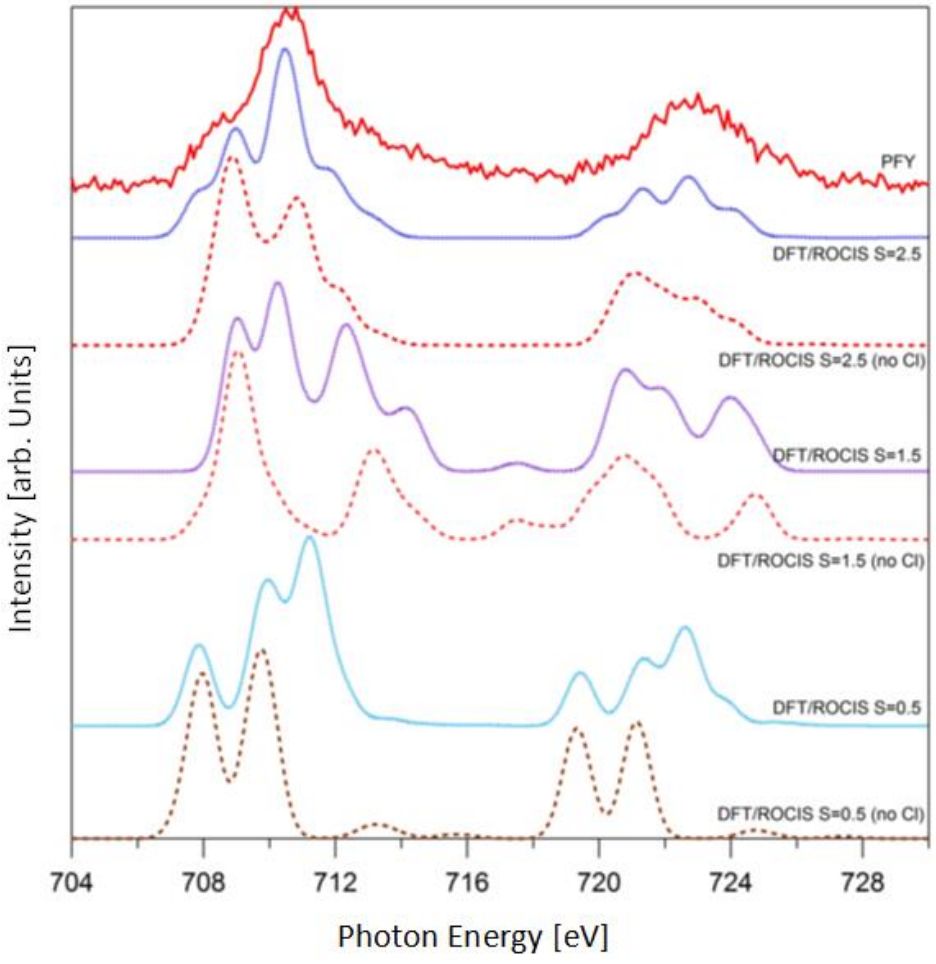

Figure 22. Experimental iron L edge PFY spectrum (top red tier) of 50 mM FePPIX chloride solution in DMSO, compared to DFT/ROCIS XA spectrum calculations for different spin multiplicities, with chloride present and absent, respectively. The blue sticks represent the intensities of individual transitions. In the top tier, (a), (b), and (c) refer to the main absorption features discussed here.

It is convenient to first consider the PFY-XA spectrum of Fe at the $L_{3,2}$ edge, measured here, with the grating set to the first order diffraction. The result is shown in Figure 22,

top tier for the reason of low concentration, as mentioned earlier, the signal-to-noise ratio of this spectrum is considerably less than the TFY-XA spectrum from hemin in ethanol reported in reference [41]. This has no effect on the current work though where one goal is to determine the electronic structure of hemin in solution, from ab initio theory. Individual RIXS spectra, from which the experimental XA spectrum of Figure 22 is obtained through integration of the RIXS signal intensities, will be addressed later.

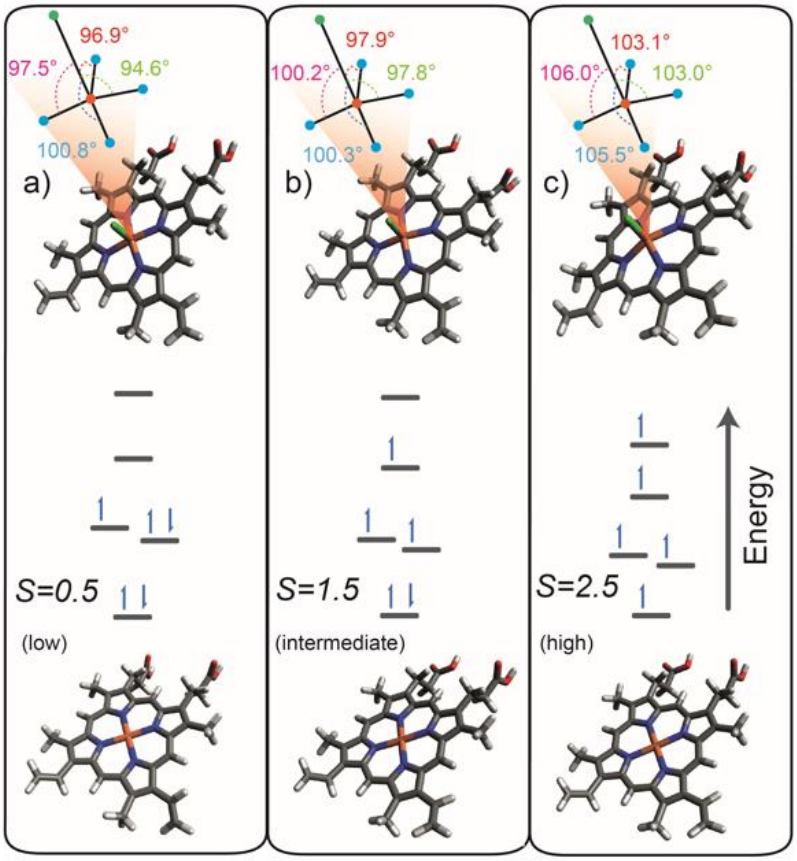

Figure 23. Simplified singly occupied iron d-orbital energy diagrams of the three different spin states and the molecular geometries of Fe(III) protoporphyrin IX with and without a chloride at the top and the bottom, respectively.

The survey will be started by theoretical simulation and the effect of the existence of a nearby Cl^- anion on the iron spin state and how this reflects in the spectra. The approach is simple, treating spin state as a parameter, while the study of the explicit molecular interactions between solute and solvent is excluded. Although it is already suggested in reference [41] that Cl^- does not dissociate and that the high spin state 2.5 is assumed (the ground-state electronic configuration of Fe^{3+} is $3d^5$), it is yet instructive to explore the effect of a hypothetical spin state on the XA spectrum. The theoretical XA spectra obtained from DFT/ ROCIS calculations are shown underneath the experimental

spectrum in Figure 22. Results for spin states S = 2.5, 1.5, and 0.5, calculated with the Cl^- present and absent, respectively, are presented in the several tiers of the figure. Spectra are normalized to the highest intensity feature at the L_3 edge. The calculations show that the high spin case (S = 2.5), with chloride bound to the molecular ring, matches best with the experimental spectrum, in agreement with reference [41]. Interestingly, the results are inconsistent with conclusions based on UV-Vis spectrophotometry studies which suggest that in DMSO solution the chloride is dissociated from FePPIX [112,173].

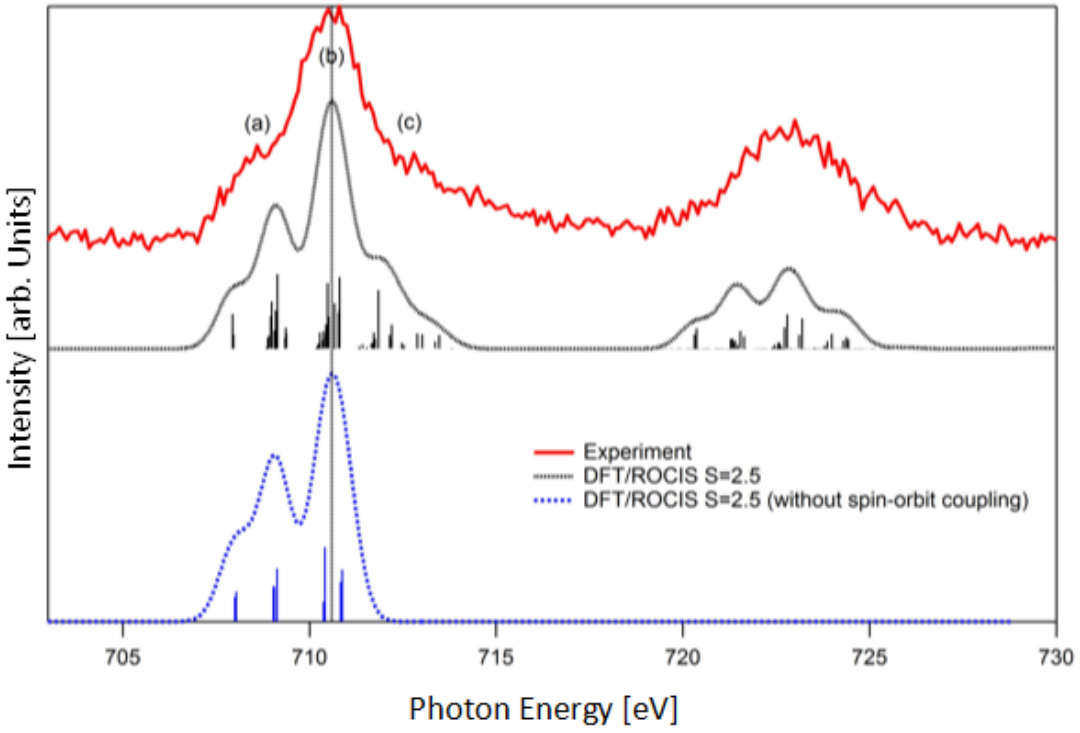

Figure 24. Experimental Fe L edge PFY spectrum of 50 mM FePPIX chloride solution in DMSO and DFT/ ROCIS XA calculations for spin multiplicity 6 with the presence and absence of spin-orbit coupling effect. (a), (b), and (c) refer to pre-maximal, maximal and post-maximal features respectively.

Computed structures are shown in Figure 23 within the same DFT calculations for a visualization of spin state on geometry. It is seen that the effect of spin state on the molecular structure is more pronounced when chloride is included. In the higher spin-state structures the iron tends to pull away from the molecular ring plane; this is reflected in the increasing N-Fe-Cl bond angles in Figure 23 (and in the table under appendix 8.1). The smaller effect of spins on structure in the absence of Cl^- is best visualized through the numerical values of the Fe-N bond distances, presented in table under appendix 8.1. So far the XA spectrum from hemin in solution is simulated without an assignment of the peaks in the experimental PFY-XA spectrum of Figure 22 (top tier) to actual electronic

transitions. For this one first calculate the transition energies in the absence of spin-orbit coupling (SOC), and then include SOC as a perturbation. Results for the SOC-excluded case are presented in Figure 24; states are well-defined and can be readily assigned to the experimental peaks. In contrast, inclusion of SOC, which is the more accurate description as one has seen previously, leads to an absorption spectrum characterized by thousands (>5000) of ionic multiplet states [174], indicated by sticks in the second top tier of Figure 22. A specific orbital-character assignment of this large manifold of spin mixed states is elusive. The analysis shows though (compare Figure 24) that the prominent transitions, represented by the bars, appear at very similar energies for both SOC included and excluded; in the latter case these states are however more spread, and each individual state contributes less to the total spectrum. For our further electronic structure analysis it is thus sufficient to just consider the well-assigned orbitals of the SOC excluded calculations. One can then employ a simpler one electron picture description for interpreting the MO character and bonding structure. The actual computed spectrum results when representing each energy value by a Gaussian of 1 eV width; furthermore, calculated energies were shifted ad hoc by +17.5 eV in order to match with experiment. Such an energy shift is due to the intrinsic shortcomings of the density functional used here [119]. In the calculations done here one also finds a similar ~1 eV underestimation of the energy difference between the L_2 and L_3 edges as reported by Roemelt et al. [119], who introduced the DFT/ ROCIS method. This effect has no relevance for the interpretation of the experimental spectrum.

The experimental L_3 edge PFY-XA spectrum of Figure 22 exhibits three main features, a maximum peak at 710.5 eV (label b), a shoulder at 708.3 eV (label a) on the low-energy side, and another shoulder near 712.8 eV (label c) at the high-energy side. These are the same features reported in a previous total yield study [41], although peaks are less resolved in the present partial-yield study; see the given reasons. The resolution in the L_2 edge region is not high enough to clearly distinguish the discrete features, appearing here only as repeating faint structures at 720.8, 722.8, and 725.0 eV. To assign the features of the L_3 edge XA spectrum to electronic transitions, one can return to the computation scheme described in the previous paragraph, and for the reasons mentioned above one has to consider the S = 2.5 case with SOC excluded. Calculated energies are presented in Figure 24. Four energy positions can be identified where prominent transitions occur, 708.0, 709.1, 710.4, and 710.9 eV. The first two constitute the feature a, and the two latter

transitions form the feature b of the experimental XA spectrum. If one compares from the table, presented in appendix 8.3, one can argue that the computed molecular-orbital (MO) characters for the MO 167 is responsible for the first transition which itself is the first singly occupied molecular orbital (SOMO). The second transition is comprised of MOs 168 and 169, implying a very small energetic difference between these orbitals in the core-hole-excited state. The last two transitions are due to MOs 170 and 171, respectively. All five MOs (167−171) are singly occupied iron d-orbitals constituting the π* and σ* antibonding MOs which will be discussed later. The computational results do not indicate any significant contributions from transitions involving unoccupied MOs; these are the ones with numbers ≥ 172. Unlike peaks (a) and (b), peak (c) is only reproduced (see appendix 8.2) when SOC effects are included which allows for mixing of orbital spins, causing the aforementioned multiplet structure.

The five SOMOs, identified in the previous paragraph, which give the XA spectrum its characteristic shape deserve more attention due to the information they provide on bonding. Here one refers back to the table of appendix 8.3 where the atomic contributions from Fe and from nearest neighbors are presented; one also explicitly quantify the d-orbital contributions from Fe using Löwdin population analysis. The identified five orbitals are seen to be primarily iron d-orbitals with antibonding character; see also the figure of appendix 8.4 which presents the MO energies and spatial distributions for these orbitals. According to the population analysis, higher-energy unoccupied orbitals have significantly more ligand character. In the absorption process, the involvement of these orbitals would imply metal-to-ligand charge-transfer transitions; however this is not the case. The antibonding MOs 167-171 hint at σ and π bonds in the form of bonding MOs (table in appendix 8.3). However, similar to the findings by Hocking *et al.* [51] for $[Fe(tpp)(ImH)_2]^+$ involving ferric Fe, back-bonding cannot be unequivocally identified. This supports the conclusion that hemin solvated in DMSO is in the high spin state since back-bonding would increase the bond strength between the TM ion and the ligands, likely causing larger orbital splitting and hence leading to a low-spin state. It should be also noted that the actual symmetry of the ligand structure is inferred here from experiment and computation, combined. Peak (a) in the experimental spectrum implies degeneracy of d_{xz}-based and d_{yz}-based orbitals (observed in both the DFT/ROCIS and the single-point calculations; check again table in appendix 8.3) which is indicative of C_{4v} symmetry ligand structure. An octahedral ligand field, for instance, causing low-spin

configuration would lead to a considerably different shape of the XA spectrum, inconsistent with experiment.

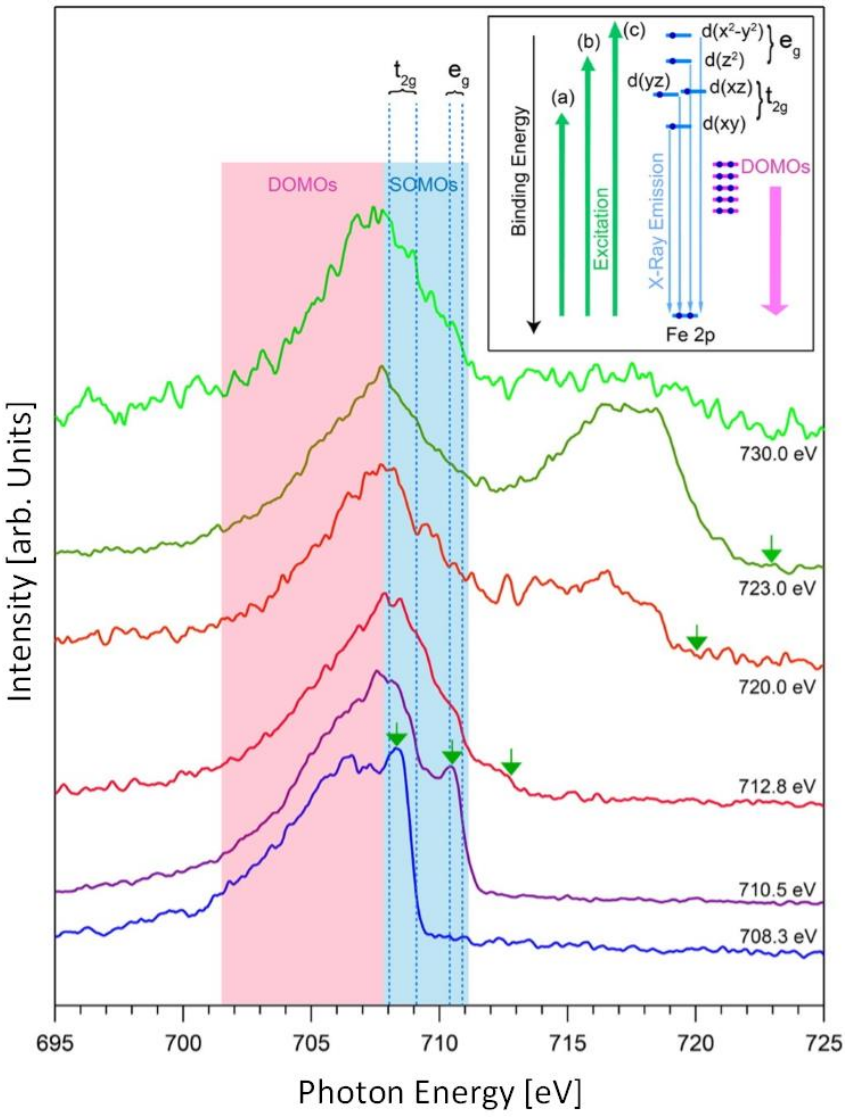

Figure 25. Fe L edge RIXS spectra from 50 mM FePPIX chloride solution. The inset is a simplified schematic representation of observed X-ray excitation and de-excitation transitions.

One can focus now onto the RIXS spectra presented in Figure 25 and extract the additional information on electronic structure these spectra provide. Here the focus is on the L_3 edge. These spectra were measured separately, for an extended collection time (~1h per RIXS spectrum) at the photon energies corresponding to aforementioned pre-absorption (a), main absorption (b), and post-absorption (c) energies, at 708.3, 710.5, and 712.8 eV, respectively. Note that the full-range PFY-XA spectrum in Figure 22 has been obtained for a much shorter acquisition time per RIXS spectrum, but many more spectra were recorded (in steps of 0.1 eV excitation photon energy) over the same photon-emission range as displayed in Figure 25. Simulation of L edge RIXS spectra has not yet

been incorporated into the ORCA suite (refer to ORCA manual) [115] and one has to attempt an interpretation of the experimental RIXS spectra using a simplified orbital picture combining the results of single-point DFT and DFT/ROCIS calculations.

Qualitative inspection of the L_3 edge RIXS spectra reveals an almost identical emission spectrum in the approximately 700-712 eV photon energy range. This is clear experimental evidence that 3d-3d and 3d-2p electron correlation is rather weak, which is a surprising result for this 3d metal complex. Note that the higher energy part of the emission spectrum (shown by blue shading) is absent for the pre- and main-edge excitation, in which case this energy region coincides with the inelastic emission peak (shown by the small arrows in the spectra). The large intensity of the elastic peak for the lower excitation energies is in line with our previous findings for simpler Fe complexes [146].

Intensity in the 715-720 eV region, occurring in the three uppermost RIXS spectra, arises from L_2 edge excitation but is not further considered here. For a more quantitative interpretation of the RIXS spectra we consider the energy level diagram shown as an inset in Figure 25. Here the three main excitations are depicted, at energies (a), (b) and (c) of the XA spectrum (of Figure 22), along with the calculated Fe 3d energies (from DFT/ROCIS and ignoring the SOC originated L_2-L_3 separation), and one also can include the doubly occupied molecular orbitals (DOMO). These latter orbitals have both Fe and ligand contributions (compare with the table in 8.3 and with the figure in 8.5)and are thus interpreted as ligand-to-metal charge-transfer transitions (LMCT). Fe 2p to valence excitations are represented by the green arrows, and the radiative decays are illustrated by blue (transitions from SOMOs to Fe 2p) and red (transitions from DOMOs) arrows, respectively. As depicted in the diagram, post-edge excitations, at 712.8 eV (and all higher excitation energies), lead to the population of all SOMOs, d_{xy} through $d_{x^2-y^2}$, and emission from each one can be expected. These transitions correspond to the high-energy side (blue shaded) of the experimental RIXS spectra, and here we notice a very good quantitative agreement between experiment and theory. It is obvious from the calculated energies that the low energy side (red shaded) of the emission band of Figure 25 must be due to the valence DOMO → Fe 2p transitions, and one can in fact determine the valence DOMO energies from the experimental emission energies. This would put the emitting DOMOs in a 6 eV energy band lying below the SOMO energies. The fact that experimental energies are well-matching with the relative energies determined here

(see appendix 8.3, 8.4 and 8.5) is another indication of the previously mentioned small 3d correlation, or alternatively the extra charge being smeared out due to the high density of states.

4.1.2 CoPPIX-Cl in DMSO

Kaan Atak, Ronny Golnak, Jie Xiao, Mika Pflüger, Tim Brandenburg, Bernd Winter, Emad F. Aziz. **Co(III) protoporphyrin IX chloride in solution: Spin-state and metal coordination revealed from resonant inelastic X-ray scattering and electronic structure calculations.** *Phys. Chem. Chem. Phys. (2014)*, DOI:10.1039/C4CP04703F

In order to probe the local electronic structure of the metal center of CoPPIX, soft X-rays were applied to resonantly excite cobalt 2p electrons into the partially occupied 3d levels. In tuning the photon energy across the full (L edge) absorption band, we obtain a series of resonant X-ray emission spectra, also referred to as resonant inelastic X-ray scattering (RIXS) spectra [175,176]. Here, specifically dipole allowed transitions from the various Co 3d-character states to the 2p core level (within an approximately 20 eV energy window) were detected. The intensity of a given spectrum reflects the relative X-ray absorption cross-section. That is, signal integration of the RIXS spectra as a function of excitation photon energy delivers one possible partial-fluorescence-yield (PFY) XA spectrum, with a large sensitivity to valence electron delocalization, in the present case. As is also the case for other X-ray absorption measurements based on secondary processes (such as inverse fluorescence [77] or electron emission [148]) these partial-yield XA spectra as well as total-yield spectra (not considered though in this work) may however differ from the true absorption spectra obtained in a transmission measurement. Differences are due to the fact that certain fluorescence channels may compete with other non-radiative relaxation pathways, and hence the observed fluorescence is not exactly proportional to the number of absorbed photons [156]. We note though that these effects are likely to be minimized if one probes 2p core-level refills involving transitions from deeper (core) levels, e.g. 3s, because of too low signal intensities, owed to low solute concentration; these channels are not investigated here. In the present work the PFY-XA spectra are discussed with the help of a newly developed hybrid calculation method of density functional theory/restricted open-shell single excitation configuration interaction (DFT/ROCIS) [115,177] that simulates the XA spectra at the Co L edge. Local coordination and spin-state character of the cobalt center can be extracted by comparison of the experimental data with the theoretical calculations; this is analogous to the chapter 4.1.1 and to a recent

article on hemin [178]. The theoretical interpretation of the XA spectra is complemented by the rather qualitative analysis of the RIXS spectra which allows for an experimental identification of electronic decay channels, corresponding to the specific transitions from occupied and unoccupied orbitals to the cobalt 2p core levels. Experimental (relative) energies, including the local HOMO-LUMO gap, are discussed with respect to the calculated energies at the ground state.

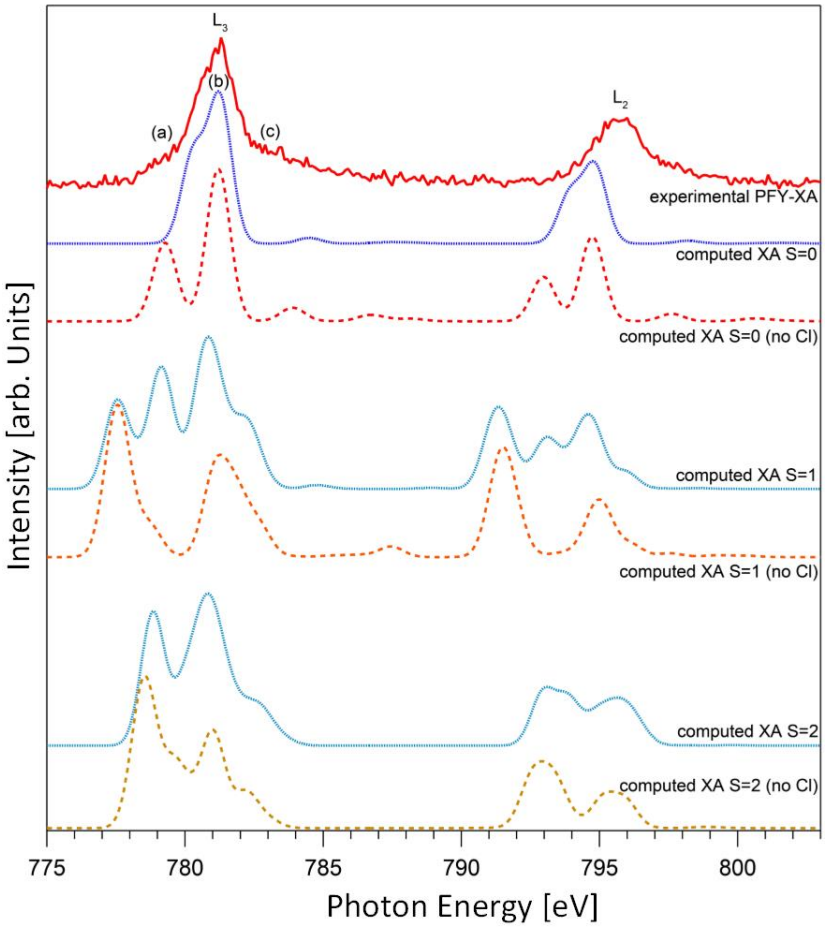

Figure 26. Experimental Co L edge PFY-XA spectrum (top red trace) from a solution of 50 mM CoPPIX-chloride dissolved in DMSO, along with the computed (using DFT/ROCIS) XA spectra for different spin multiplicities, in the presence and absence of chloride, respectively. Labels (a)-(c) refer to the photon absorption energies for which the RIXS spectra will be presented.

It is useful to first address the Co L edge PFY-XA spectrum from the CoPPIX-Cl/ DMSO solution, determine the energies of the most probable 2p-3d transitions, and explore the Co^{3+} ($3d^6$) spin multiplicity and possible ligand coordination. The experimental PFY-XA spectrum is presented in Figure 26, top trace, and for comparison are also shown six theoretical XA spectra accounting for various spin states and Co coordination. Since Co^{3+} has $3d^6$ electron configuration, the spin multiplicity 2S + 1 may adopt values 1, 3, 5, with

S = 0, 1, 2, corresponding to an all-paired electron system (S = 0), a two-unpaired electron system (S = 1) and a four-unpaired electron system (S = 2), respectively. In addition, for each hypothetical spin state (the actual spin state is yet to be discussed) we also look at the effect of chloride being attached or not. This latter aspect is motivated by previous works on hemin in DMSO, reporting that chloride detaches from the Fe^{3+} center [112,173]. The respective geometric structures, shown in appendix 8.6 were first optimized by DFT calculations, and then transferred into the DFT/ROCIS routines to simulate XA spectra. It is seen from Figure 26 that the spectrum for S = 0, and chloride attached (structure A of the figure in appendix 8.6), matches the experiment best. Another important observation from Figure 26 is that the spectral shape is very sensitive to both spin state and Co-Cl coordination. The four simulated spectra for S 4 > 0 tend to exhibit an overall richer structure, dispersed over a larger energy range. However, the simpler structure for the S = 0 case is in better agreement with experiment. Spin state has also a quite pronounced effect on the molecular structure; the effect of increasing spin state on the geometric structure of CoPPIX-Cl is a slight protrusion of Co above the molecular plane (Figure in appendix 8.6, top view). Numerical values of theses bond distances and also of the respective bond angles are presented in appendix 8.7.

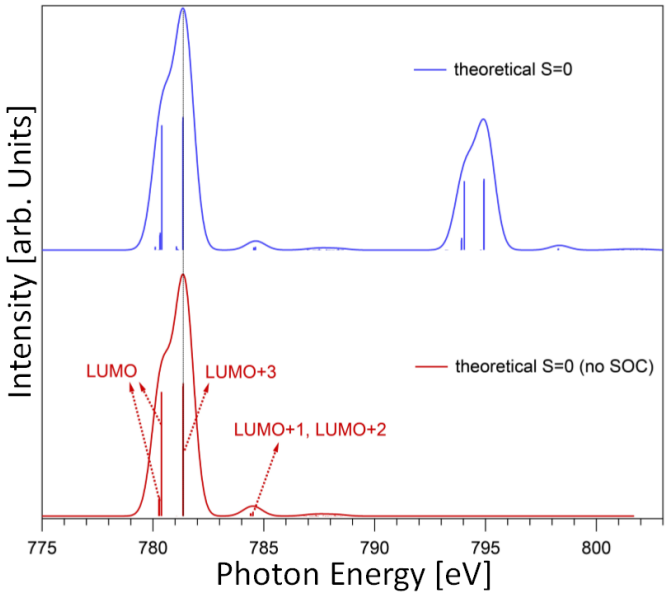

Figure 27. Computed (using DFT/ROCIS) cobalt L edge XA spectra for CoPPIX-Cl: S = 0 in the presence (blue trace) and in the absence (red trace) of spin-orbit coupling, respectively. Vertical sticks mark the calculated transition moments. The computed spectra are shifted ad hoc by 16.35 eV (blue trace) and 11.7 eV (red trace).

In order to determine the molecular orbital (MO) contributions to the individual X-ray absorption transitions, a computed spectra without spin-orbit coupling is used again, like

in the chapter before. Figure 27 (upper trace) shows the best matching simulated spectrum from Figure 26, i.e., the blue trace for low-spin S = 0 state and 5-coordination, along with the respective calculated transition moments as vertical bars. In addition a calculated spectrum with spin-orbit-coupling (SOC) excluded is inserted with its individual transition moments, shown in the bottom of Figure 27. In this latter case assignment of the transition moments to individual MOs is much facilitated as the number of transitions reduces from hundreds (SOC-included, upper trace) to dozens. Such a simplification still correctly describes the overall orbital character, and preserves almost all spectral features at the Co L_3 edge, as is also demonstrated in the previous chapter [178]. One has to note that the simulated spectra along with their transition moments (vertical bars) were adjusted in energy in order to match the experimental spectrum. Furthermore, the spin-orbit splitting of the Co 2p level (L_3-L_2 energy difference) is underestimated by ≈ 1 eV. These shortcomings are intrinsic to the DFT/ROCIS method [119] but insignificantly affect the interpretation. The analysis below will reveal the details of the absorption peak (Figure 27, bottom), and it will be constructed a local electronic structure map around the cobalt ion.

Population analysis by DFT calculations for the 5-coordination structure, and S = 0, reveals both the atomic contributions from Co and its nearest neighbors to the MOs, as well as the percentage of different Co d-orbitals within the considered energy range. The results are presented as chart diagrams in Figure 29a and b, respectively. In addition, multiple valence orbitals (their spatial distributions and energies) are depicted in the Figure of appendix 8.8 that have considerable Co contributions, including the unoccupied MOs with significant contributions to the XA transitions. Other occupied orbitals will be addressed along with the discussion of the RIXS spectra, below. From the ground state DFT calculation one can thus infer that MO 170 is the lowest unoccupied molecular orbital (LUMO), and the main contributions to the XA spectrum of Figure 27 (bottom) are the 2p to LUMO and LUMO +3 (MO 173) transitions. Together with the Figure 29b one finds that these unoccupied orbitals are largely of d_{z^2} and $d_{x^2-y^2}$ character, resulting from the 3d energy splitting in an approximate square-pyramidal (C_{4v}) ligand-field symmetry. Having nodes between Co and its nearest neighbors, these orbitals are essentially anti-bonding. The small XA peak at higher photon energy, near 785.5 eV (Figure 27, bottom), is identified as the 2p – LUMO +1 (MO 171) and 2p – LUMO +2 (MO 172) transitions. Both orbitals have mainly N character, and less of Co contributions

(d_{xz} and d_{yz}), indicating that the respective transitions are metal-to-ligand charge transfer (MLCT) in nature. Notice that for the molecular ground-state LUMO +1 and LUMO +2 energies are in between the LUMO and LUMO +3 energies, and yet higher photon energy is required (see Figure 27, bottom) for their population by a Co 2p electron. This suggests an alteration of orbital energies due to the highly perturbed nature of core-hole excited state. Considering the stronger N character of the LUMO +1 and LUMO +2, we argue that populating these orbitals by a Co core-level electron may require additional energy relative to LUMO +3 that has mainly Co character. This leads to the observed change of the energetic ordering in the excited state.

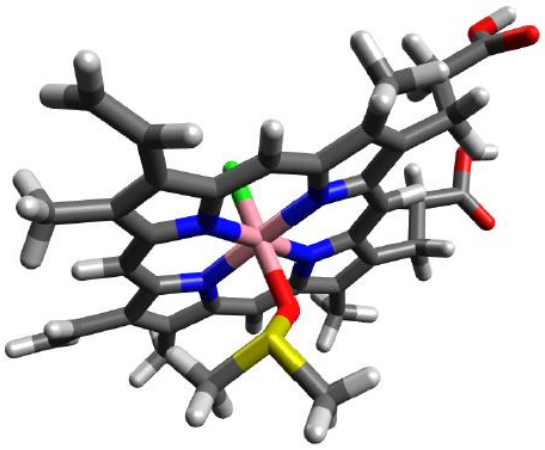

Figure 28. Molecular geometry of Co(III) protoporphyrin IX with DMSO oxygen in the cobalt's sixth-coordination site (S=0).

It is instructive to compare the favorable low-spin case of CoPPIX-Cl in the 5-coordinated geometry with the findings for hemin (previous chapter). Dissolved in the same DMSO solvent, the Fe^{3+} ($3d^5$) ion assumes a high-spin state in the 5-coordinated geometry but it has a tendency to acquire low-spin configuration in the 6-coordinated geometry [179]. Apparently, the analogous situation does not apply for Co^{3+} in CoPPIX-Cl that adopts low-spin state and 5-coordination structure as it was discussed. This raises the question whether Co^{3+} can acquire a sixth ligand, say, from the solvent since it is already in the low-spin state. However, adding a sixth ligand is unlikely to change the spin state. In order to complete the spin-coordination argument, the 6-coordination configuration was explored, too. For this following XA spectrum has been computed: the spectrum of CoPPIX-Cl in a structure where the cobalt center binds to an additional oxygen atom, the oxygen site of the DMSO solvent. The resulting XA spectrum is depicted in the figure of appendix 8.9, and the corresponding structure is shown in Figure 28 (S = 0). The spectrum

is indeed very similar to the one calculated for the respective 5-coordination geometry, and both are in good agreement with our experimental spectrum; all three spectra are presented in appendix 8.9. Very likely both 5-and 6-coordinated geometries co-exist in solution but an experimental quantification of the relative amounts is not possible at the present moment.

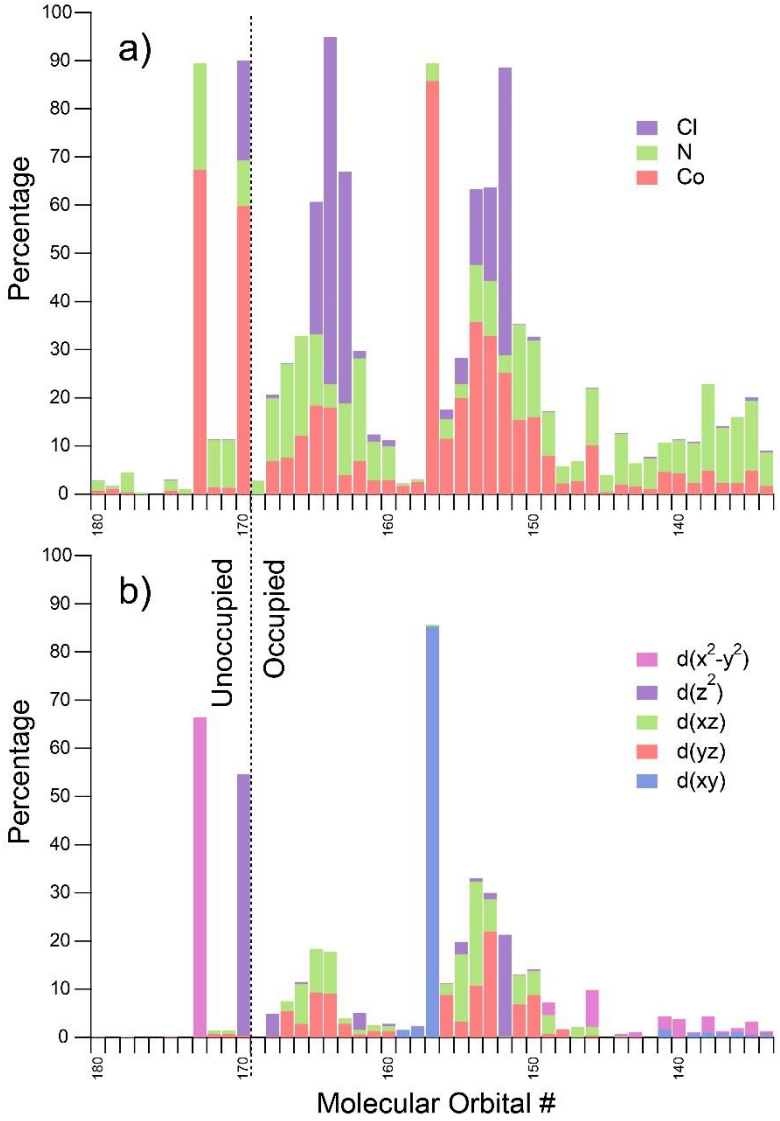

Figure 29. The molecular orbital character obtained from single-point DFT calculations for CoPPIX-Cl. (a) Relative contributions of Co and its nearest neighbors. (b) Contributions from the different Co d-orbitals, obtained from restricted closed shell single point DFT calculation, using Löwdin population analysis.

Regarding experiment, so far only the partial (3d-2p)-yield X-ray absorption spectrum was discussed, which is obtained by integration of many individual RIXS spectra, and these are in fact the actual spectra measured in the experiment. More importantly, the RIXS spectra contain information (which is lost in the XA spectrum due to the

integration) on the states involved in the electronic de-excitation process, and this includes the occupied valence orbitals. As was pointed out earlier in the previous chapter, the computation of L edge RIXS spectra with ORCA is not yet implemented in the ORCA package, and one has to discuss findings rather qualitatively, yet revealing significant new electronic-structure details. For the analysis some few explicit RIXS spectra (mapping aforementioned 3d-2p transitions) will be considered, which were each acquired for much longer time, approximately factor 24, than the individual RIXS spectra, measured at an excitation step width of 0.1 eV, giving rise to the XA spectrum of Figure 26, in order to yield spectra with reasonably good signal-to-noise. It were chosen the RIXS spectra measured at 781.3 eV and 795.7 eV excitation photon energies, corresponding to peak maxima in the respective Co L_3 and L_2 edge XA spectra (see Figure 26, top), and in addition it were also selected some spectra measured at the respective absorption onset (pre-edge), and at a photon energy approximately 1.5 eV above the Co $2p_{1/2,\ 3/2}$-3d resonance. Results are presented in Figure 30; energies are shown as emitted photon energy rather than energy losses, and intensities are scaled to yield the same peak heights at maximum photon emission. In the following discussion we largely focus on the L_3 edge, i.e., on the three bottom spectra of Figure 30.

For all excitation photon energies the RIXS spectra are seen to be almost identical within the approximately 770-778 eV energy range. This emission range, pink-shaded in Figure 30, is well below the onset (pre-edge, feature (a) in Figure 26) of the experimental XA spectrum, and is thus attributed to transitions from doubly occupied molecular orbitals (DOMOs) into Co $2p_{3/2}$. The insensitivity to excitation energy is a clear implication of a weak 3d-3d electron correlation. To support the spectral assignment one has to consider the inset of Figure 30 which is a schematic representation of the experimental excitation (2p-3d) and emission (3d-2p) energies, as well as of the calculated Co orbital energies. The depicted excitation energies (represented by green arrows in the inset) refer to the lowest-energy X-ray absorption ((a) from Figure 26), which is somewhat below the $2p_{3/2}$ - $3d_{z^2}$ (LUMO) transition, and maximum absorption (b) corresponds to the $2p_{3/2}$ - $3d_{x^2-y^2}$ (LUMO +3) transition.

The approximately twice as large intensity for the $2p_{3/2}$ - $3d_{x^2-y^2}$ transition as compared to the $2p_{3/2}$ - $3d_{z^2}$ transition, observed in Figure 27, reflects the difference in the respective density of states of the 2p core-level. Feature (c) corresponds to a post-edge absorption due to the MLCT transitions (LUMO +1, LUMO +2) that require higher

energies than $3d_{x^2-y^2}$, as discussed above. For excitations (a) and (b) the corresponding elastic-scattering peaks are clearly visible in the spectra, and indicated by small arrows. With reference to the energy scheme in Figure 30 (inset) it is possible to determine the local HOMO-LUMO gap from experiment.

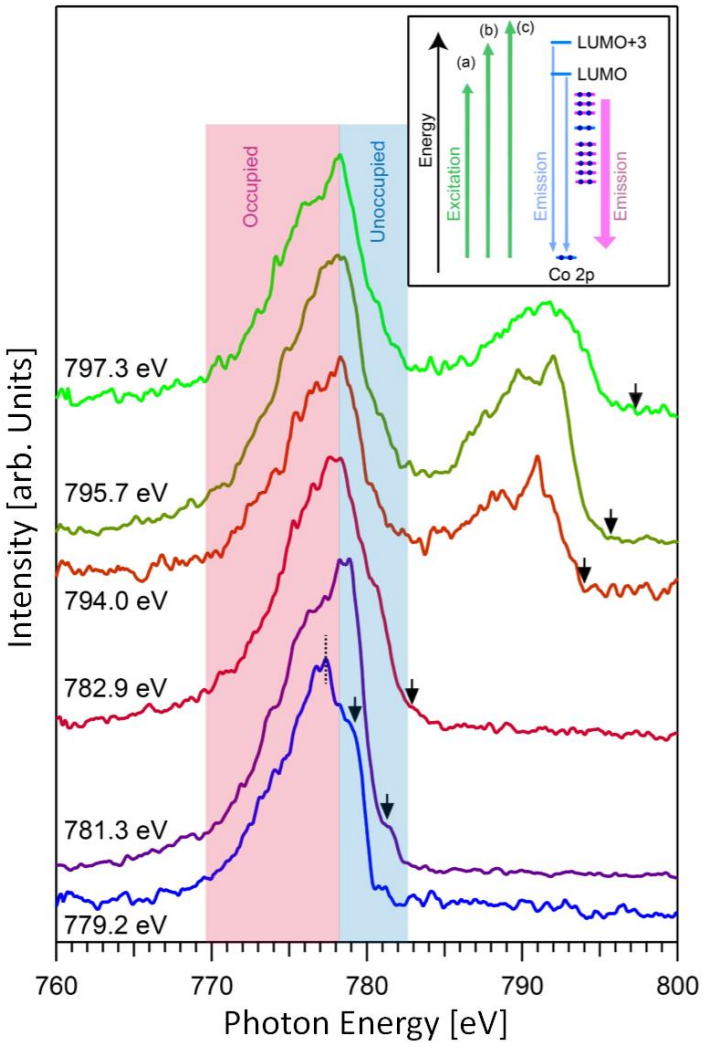

Figure 30. Co L edge RIXS spectra from 50 mM CoPPIX-Cl in solution, measured at selected excitation energies; see text for details. The pink shaded area indicates the doubly occupied molecular orbitals (DOMOs), and the blue-shaded area highlights the unoccupied orbitals. Black small arrows indicate the energies of the elastic peak. The inset is a schematic representation of the observed X-ray excitation and de-excitation transitions along with the relevant orbitals.

The focus is switched now to the RIXS spectrum at the excitation energy 779.2 eV (a), Figure 30, bottom. At this energy a Co $2p_{3/2}$ electron is excited into the LUMO, and the observed (elastic) peak, again shown by small black arrow, thus corresponds to the LUMO-$2p_{3/2}$ electron refill (blue arrow in inset figure). Emission at lower energies than the elastic peak is due to HOMO-$2p_{3/2}$ (pink arrow) and other lower-lying DOMO-$2p_{3/2}$

transitions. The approximately 1.8 eV energy difference between the elastic peak and the onset of the latter transitions (marked by a vertical dashed line) is thus the HOMO-LUMO gap at the Co site. This experimental value is not in a good agreement with the 2.6 eV difference between MO 170 (LUMO) and MO 168 (HOMO -1) in appendix 8.8. Note however that MO 169, which is the actual molecular HOMO, has no metal contribution, and is thus not probed in the present experiment. This energy mismatch mirrors the rather limited value of ground-state DFT calculation for the interpretation of core-hole excitation spectra. As one tunes the excitation photon energy to the maximum L_3 edge absorption, at 781.3 eV (b), one can observe in addition to the elastic peak, which is LUMO +3-$2p_{3/2}$, emission due to the LUMO-$2p_{3/2}$ transition. Since the LUMO is not directly populated by absorption of a 781.3 eV photon, its population is most likely by a shake-up process, involving promotion of an electron from occupied valence states. Shake-up processes occur also for all higher excitation energies, particularly at the L_2 edge, in which case LUMO +3, LUMO -$2p_{3/2}$ transitions are still being observed (giving rise to the signal in the blue-shaded energy region in Figure 30). Here the electron promotion from occupied valence states to LUMO (shake up) is initiated by ionization of the Co $2p_{3/2}$ level. Alternatively, at the $2p_{1/2}$ - LUMO resonance, Coster-Kronig Auger decay may also take place, comprising the refill of the Co $2p_{1/2}$ core hole by a $2p_{3/2}$ electron. This creates a Co $2p_{3/2}$ core hole, and the released energy is used to emit an (Auger) electron from an occupied Co 3d level. The Co $2p_{3/2}$ core hole is subsequently filled by Co valence electrons from DOMOs or LUMO/LUMO +3, resulting in the signal detected in the pink and blue shaded areas, respectively. Note that the direct $2p_{3/2}$-level ionization (at the L_2 edge excitation energy) provides another route for emission in this energy range. The high-energy transitions for L_2 edge relaxation are, however, DOMOs and LUMO/LUMO +3 - $2p_{1/2}$, which lead to the emission intensity in the 785-795 eV range.

4.2 Intermolecular Interactions in FePPIX-Cl Dimer

Porphyrin molecules are often in a solution environment, in which self-association can lead to different types of non-monomeric species. The differences in solvation and solute-solute interactions will consequently affect the functionality of metalloporphyrins, requiring studies of speciation in solution to further our understanding of their

functionality. For example, iron protoporphyrin IX chloride forms monomer species when dissolved in most of the organic solvents, while dimer structures are present in aqueous solution [178,180–182]. It is known that the electronic structure of hemin, especially the local electronic structure at the Fe center, which often serves as the major functional site, is altered due to dimerization. Hemin oligomer species in various solvents have therefore been investigated previously by UV-Vis spectroscopy and X-ray absorption/emission spectroscopy (XAS/ XES) at the Fe L edge, although the nature of the probed electronic transitions implied that the hemin intermolecular bonding interactions were probed rather indirectly. UV-Vis measures overlapping valence excitations of all components in the hemin solution, without differentiation between contributions from solute, solvent or solute-solvent interactions. The lack of exclusive probing of the π-π interactions expected for hemin dimerization left some ambiguity in the interpretation of the UV-Vis data [182]. XAS/ XES measurements at the Fe L edge, on the other hand, represent a local probe sensitive to the electronic structure changes at the Fe sites induced by hemin dimerization [180]. However, the information obtained for the dimerization is still fairly indirect, since hemin dimerization is primarily driven by π-π stacking of porphyrin rings, without intermolecular bonding by the Fe center. The characteristic L edge features at the Fe sites do of course depend on their interaction with the N moieties of the porphyrin ring, but the Fe center in hemin is also coordinated by a chloride ligand. Moreover, there is a sixth vacant coordination site perpendicular to the porphyrin plane, available for possible coordination by molecules from the solvent. Even though contributions of Fe-solvent interaction have been determined to be insignificant [180], they cannot be completely excluded. It is therefore difficult to unravel the different types of interactions at the Fe site for obtaining unambiguous information about the π-π interactions underlying dimerization.

Locally probing the N valence orbitals is expected to be a more explicit way of probing hemin dimerization, or the extent of hemin intermolecular interactions in general. The N moieties are part of the porphyrin ring and thus part of the valence system directly involved in the π-π stacking. Each N atom embedded in the porphyrin ring is fully coordinated with the metal center and C atoms of the porphyrin and consequently there is much less scope for strong interaction with solvent molecules. We have therefore targeted the local electronic structure at the N moieties through X-ray absorption/ emission spectroscopy (XAS/XES), to obtain electronic structure information about the

unoccupied and occupied valence states of hemin in solution [50,183,184]. It will be shown that solvent-dependent XA/ XE spectral differences at the N K edge are observable, and certain XA features are identified as spectral characteristics associated with the extent of hemin intermolecular bonding. Because the carboxylate groups are not conjugated with the π system of the porphyrin ring their influence on the N K edge is expected to be minor, in contrast to the recently presented N K edge spectra of para-amino benzoic acid in solution, where the amine nitrogen felt the direct influence of the carboxylate group as both were part of the delocalized π system of the aromatic ring [185].

In this chapter direct experimental observations are presented, showing the local energy gap of the Fe center of hemin dimer in aqueous solution. The gap is opened, induced by hemin dimerization through π-π stacking of the outer porphyrin ligands. The sections 4.2.1 and 4.2.2 can be directly compared to the previous section 4.1.1 where the hemin was investigated as monomer in dimethyl sulfoxide solution. So far the possible interaction of the solute hemin with solvent molecules was proven to be negligible on the electronic structure of porphyrin based on UV-Vis measurements and the previously presented X-ray study [178,181,182]. XAS/ XES measurements at the Fe L edge represent a local probe sensitive to the electronic structure changes at the Fe sites induced by hemin dimerization and are dealt with in chapter 4.2.1. The N moieties are part of the porphyrin ring and thus part of the valence system directly involved in the π-π stacking. In chapter 4.1.1 it will be shown that solvent-dependent XA/ XE spectral differences at the N K edge are observable, and certain XA features are identified as spectral characteristics associated with the extent of hemin intermolecular bonding.

4.2.1 Local Energy Gap Opening at the Iron Site

Ronny Golnak, Jie Xiao, Kaan Atak, Munirah Khan, Edlira Suljoti, Emad F. Aziz. **Local Energy Gap Opening Induced by Hemin Dimerization in Aqueous Solution.** *J. Phys. Chem. B (2015),* DOI:10.1021/jp509966q

Previous studies have already demonstrated that the hemin dimer structure is two hemin molecules stacking on each other with a certain lateral shift; that is, one Fe center is not directly top of the other Fe center, as shown in Figure 31 [181,182]. X-ray absorption and emission spectroscopy (XAS/XES), with the excitation photon energy tuned to the Fe $L_{2,3}$ edge, were employed here to explore the iron 3d electronic structure of the hemin in aqueous solution, in which unoccupied and occupied valence states were measured,

respectively. The photon-in (excitation) photon-out (probing) process makes the measurements bulk sensitive, significantly reducing possible interface complications. Compared with the K edge measurements on transition metal complexes, the Fe 2p to 3d transitions studied here are dipole allowed, yielding more intense and more structured spectra associated with 3d orbitals than for the dipole forbidden K edge transitions [186].

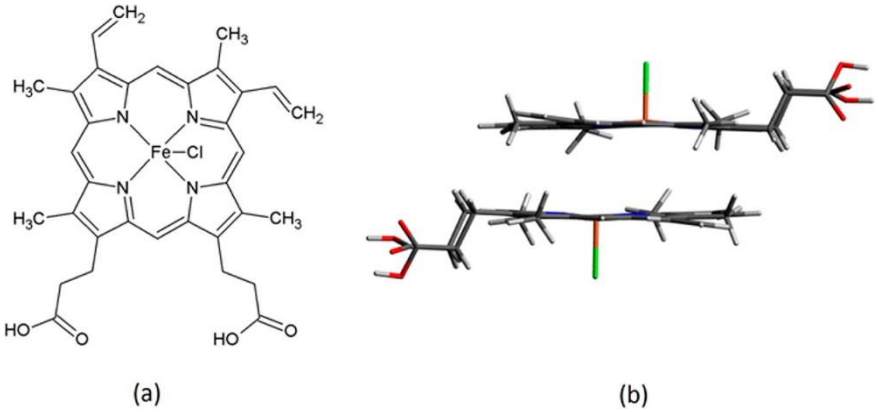

Figure 31. (a) Schematic of hemin chemical structure; (b) geometrical structure of hemin dimer proposed in reference [182].

The obtained PFY-XAS and XES spectra of hemin dimer in aqueous solution are shown in Figure 32. Two major absorption features at 709.0 and 710.3 eV within the Fe L_3 edge are from t_{2g} and e_g orbitals, respectively, owing to the Fe 3d orbital splitting in an approximate octahedral ligand field around the Fe center, as already been demonstrated in the previous chapter 4.1.1 [178]. The XES spectra are plotted in the emitted photon energy scale, instead of photon energy loss scale, because the major XES features, marked by vertical green dashed lines, barely shift as the excitation energy varies. It suggests that the Fe 3d electrons in a hemin dimer structure have little correlation, similar to the situation in a hemin monomer in which absolutely no energy shift was observed in its XES spectra. The XES features of the hemin dimer in Figure 32, however, still have small energy shifts when the excitation energy reaches major absorption edges, as indicated by the shifts of the vertical green lines at both L_3 and L_2 edges; but the magnitudes of the shifts are much smaller than the variations of the corresponding excitation energies, indicating that only very weak d-d electron correlation exists in the Fe 3d electron system of the hemin dimer where the occupied 3d orbitals are only slightly disturbed (excited) by the excited Fe 2p electron.

Besides the small energy shifts observed here, the resonant XES spectra at the Fe L_3 edge in Figure 32 (labeled 710.3 eV and below) have more resolved features than that of the

hemin monomer in the same figure. The absence of the well-resolved XES features generally suggests highly delocalized electrons that overlap strongly with the ligand orbitals, so that the local density of states (LDOS) at the Fe sites is enhanced by valence orbital mixing, leading to more valence states involved in the electronic transitions in the XES process, which could smear out the XES features. Compared with the hemin monomer, the hemin dimer structure exhibits more localized, and thus more correlated character of the Fe 3d electron system, even though the localization and correlation of the Fe 3d electrons is still weak in general. When the excitation energy moves beyond the major absorption peak at the L_3 edge and into the Fe L_2 edge (711.8 eV and higher), the photon emissions at the L_3 edge share the exact energies (marked by a straight green dashed line), exhibiting typical off-resonant emission features, as shown in Figure 32.

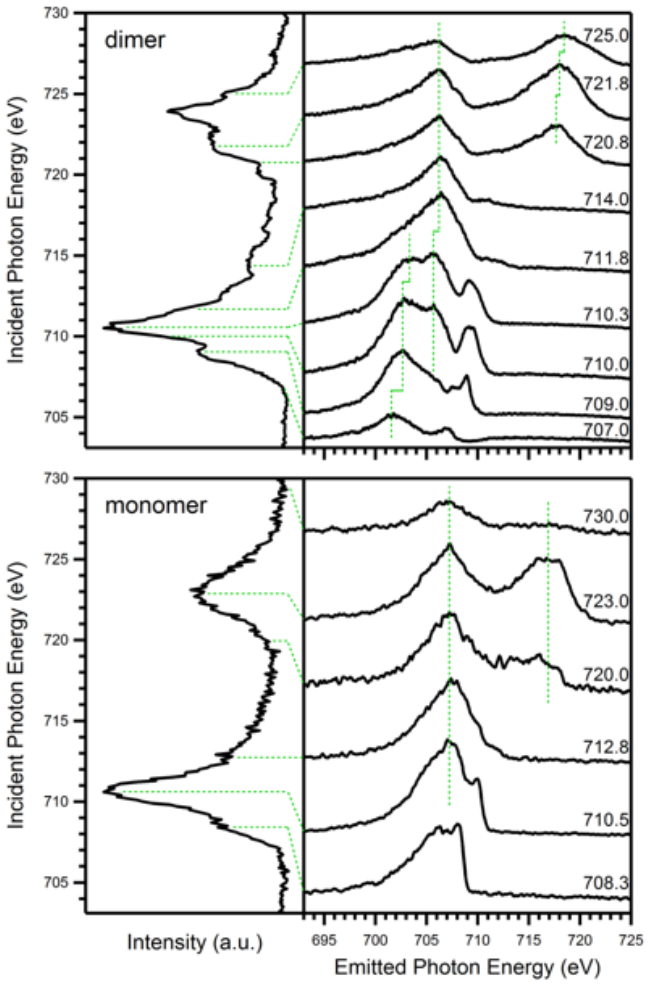

Figure 32. XAS/ XES spectra of hemin dimer (upper) and monomer (lower). The excitation energies used for XES measurements are labeled on the right side of the figure, and also indicated by horizontal green dashed lines pointing to the corresponding absorption features in the left panel. The vertical green dashed lines pointing to the corresponding absorption features in the left panel. The vertical green dashed lines in the right panel mark the major XES features at the Fe L_3 and L_2 edges.

Localization of the valence orbitals usually leads to large energy gaps, as is the case for general insulator materials. The gap opening is indeed observed for the hemin dimer in which the Fe 3d orbitals are more localized as discussed above, when compared with the hemin monomer. The off-resonant emission spectra which represent the occupied valence orbitals, combined with the PFY-XAS that probes the unoccupied valence states, of the hemin dimer and monomer are presented in Figure 33 for comparison. Figure 33 is thus a complementary map of the occupied and unoccupied valence states around the Fermi level for the hemin dimer and monomer. Note that the orbital localization discussed for Figure 32 is inferred from the XES spectra which involve the occupied orbitals only. The off-resonant XES spectrum of the hemin dimer (Figure 33 a) is clearly shifted about 1.3 eV to lower energies with respect to that of the hemin monomer (Figure 33 b), while the PFY spectrum shares the same energies, as indicated by a vertical green dashed line inFigure 33. The extent of the orbital localization is generally greater for low-lying energy levels, but lesser for valence states close to the vacuum level. Above the vacuum level, the electrons are no longer bound to any specific atom and become completely delocalized (free electron). This trend of the orbital localization at different energy levels is well represented in Figure 33. The unoccupied orbitals of the hemin dimer and monomer share identical energies because they are already quite delocalized due to their energy levels being above the Fermi level (close to the vacuum level), while the occupied orbitals of the two hemin species exhibit an energy offset of 1.3 eV due to their different extents of localizations as discussed above. The local energy gap for the hemin dimer is thus opened by shifting the occupied orbitals away from the Fermi level. The localization of the occupied orbitals also results in a narrower peak width of the off-resonant XES for the hemin dimer, compared to that of the hemin monomer, as shown in Figure 33. The reduction of the peak width for the dimer structure shares the same reasoning as for interpreting the better-resolved resonant XES features in Figure 32, that is, the less LDOS caused by the orbital localization. On the other hand, hemin monomer has a greater extent of the delocalization of the valence (occupied) 3d electrons than that of hemin dimer, resulting in broader emission features, as observed in the XES spectrum of Figure 33b. As pointed out in the Introduction that any significant differences observed in the Fe L edge PFY-XAS and/or XES spectra of the hemin dimer and monomer must originate from the hemin dimerization (or its induced effect) through the π-π stacking, the orbital localization that directly leads to the observed spectral differences discussed above is the major induced effect. The resultant gap opening for the hemin dimer suggests that the

total energy of the dimer structure is lower than the combination of two isolated monomers since the valence occupied states of the dimer shift to lower binding energies, as shown in Figure 33, indicating that the dimer is the favored structure in aqueous solution. If a checkerboard structure self-assembles on a substrate with dimer structure as the building block, the overall energy of the whole 2D porphyrin network is then expected to be significantly lowered, compared to isolated molecules or other 2D structure the adsorbed porphyrins might adopt. This argument of the reduced total energy provides an alternative explanation at the electronic level for the abrupt enhancement of the metalation rate of 2HTPP with Cu(111) substrate that was investigated by Röckert *et al.* [187] in which the steric reason that the mobility of free Cu atoms is increased due to the elevation of every other porphyrin molecule in the network was offered. The detailed mechanism connecting the hemin dimerization and the orbital localization is still under investigation by theoretical simulations. Owing to the high sensitivity of the valence orbital to the surrounding ligand field, such observed electronic changes in the local valence structure are not totally unexpected since the porphyrin planar structure may be altered by the π-π stacking of the two adjacent porphyrin molecules in solution, even though the Fe center is not involved in the dimerization process directly.

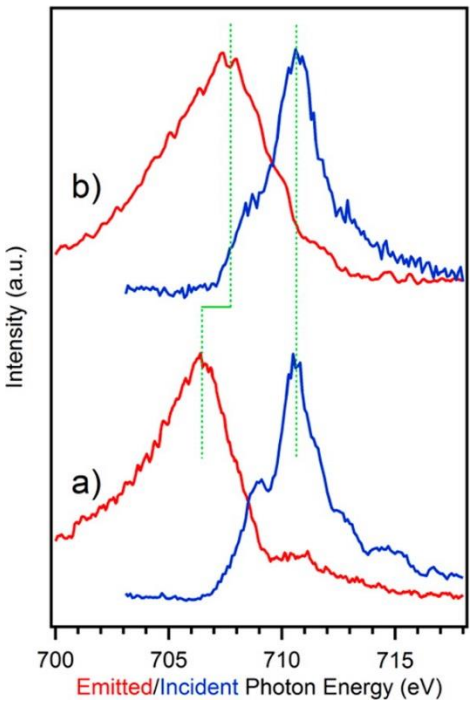

Figure 33. Off-resonant XES spectra (red traces) at the excitation energies of 714.0 and 712.8 eV for the hemin dimer (a) and monomer (b), respectively, combined with their respective PFY spectra (blue traces). Vertical green dashed lines mark the major absorption and emission features, as well as their energy shift. The spectra of the hemin monomer (b) were introduced already in chapter 4.1.1.

4.2.2 Characteristic XA-Feature Shifting of Nitrogen

Ronny Golnak, Jie Xiao, Kaan Atak, Joanna S. Stevens, Adrian Gainar, Sven L. M. Schröder, Emad F. Aziz. **Intermolecular Bonding of Hemin in Solution and in Solid State Probed by N K-edge X-ray Spectroscopies.** *Phys. Chem. Chem. Phys. (2015),* DOI:10.1039/C5CP04529K

Locally probing the N valence orbitals is expected to be an explicit way of probing hemin dimerization. In this chapter it will be shown that solvent-dependent XA/ XE spectral differences at the N K-edge are observable when hemin dissolved in DMSO and 0.5 M NaOH is compared. Certain XA features are identified as spectral characteristics associated with the extent of hemin intermolecular bonding.

DMSO and 0.5 M NaOH aqueous solution were chosen as solvents to dissolve hemin powder as in previous studies. These solutions contain hemin monomer and dimer species, respectively [178,180]. The high pH value (from NaOH) of the aqueous solution increases hemin solubility in water, but adds potential additional complexity due to formation of the carboxylate anionic form in basic solution, as shown in Figure 34c. However, because the carboxylate groups are not conjugated with the π system of the porphyrin ring their influence on the N K-edge is expected to be minor, in contrast to the recently presented N K-edge spectra of *para*-aminobenzoic acid in solution, where the amine N felt the direct influence of the carboxylate group as both were part of the delocalized π system of the aromatic ring [185].

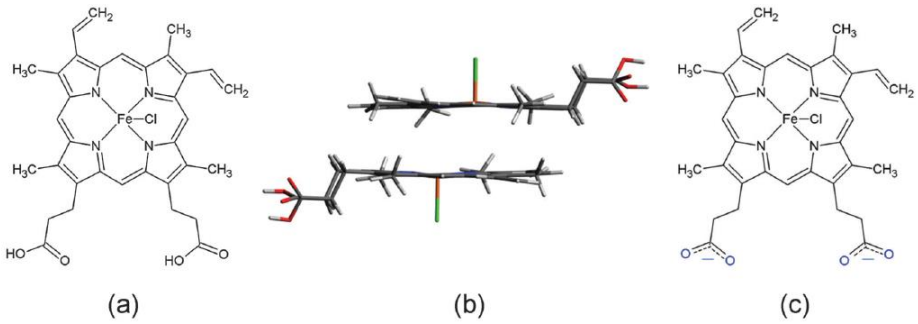

Figure 34. (a) Schematic of hemin chemical structure with neutral carboxyl groups (COOH), (b) geometrical arrangement of hemin dimer, and (c) schematic of hemin chemical structure with anionic carboxylate groups (COO^-).

The obtained PFY-XA and XE spectra of hemin in DMSO (monomer) and in 0.5 M NaOH aqueous solution (dimer) are shown in Figure 35 as blue and red traces, respectively, along with the difference plot (black trace in the left panel) obtained from the subtraction of the monomer XA spectrum (blue) from that of the dimer (red). The XA spectra of the two hemin oligomer species are very similar but on closer inspection three

regions with significant spectral differences can be identified, indicated by the three color-highlighted areas of the difference plot. The intense absorption feature at 398.5 eV, which represents the lowest unoccupied molecular orbital (LUMO) at the N sites, is associated with the porphyrin nitrogen in a N-Fe environment [188,189]. Such a low-lying energy feature is, therefore, completely absent in small metal-free N-containing molecules [185,190,191]. The metal-free porphyrin (2HTPP) usually has the first N absorption feature located more than 1 eV below the metal-N peak with much reduced intensity, arising from the inequivalence of the N species in the absence of the metal center, leading to iminic =N– and pyrrolic –NH– nitrogen [188,189]. The slight energy shift between the two absorption edges at around 398 eV is made evident by the blue-highlighted area in the difference plot, which actually indicates a broadening, instead of an energy shift, of the first absorption feature for the hemin dimer species since its peak position at 398.5 eV does not exhibit observable shift when compared with that of hemin monomer (the broadening effect is discussed below). Nonetheless, the N-Fe features of the two hemin species are in general very similar, which is in line with the similarity of the LUMO observed in the Fe L edge XA spectra [180] (compare with previous chapter 4.1.1), indicating that the N-Fe bonding is not strongly influenced by the dimerization process, or affected by the different solvents significantly. The absorption features at 400-403 eV (green-highlighted) originate from N π^* orbitals as N is part of the aromatic ring system, while the arising absorption edges at the brown-highlighted area are in the region of the ionization potentials (IPs) [185,190]. The N π^* orbitals and IP thus exhibit distinguishable characteristics for different hemin solutions. The exact origins of these differences will be discussed in detail for Figure 36.

Besides the unoccupied valence orbitals revealed by XAS, slight differences between the occupied valence states at the N sites are also uncovered by the XE spectra of the two hemin solutions (Figure 35). Emitted photon energies, instead of photon energy losses that are often observed in highly localized and correlated electron systems as in d or f orbitals, are shared by the N XE features measured at various excitation energies, marked by vertical dashed green lines in Figure 35. The absence of the loss features indicates little electron correlation in the N 2p orbitals, as expected for generally delocalized orbitals like valence s or p. The XE spectra of hemin in NaOH aqueous solution (red traces) present generally a better resolution (narrower peaks) when compared with the spectra of hemin in DMSO (blue traces). This is in line with the previous observation at the Fe L edge that the Fe XE peaks of hemin dimer species are narrower than those of hemin

monomer, owing to the higher degree of orbital localization induced by hemin dimerization [180] (chapter 4.3.2). Different degrees of orbital delocalization (or localization) in the two hemin oligomer species also lead to the elastic peaks with different intensities. The elastic peak of each red XE spectrum (hemin dimer) in Figure 35 shows higher intensity than the blue trace (hemin monomer) when the excitation energy tuned to the corresponding absorption peaks, indicating higher cross-sections of the N 2p → 1s transition for hemin dimer. It can be argued that the higher degree of orbital localization in hemin dimer preserves a density of states (DOS) with the p character of the N 2p orbital better than in the hemin monomer, resulting in more dipole-allowed 2p → 1s transitions. If the N 2p orbitals mixes more with Fe 3d orbitals, lower transition probability is expected since lower DOS with p character is present at the N sites due to the higher extent of N 2p orbital delocalization in the hemin monomer.

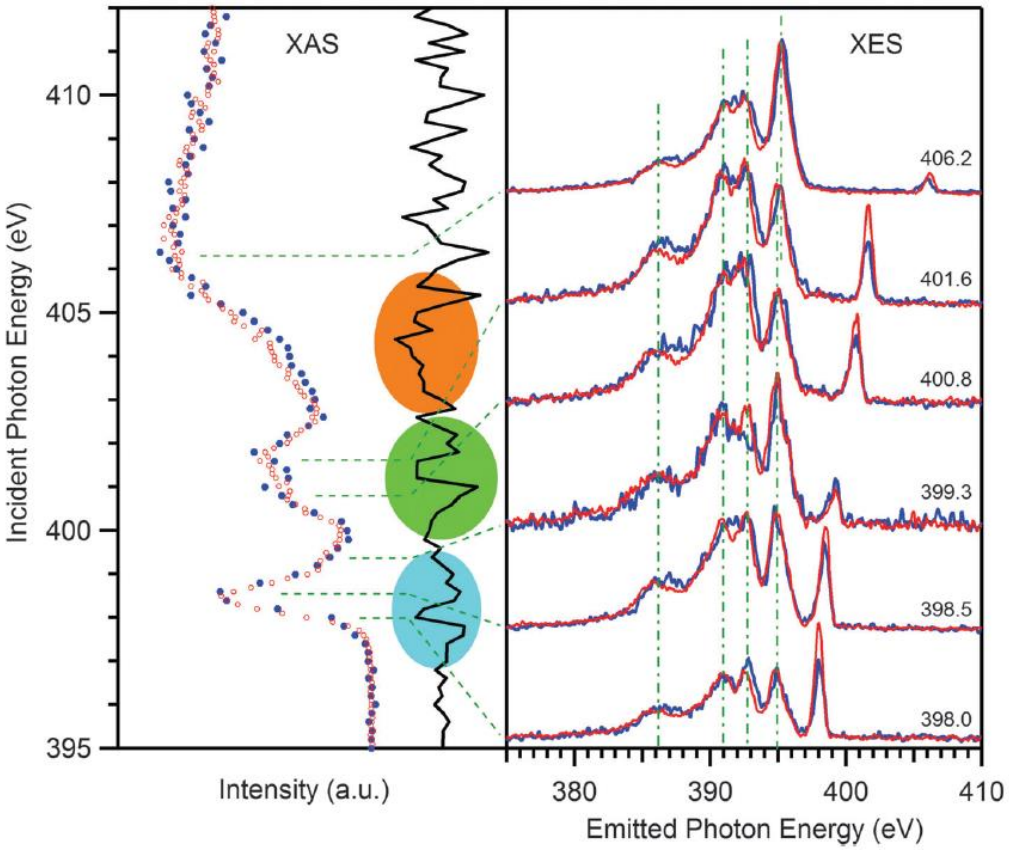

Figure 35. PFY-XA and XE spectra of hemin dissolved in DMSO (blue) and in NaOH aqueous solution (red). The black trace is the difference plot of the two XA spectra, with color-highlighted areas indicating the differences observed in the PFY-XA spectra of the two hemin solutions. The excitation energies used for XES measurements are labeled on the right side of the figure, and also indicated by horizontal green dashed lines pointing to the corresponding PFY features in the left panel. The vertical green dashed lines in the right panel mark the major XE features at the N K edge.

The more intense elastic peak and better resolved emission features in the N XE spectra of hemin in aqueous solution could be regarded as an indicator of hemin dimerization, similar to the observation of the local energy gap opening at the Fe L edge used to indicate the hemin dimerization [180]. However, unlike the local gap opening at the Fe L edge that involves the energy shift of the characteristic spectral feature, these observed spectral differences in the N XE spectra only contain intensity variations. Signal strength often largely depends on extrinsic parameters and thus cannot be used as an intrinsic and reliable indicator for hemin dimerization. The observed differences of the N π^* orbitals and IP (green and brown areas) in the N XA spectra in Figure 35 may, however, intrinsically differentiate between hemin monomer and dimer species. It is instructive to compare these N XA spectra of the small scale intermolecular bonding species (dimer) in Figure 35 with that of a large scale case in solid form, to clearly identify the characteristic spectral evolution under the various extents of hemin aggregation. Such a comparison of the XA spectra is presented in Figure 36, with their respective fitted components (green traces) as well as the summations of the components (red traces). Each individual fitted Gaussian component below IP is marked by vertical dashed lines and labeled as A, B, C, D and E. The IPs are fitted by arctan step functions with their energy positions marked by vertical lines as well.

The most striking difference between the solid state and the solution spectra is the considerable broadening of almost all the spectral features in the solid state spectrum. This is likely due to the extensive orbital overlapping in the solid state [192,193] and was also somewhat evident in the previous study of aminobenzoic acid [185]. Self-absorption distortions of the spectrum from the more dense solid state may also contribute to the observed broadening of features. This solid state broadening makes the component A, originating from the N-Fe interaction as discussed in Figure 35, and component B resolvable in Figure 36a and b after the Gaussian fitting appear to be irresolvable in Figure 36c. The feature B may stem from a multi-electron excitation, e.g. a shake-up satellite to feature A, or reflect an electronic state that originates from solute-solvent interactions since the ground state calculation (vertical bars at the bottom of Figure 37) does not give rise to any molecular orbitals in this energy region. Feature A keeps relatively similar peak widths in Figure 36a and b because the N-Fe interaction is not directly involved in the dimerization process. However, its broadening in Figure 36c suggests that the hemin oligomer species in the solid form may adopt different forms of intermolecular bonding

that may involve the N-Fe interaction to some extent. Components C and D, constituting the green-highlighted difference in Figure 35, exhibit monotonic energy shifts from the monomer (Figure 36a) to the dimer (Figure 36b), and appear to be even lower in the solid (Figure 36c). It seems that these features are associated with the development of hemin-hemin interactions and can therefore be used to characterize the extent of intermolecular bonding. The shifts of the features C and D to lower energies indicate that the measured energy level distances between the N π* orbitals and the N 1s core level are systematically reduced when a larger scale of the hemin oligomer species is realized. The origin of this energy shift could be either an initial state effect in that either the valence N π* orbitals are lowered or the N 1s core level binding energy raised. Alternatively, a final state effect may contribute, perhaps reflecting differences in valence charge relaxation upon core-hole formation, analog to the relaxation shift of CO molecules going from gas phase to solid state observed in photoelectron spectroscopy [194]. However, recent studies of bipyridine acid salts and co-crystals indicated that the effect of final state effects on the relative positions of π* features are negligible, even when comparing bipyridine nitrogen species in very different local chemical environments [195]. Further inspection into the individual components C and D uncovers that the feature C remains roughly constant in peak width from Figure 36a to c, while the feature D becomes broader and relatively more intense upon hemin aggregation. The mechanism of this distinct peak evolution is likely due to the different extents of the orbital involvement in the hemin intermolecular bonding interactions which will be discussed in detail for Figure 37 based on a molecular orbital (MO) picture derived from DFT calculations.

The evolution of feature E is very similar to feature A, both exhibiting solid state broadening. However, the feature E does not have a sole MO origin as for feature A where the N-Fe interaction can be assigned, because it consists of contributions of many MOs. A similar situation also occurs for the broadest fitted Gaussian components with their centers located above the IPs, representing contributions from a number of MOs, as illustrated by the vertical bars at about 404-411 eV at the bottom of Figure 37. Strictly speaking, each spectral feature in Figure 36 comprises multiple MOs, and therefore should not be represented by a single Gaussian function in principle. Nevertheless, the fittings of the components A, B, C and D with a single Gaussian function still hold the physical significance discussed above because the contributed MOs to each component are very few in number and also located closely to each other in energy, as demonstrated

in Figure 37. The characteristic spectral features that can distinguish various hemin oligomer species are therefore the features C and D in Figure 36 exhibiting systematic energy shifts, and consequently associated with the extent of hemin intermolecular interactions.

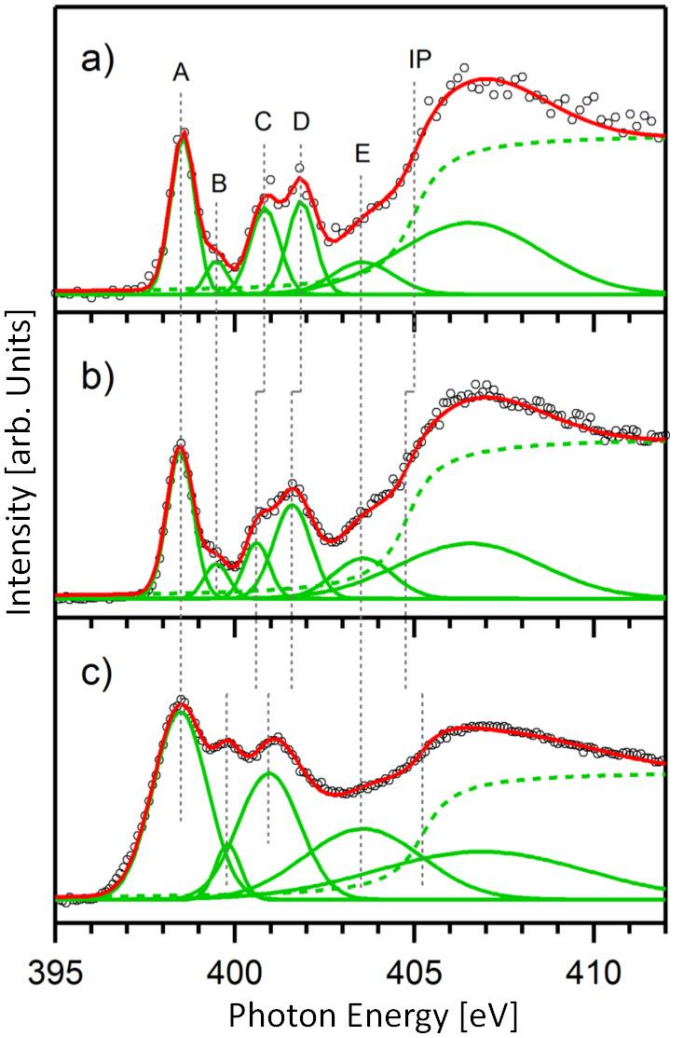

Figure 36. Nitrogen K edge PFY-XA spectra, represented by circles ○, of (a) hemin in DMSO, (b) hemin in NaOH aqueous solution and (c) hemin powder in solid form, with their respective fitted components in green and the summation of these components in red. The ionization potential (IP) is fitted by step functions arctan, represented as green dashed traces, while the other components by Gaussian functions (solid green traces) with labels A, B, C,D and E. The energy positions of the IP and fitted Gaussian components, as well as their relative energy offsets, are marked by grey dashed lines.

The energy shifts of the IPs, however, do not follow the monotonic energy shift when going from dimer to solid, as shown in Figure 36b and c. The IP shift from Figure 36a to b is in line with the energy shift of the features C and D, which seems to suggest they have the same origin - elevation of the N 1s level. However, the core level argument

cannot explain the non-shifting features, such as feature A, and the opposite shifting of the IP in the spectrum of the solid sample. The other mechanism discussed above, i.e. the initial state effect of the valence orbital shifting, has to come to play.

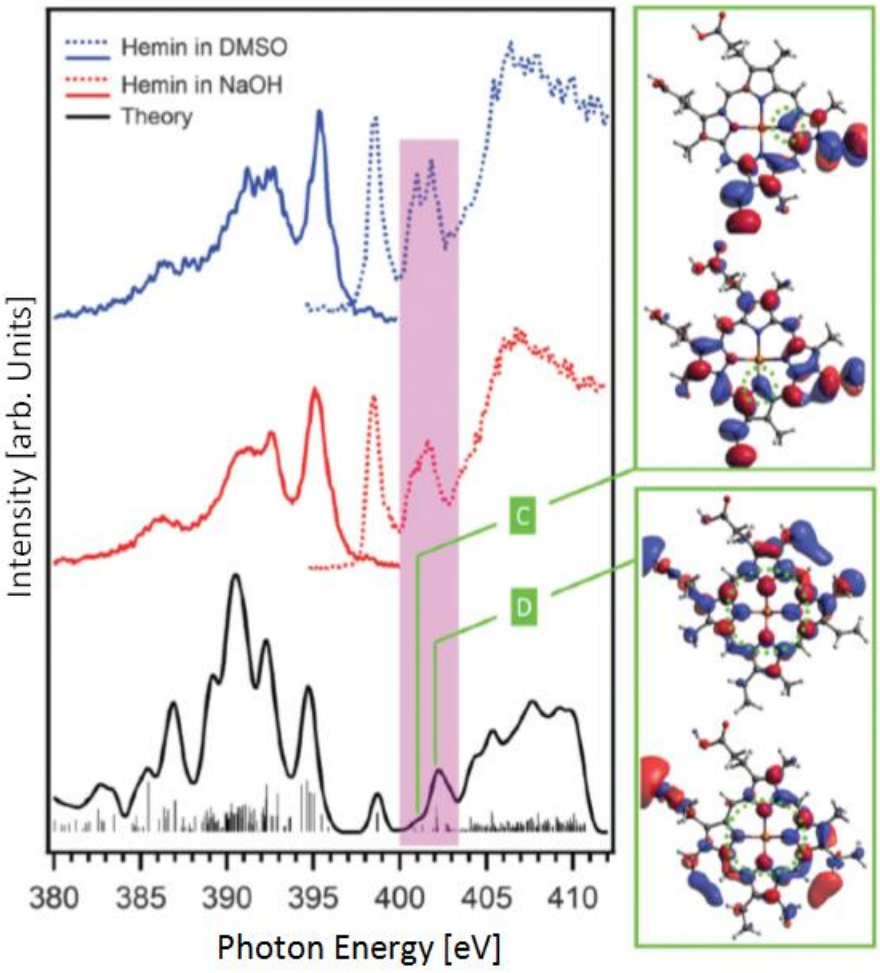

Figure 37. Off-resonant XE spectra (solid blue and red traces) at the excitation energies of 420 eV for the hemin dissolved in DMSO and NaOH aqueous solution, respectively, combined with their respective PFY-XA spectra (dashed blue and red traces). The experimental spectra are identical to the corresponding spectra in Figure 35. The theoretical DFT calculations and individual MOs weighted by N contributions are shown at the bottom as black trace and vertical bars, respectively. The characteristic features C and D identified in Figure 36 are assigned to certain calculated MOs with visualized orbitals presented on the right side of the figure. The orbitals localized at the N sites are highlighted with dotted green circles.

Some DFT calculations were conducted with the ORCA program package [115] to obtain the molecular orbital (MO) information of the hemin molecule in gas phase in the ground state [178]. Molecular geometry optimization was performed using the B3LYP DFT method together with the def2-TZVP(-f) basis set [116–118]. The N contributions to both occupied and unoccupied valence MO are acquired from Löwdin population analysis based on the

DFT calculations [196]. A Gaussian-type broadening of 0.5 eV with the respective weight (according to the N contribution) is applied to each valence MO and then summed up, to simulate the XA/XE spectra obtained at the N K-edge.

With the help of the ground state DFT calculations, the origins of the characteristic features C and D that exhibit distinct spectral evolutions of the component width and intensity in Figure 36 is uncovered at a MO level. The theoretically simulated spectrum at the occupied and unoccupied valence levels, obtained from the summation of individual N contributions with a universal Gaussian broadening, is plotted in Figure 37, along with the combined XA and XE spectra of the hemin monomer (in DMSO) and dimer (in NaOH aqueous solution) for comparison. The N contribution to each calculated MO, shown as vertical bars at the bottom of Figure 37, is acquired from the Löwdin population analysis based on the DFT calculations of the gas phase hemin in the ground state. Even though the experimental spectra are acquired from the core-hole excited final state (XAS) or initial state (XES), the simulated peak positions from the ground state calculation are in good agreement with experiment, allowing for accurate and reliable assignments of the calculated MOs to the experimental peaks. The characteristic features C and D in Figure 36 can therefore be visualized as the MOs presented in Figure 37. As illustrated in Figure 37, the feature C mainly originates from the orbitals localized at a single N atom; while the feature D, on the other hand, is from the orbitals delocalized over all four N atoms, as highlighted by dotted green circles. With development of the hemin intermolecular bonding through π-π stacking of the porphyrin ring, the feature D that involves four N atoms will surely develop a higher extent of the peak width broadening as well as intensity enhancement, owing to the extensive orbital overlapping, when compared with the feature C that has only very localized orbitals involved in the hemin-hemin interaction. The localized nature of the feature C inhibits its orbital overlapping with neighbor orbitals and consequently suppresses the broadening and enhancement of the fitted peak, as demonstrated in Figure 36.

Due to the computational challenges for large-scale hemin oligomer species - dimer and above - the DFT calculations are only performed on a geometry-optimized isolated hemin monomer. The proposed N 1s core level shift arising from the different hemin oligomer species is therefore unable to be probed theoretically. The DFT calculations are carried out on the ground state, so that the final state effect is not possible to investigate. The spectrum of the solid sample is not included in Figure 37 for the comparison with the

theoretical simulation because the strong solid state effect is expected to have significant influences on both initial state shifting and final state relaxation, which shifts certain experimental peaks significantly when compared with those of the isolated molecules, as has been demonstrated in Figure 36 for the features C and D. Therefore, attempted assignments of the calculated MOs performed on the gas phase molecules to the solid state features may not possess high credibility.

4.3 Outer Ligand Effects on Metalloporphyrins in Solution

It is an amazing and interesting question that how exactly the electronic structure, especially the valence levels, of the metal center is altered by outer ligands. In this section the investigations upon ligand effects in metalloporphyrins are presented. Two similar systems were investigated in liquid solution at very low concentration. One system is the manganese octaethylporphyrin chloride (MnOEP-Cl) and manganese teraphenyl-porphyrin chloride (MnTPP-Cl) in dichloromethane, in section 4.3.1. The other system is the iron octaethylporphyrin chloride (FeOEP-Cl) and iron teraphenylporphyrin chloride (FeTPP-Cl) in dichloromethane, in section 4.3.2.

Both systems were characterized by resonant inelastic X-ray scattering (RIXS). While the Mn samples were probed at the Mn and N edge, the Fe samples were only characterized at the Fe edge. In addition the metal-ligand orbital mixing is analyzed with the help of density functional theory/ restricted open-shell configuration interaction singles (DFT/ROCIS) calculations.

4.3.1 Outer Ligand Effect on the Metal Center

Ronny Golnak, Jie Xiao, Marvin Pohl, Christoph Schwanke, Antje Neubauer, Kathrin M. Lange, Kaan Atak, Emad F. Aziz. **Influence of outer ligands on metal-to-ligand charge-transfer in solvated Mn porphyrins.** *Inorg. Chem. (2016),* DOI:10.1021/acs.inorgchem.5b01585

In this work, two similar metalloporphyrins with identical central part but different outer ligands, manganese tetraphenylporphyrin chloride and manganese octaethylporphyrin chloride, were selected as a model system to explore the influence of the porphyrin outer ligands on the electronic structure, including the MLCT, of the central part.

In order to explore the possible effects of the porphyrin outer ligands on the central electronic structure, it is ideal to leave the outer ligands unconstrained so that they can freely exert their influences on the central part. A liquid solution, instead of a solid substrate, is therefore a more suitable environment to allow for the flexibility of the outer ligands as well as for any possible geometric variations of the porphyrin central part induced by the outer ligands. The solvated porphyrins can also mimic realistic conditions in biochemical systems. Dichloromethane (CH_2Cl_2, DCM) is chosen as the solvent in this study since it was adopted as the solvent for similar metalloporphyrin solutions in our previous study and its chemical nature is well-understood [54]. Moreover, the simple and symmetric outer ligands, four phenyl groups of MnTPP-Cl and eight ethyl groups of MnOEP-Cl, can avoid additional complexity that is often present in real biological systems due to complex ligands. The molecular structures of these porphyrines are shown in Figure 38:

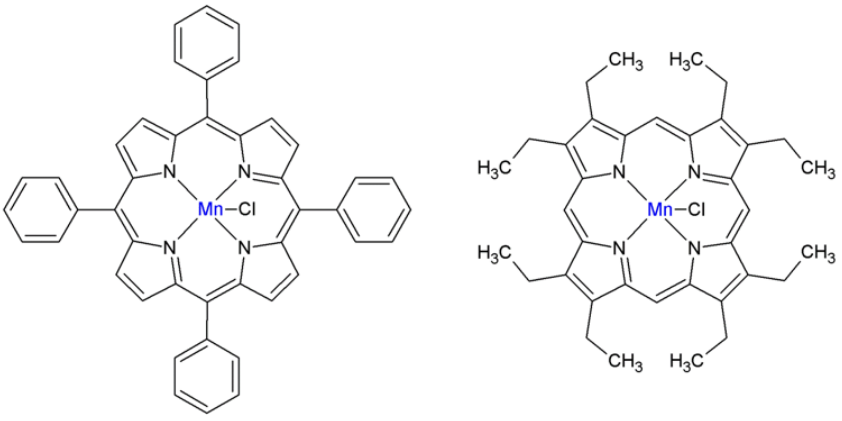

Figure 38. Structural formula of MnTPP-Cl (left) and MnOEP-Cl (right).

The localization character of the MLCT and its mediated chemical bond requires a local probe that is able to selectively investigate the valence electronic structure of specific atoms in liquid solution, which makes resonant inelastic X-ray scattering (RIXS) the most suitable probing tool [197]. The dipole-allowed core-level excitation and subsequent core-hole relaxation in RIXS process leave the probed system in a valence-excited electron-hole-pair state. If a N 1s core-level is resonantly excited, the N 1s core-hole can be filled by an electron originating from orbitals with Mn 3d character when there is a considerable metal-ligand valence orbital mixing. This RIXS process therefore leads to a "metal-to-ligand charge-transfer" (MLCT) with the excited N 1s electron primarily located at the N site, while the hole is mainly localized at the Mn site, forming an electron-hole-pair at the valence level. The intensity of such a charge-transfer transition directly reflects the

strength of the metal-ligand orbital mixing in the covalent bond. This method has been successfully applied to probe the molecular orbital hybridization in adsorbed gas molecules on various metal substrates as well as in solvated small organometallic complexes [50,198].

In this study, both Mn centers and their coordinated N ligands were probed locally by RIXS for both Mn porphyrin solutions. In the following discussion, the labels MnTPP-Cl and MnOEP-Cl are replaced by MnTPP and MnOEP because the Cl^- ligand is detached once the molecules are dissolved in CH_2Cl_2 (explained below in the theoretical discussion). The RIXS maps of the MnTPP and MnOEP at the Mn L-edge show very similar images, exhibiting two energy-loss features located at 3.1 and 4.4 eV away from the elastic peak for both molecules, marked by the tilted dashed lines in Figure 39 (b and c). The different outer ligands in the two Mn porphyrin complexes seem to have little influence on the electronic structure of the Mn metal centers implied by the similarity of the two RIXS maps. According to the literature containing various Mn L-edge RIXS spectra, the energy-loss features up to 6 eV (away from the elastic) are generally categorized as d-d excitations, while the larger energy losses at 8 to 12 eV are often considered to be charge-transfer transitions [199–201]. The two loss features observed in Figure 39 (b and c) are therefore assigned as Mn d-d excitations. The charge-transfer features located in the "white clouds" of the RIXS maps are, however, not as clearly resolved as the d-d transitions due to their general low intensity and broadness.

The PFY-XA spectra of the MnTPP and MnOEP integrated from the fairly similar RIXS images shown in Figure 39 (b and c), however, present slight differences, as indicated in in Figure 39 (a). The overall intensity of the MnOEP spectrum is lower than that of the MnTPP after the intensity normalization to the individual background. Since the MnOEP solution has lower concentration than that of MnTPP, the saturation effect that reduces the intensity of the most intense peak [77,137,139] is expected to be alleviated for the MnOEP solution, resulting in relatively less reduction of the peak intensity at 640.7 eV. A closer inspection of the absorption peak energies reveals that the L_3 features, especially the one at 644.2 eV, and the L_2 features of MnOEP shift to lower and higher energies, respectively, with respect to the corresponding features of MnTPP, resulting in a larger L_3-L_2 ($2p_{3/2}$-$2p_{1/2}$) spin-orbit splitting. The magnitudes of the splitting are 10.26 and 9.92 eV for MnOEP and MnTPP, respectively, measured from the respective spectral gravity centers of each absorption edge, as indicated by the horizontal blue and red lines in Figure

39 (a). Spin-orbit splitting is a relativistic effect induced by charged particles with spin moving in an electric field. A stronger electric field which can be produced by a stronger ligand field or higher oxidized state generally leads to a larger splitting [82,202]. The spin-orbit splitting in 3d valence levels of transition metals usually has the order of magnitude of < 1 eV, but > 10 eV for the 2p core levels due to the different strengths of the nuclear electric filed experienced by the 2p and 3d levels [202].

The different 2p spin-orbit splitting in Figure 39 (a) suggest a stronger electric field present around the Mn center of MnOEP. Such a difference of the electric fields is likely to originate from the ligand field around the Mn centers, instead of oxidation state variation of the Mn ions because different oxidations will also cause the energy offset at the starting absorption edge around 640 eV [202,203], which is not observed in Figure 39 (a). The ligand field difference implies possible variations of the Mn-N bond length/angle in MnOEP as compared to MnTPP, and/or additional ligands from the solvent binding to the MnOEP metal center.

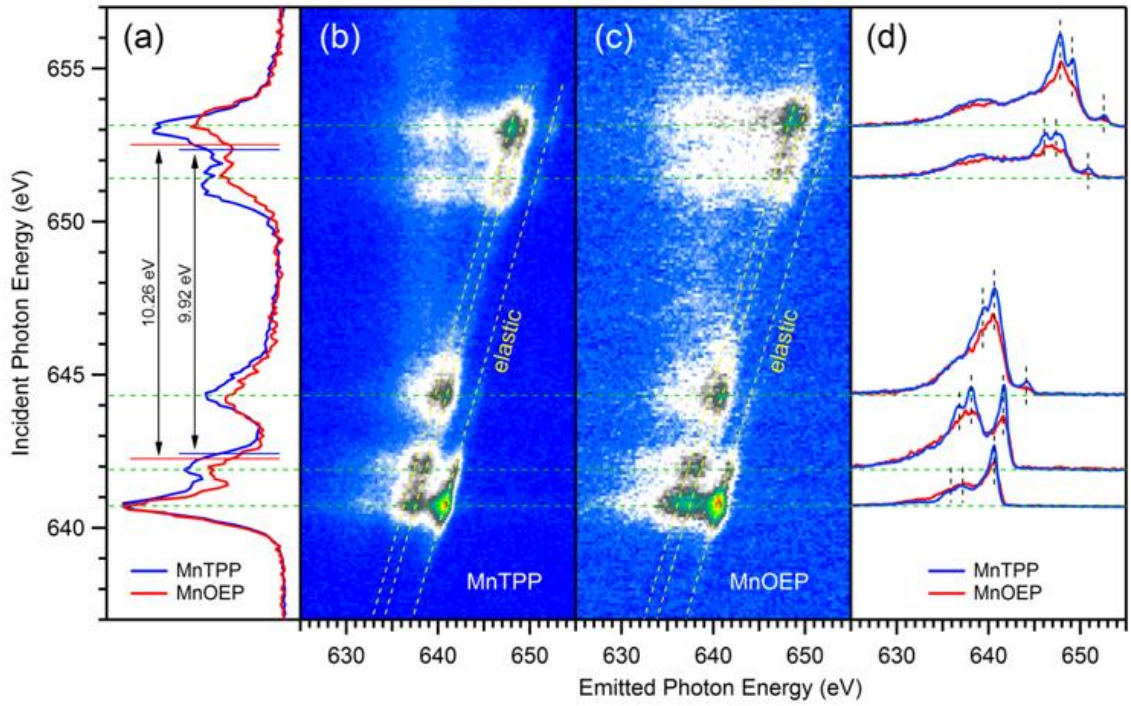

Figure 39. PFY-XA spectra of MnTPP and MnOEP at the Mn L-edge (a) derived from the integrations of their respective 2D RIXS-maps (b) and (c). Selected RIXS spectra measured at the excitation energies of major absorption peaks (marked by horizontal green dashed lines) with extended data acquisition time are presented in (d). The spectral gravity centers of the L_3 and L_2 edges, as well as the respective values of the L_3-L_2 spin-orbit splitting, are indicated in (a). One RIXS elastic and two loss features (d-d transitions) are indicated by tilted dashed lines in (b) and (c), and by short vertical dashed lines in (d).

Different ligand fields are expected to produce different effects on the valence electronic structure, including unoccupied (Figure 39 (a)) and occupied orbitals (Figure 39 (5)). Five selected RIXS spectra (Figure 39 (d)) were measured at the excitation energies of the major absorption features for extended data acquisition durations in order to better resolve the Mn 3d valence excitations. The X-ray energy-loss features of MnOEP, marked by the vertical dashed lines, are in general less resolved than those of MnTPP. The absence of clear energy-loss features generally indicates that the absorption process has little influence on the emission process, suggesting that the Mn 3d electrons are less correlated in MnOEP than in MnTPP, most likely due to the more itinerant character of the Mn 3d orbitals in MnOEP through the higher extent of valence orbital mixing with the ligands. The stronger orbital mixing in MnOEP is also supported by the more intense charge-transfer features which appear as the left shoulders to the d-d excitations (marked by the vertical dashed lines) in Figure 39 (d). The charge-transfer intensities in the MnOEP RIXS spectra are actually higher than those in the MnTPP spectra if the intensities of their d-d excitation peaks are normalized.

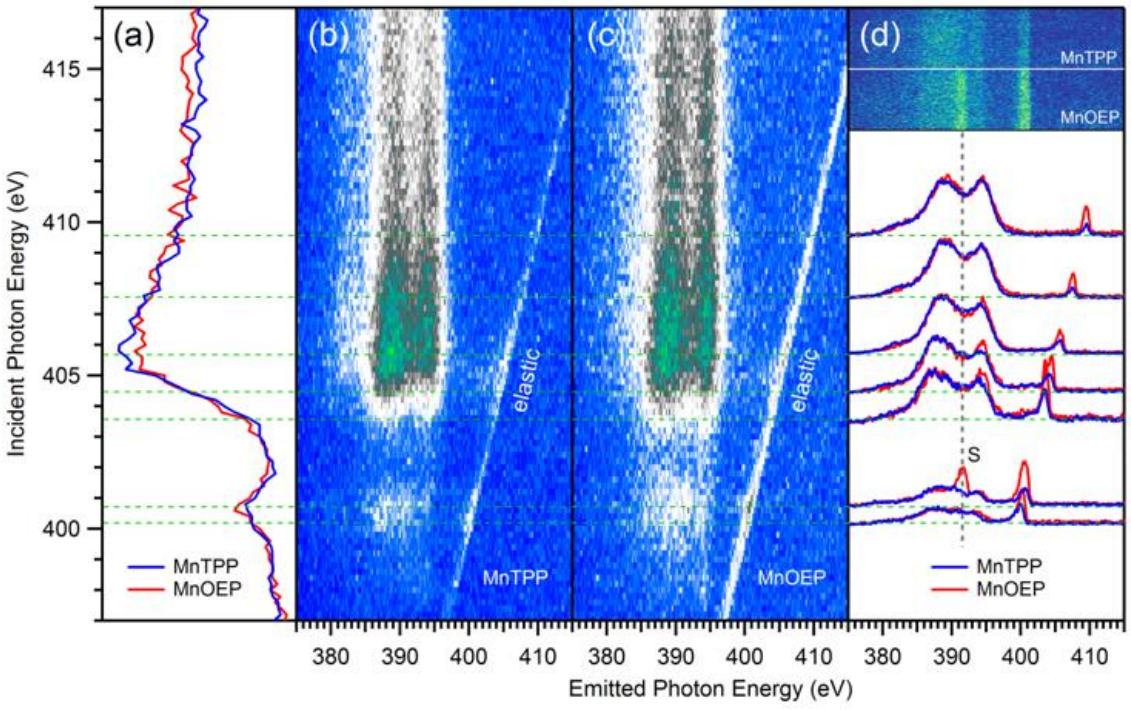

Figure 40. PFY-XA spectra of MnTPP and MnOEP at the N K-edge (a) derived from the integrations of their respective 2D RIXS-maps (b) and (c). Selected RIXS spectra measured at various excitation energies (marked by horizontal green dashed lines) with extended data acquisition time are presented in (d). A distinctive RIXS feature "S" of MnOEP taken at the excitation energy of 400.8 eV is marked by a vertical dashed line in (d), along with the two RIXS camera images of MnTPP and MnOEP taken at the same excitation energy presented at the top.

The N K-edge RIXS spectra provide a complementary picture to the valence structure, as shown in Figure 40. Unlike the Mn 3d excitations that exhibit distinctive energy-loss features (Raman-like behavior), the emission energies of the N fluorescence features do not follow the dispersion of the elastic peak, but rather remain constant as the excitation energy varies (regular fluorescence behavior). This behavior is expected since the N 2p orbital is not as correlated as the Mn 3d, but a quite delocalized electronic system [204,205]. The different delocalization characters between the general p and d orbitals are also reflected in the electronic band widths generated by respective p and d orbital overlapping in periodic structures [82]. The normalized PFY-XA spectra at the N K-edge are fairly similar (Figure 40 (a)). The RIXS spectra in Figure 40 (d), however, exhibit two major differences between the two Mn porphyrins. First, the spectrum of MnOEP has more intense elastic peaks than that of MnTPP, which becomes evident by comparing Figure 40 (b) with Figure 40 (c). Second, there is a distinctive feature (indicated as S) in the spectrum of MnOEP, marked by a vertical dashed line in Figure 40 (d), appearing only at the excitation energy of 400.8 eV – the first N based absorption feature which probably corresponds to the excitation into the lowest unoccupied molecular orbital (LUMO) with considerable N character. The RIXS camera images of the two Mn porphyrins at 400.8 eV are presented as well at the top of Figure 40 (d) for a clear comparison.

The intensity of elastic peaks partially represents the transition cross-section between unoccupied valence orbitals and N 1s orbital, when other measurement conditions are identical, e.g. the angle between the synchrotrons beam polarization and the photon detector. The more intense elastic feature therefore implies a higher unoccupied orbital density at the N sites of MnOEP, as compared to that of MnTPP. Such an enhancement of the valence orbital density may be from the stronger N 2p orbital mixing with the Mn 3d orbital in MnOEP. It is also consistent with the less resolved energy-loss features of MnOEP discussed for Figure 39 (d). The feature S is quite special and unique, as well as very robust and reproducible. It possesses three distinctive properties: 1. It appears at the emission energy where no other N emission features exist, marked by the vertical dashed line in Figure 40 (d). 2. The peak is much narrower than other N features. 3. The feature S is only present in the RIXS spectrum at the excitation energy of the first N absorption peak, i.e. when the lowest N-character acceptor orbital is occupied by the excited N 1s electron. The first two properties of the feature S indicate that the emitter orbital which emits an electron to fill the N 1s core-hole does not possess much of N 2p character. It

instead resembles the character of more localized Mn 3d orbitals. Based on the various indications of the considerable Mn-N orbital mixing in MnOEP discussed above, it is reasonable to argue that the feature S originates from the transition of a valence MO with Mn 3d character to N 1s through a strong Mn-N valence orbital mixing, which is actually a RIXS-induced MLCT process. Such a MLCT occurs only with the presence of a "spectator" electron at the LUMO with significant N character (the third property). The result of the MLCT in MnOEP is the valence excitation with the hole located at the Mn site while the electron is localized at the N site. This electron-hole pair forms a stable excitonic state at the valence level which possesses a definite energy and therefore gives rise to a certain emission energy of the feature S, independent of other N features. The absence of such a feature S in MnTPP strongly indicates the significant influence of the porphyrin outer ligand on the MLCT process.

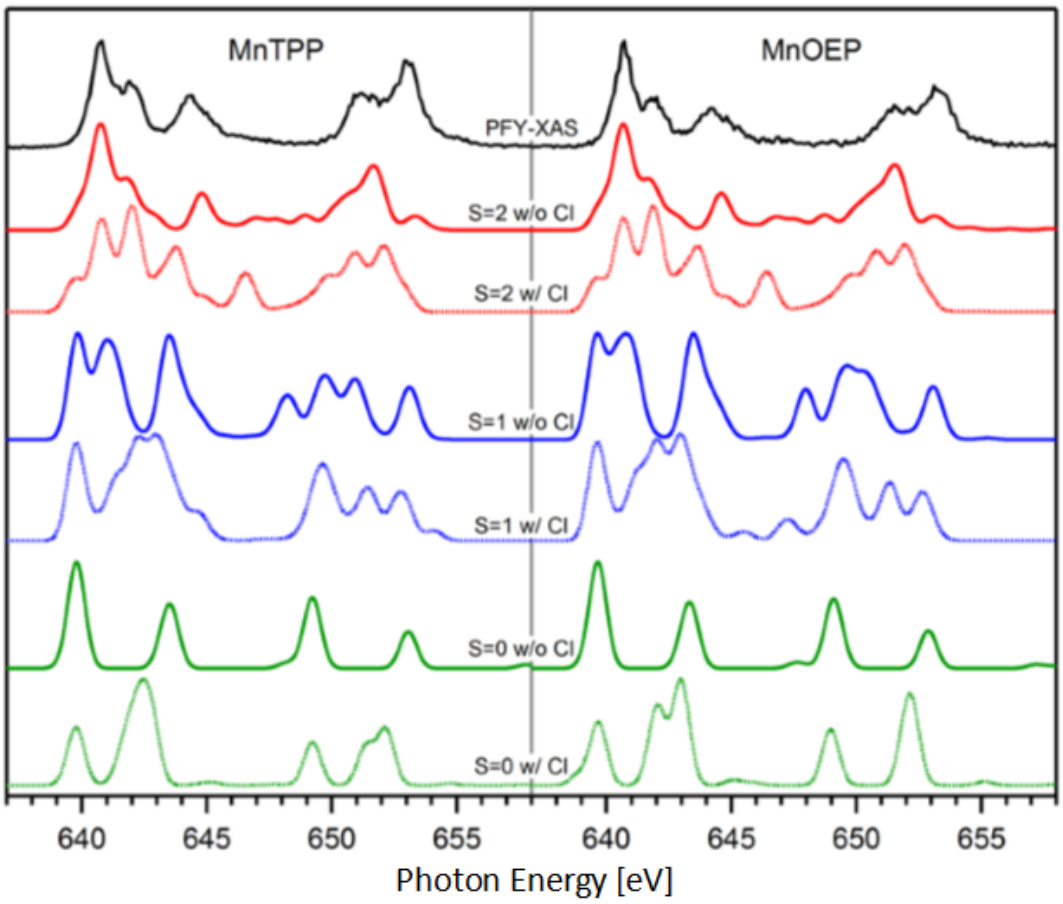

Figure 41. PFY-XA spectra of MnTPP and MnOEP at the Mn L-edge, identical to the experimental spectra in Figure 39 (a), along with simulated XA spectra by DFT/ROCIS calculations for various molecular configurations – total spin S = 0, 1, 2 with and without Cl attached to the Mn center.

It is of importance to compute the electronic structure of the two Mn porphyrins in order to gain insight into the mechanism behind the experimental observations discussed above.

DFT/ROCIS calculations are thus employed to simulate the Mn L-edge XA spectra for various possible molecular geometric and electronic configurations, as shown in Figure 41. The Mn^{3+} (d^4) system can theoretically have spin states S = 0, 1, 2 corresponding to a closed-shell (S = 0) or an open-shell (S = 1, 2) system. The original Cl^- ion in both porphyrin complexes may either remain bound to the Mn^{3+} center or dissociate when dissolved in CH_2Cl_2. Therefore, a total of six different molecular configurations may exist for each solvated Mn porphyrin. All six structures are calculated and presented in Figure 41, along with their respective experimental PFY-XA spectrum shown at the top for comparison. It is apparent that the top red traces (high spin state S = 2, without an attached Cl^- configuration) are the best matching simulated spectra for both solvated Mn porphyrins, and thus reproduced in Figure 42 (b), along with the experimental spectra (Figure 42 (a)) for further analysis. Traces in Figure 42 (c) are the simulations without the spin-orbit coupling (SOC) effect applied, which have a significantly reduced number of transitions, but still largely preserve the spectral characters at the L_3 edge, allowing for identifications of the contributing orbitals [178,196]. Based on the simplified SOC-excluded spectra (Figure 42 (c)), the first absorption features of both Mn porphyrin complexes at around 640.7 eV in Figure 42 (a) can be attributed to the joint contributions from the singly occupied Mn 3d orbitals d_{xz}, d_{yz}, d_{z^2} and d_{xy} among which d_{xz} and d_{yz} are energetically degenerate. The second absorption features at 641.8 eV are entirely SOC-induced, based on the comparison between Figure 42 (b and c), where the features indicated by green arrows in Figure 42 (b) are absent if the SOC is not included in the simulations (Figure 42 (c)).

The third absorption features at 644.2 eV are from the empty orbital $d_{x^2-y^2}$. Unfortunately, the simulations (Figure 42 (b)) produce almost identical theoretical spectra for both Mn porphyrin complexes, failing to reproduce the different spin-orbit splitting observed in Figure 39 (a). This is expected since the calculated Mn-N bond lengths and angles after the geometry optimizations are almost identical for both molecules, as illustrated in Figure 42 (c) and the Table in appendix 8.10. The different outer ligands, as well as their geometrical arrangements - four phenyl groups of MnTPP symmetrically distributed at the porphyrin peripheral while eight ethyl groups of MnOEP located at only one side of the porphyrin plane, appear to have little influence on the porphyrin central structure. In other words, the different outer ligands do not produce different ligand fields around the Mn centers in two Mn porphyrins according to the gas phase calculations,

leaving only one option - extra binding of the Mn center to solvent molecules to create different ligand fields. Note that the gas phase calculations do not consider the solvent effect around the solvated porphyrins.

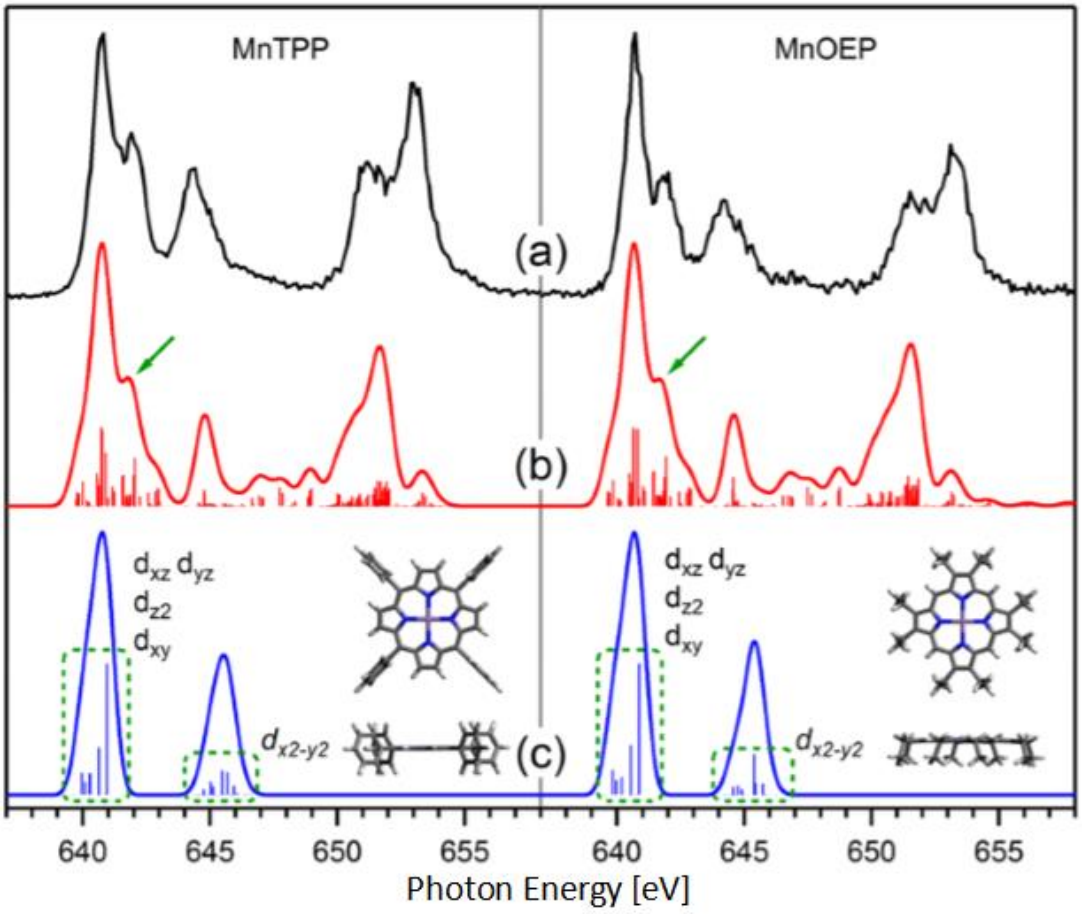

Figure 42. Comparison of the experimental PFY-XA spectra of MnTPP and MnOEP (a), identical to the spectra in Error! Reference source not found. **(a), with the simulated spectra with spin-orbit oupling (SOC) included (b) and excluded (c). Numerous vertical sticks represent the calculated transition moments. The high spin configuration S = 2 (d^4 for Mn^{3+}) with Cl^- detached from the molecule is adopted for the calculations of both Mn porphyrins in (b) and (c). The computed spectra are shifted *ad hoc* 16.0 eV (red trace) and 12.8 eV (blue trace) for MnTPP, while 15.8 eV (red trace) and 12.6 eV (blue trace) for MnOEP. The geometry optimized structures of the two molecules are presented at the bottom as top view and side view.**

When the Mn porphyrin complexes are dissolved in CH_2Cl_2, the different outer ligands may cause significantly different interactions of the Mn centers with solvent molecules. It is very much desirable to theoretically simulate the RIXS processes for the solvated Mn porphyrin molecules in order to uncover the detailed transition mechanism of the feature S observed in Figure 42 d. However, such calculations are extremely difficult at present, if not impossible. There are no RIXS calculations successfully done so far on such a

complex metalloporphyrin molecular system that are in good agreement with the experimental data, to our best knowledge. Some RIXS calculations have been previously applied only on simple transition metal complexes [50,205,206]. Similar porphyrin solutions with different metal centers, FeTPP-Cl and FeOEP-Cl dissolved in CH_2Cl_2, have been investigated in another study, too [54]. The outer ligands as the ethyl groups in FeOEP-Cl have been demonstrated to be able to assist the binding of solvent molecules to the metal center. Similar behavior is reasonably expected for MnOEP dissolved CH_2Cl_2, which can provide a stronger ligand field around the MnOEP metal center causing a larger spin-orbit splitting observed in Figure 39 (a). The additional solvent ligand can also contribute extra orbitals into the MnOEP valence levels and consequently enhance the valence orbital density around the porphyrin metal center. These extra valence orbitals from the solvent ligation may delocalize between the Mn center and its coordinated N, strengthening the Mn-N orbital mixing, thereby providing extra channels for the MLCT. The additional valence orbitals from the solvent ligand are mainly with 2p character, so that they can enhance the cross-section between the N 1s and valence 2p transitions as well that is required for the observations of the stronger elastic feature in Figure 40 (c and d) for MnOEP. The different Mn porphyrin outer ligands have no direct effect on the electronic structure of the porphyrin central part as demonstrated by the DFT/ROCIS calculations (Figure 42 (b)), but indirectly influence it through the different extents of the assisted binding of the solvent molecules to the Mn centers.

4.3.2 Metal-Solvent Interaction Assisted by Porphyrin Outer Ligands

Jie Xiao, Ronny Golnak, Kaan Atak, Mika Pflüger, Marvin Nicolas Pohl, Edlira Suljoti, Bernd Winter, Emad F. Aziz. **The Assistance of the Iron Porphyrin Ligands to the Binding Interaction between the Fe Center and Small Molecules in Solution**. *J. Phys.Chem. B (2014),* DOI:10.1021/jp5023339

For the study of the effects on porphyrin´s metal center chemistry in solution, iron octaethylporphyrin chloride (FeOEP-Cl, CAS: 28755-93-3) and iron tetraphenyl-porphyrin chloride (FeTPP-Cl), CAS: 16456-81-8) were selected. Both of them were dissolved in dichloromethane (CH_2Cl_2) as solvent. The molecular structures of these porphyrines are shown in Figure 43. The Fe center of the porphyrin´s is at the stable 3^+ oxidation state. In both molecules only one type of the side ligands exists. Eight ethyl groups in FeOEP-Cl and four phenyl groups in FeTPP-Cl. This rules out additional

interactions that may occur between dissimilar ligands. Only one type of small molecule, CH_2Cl_2 is present in both sample solutions, which interacts with the Fe center and serves as solvent at the same time. The choice of CH_2Cl_2 as solvent is also driven by the considerably higher solubility of this chlorinated molecule as compared to other commonly used organic solvents. This is important here in order to obtain reasonably large solute signal in the X-ray absorption spectra. In addition chemical interactions of CH_2Cl_2 with the Si_3N_4 membrane of the liquid flow cell are avoided. A degradation and/ or breaking of the membrane does not occur upon intense synchrotron radiation during the measurements. If a small solvent molecule binds to the Fe site, the Fe center will be coordinated by six atoms (four N and two Cl) forming a distorted octahedron. According to O_h symmetry, the resulting ligand field leads to a splitting of the Fe 3d orbitals into two groups: e_g ($d_{x^2-y^2}$, d_{z^2}) and t_{2_g} (d_{xy}, d_{yz}, d_{xy}), corresponding to the two major absorption peaks observed in our X-ray absorption measurements, as shown in Figure 44.

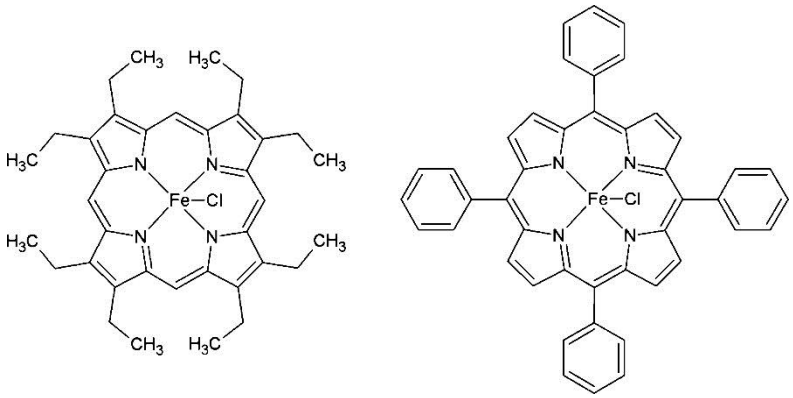

Figure 43. Structural formula of FeOEP-Cl (left) and FeTPP-Cl (right)

Obtained PFY and RIXS spectra of FeOEP-Cl and FeTPP-Cl are shown in Figure 44, in blue and red, respectively. Although both molecules have the same nominal Fe^{3+} oxidation state, an overall energy shift of 0.4 eV to lower excitation energy of the FeOEP-Cl PFY spectrum is observed when compared with the FeTPP-Cl PFY spectrum, as marked by green dashed lines in Figure 44(A). Such a shift suggests that the actual Fe oxidation state in FeOEP-Cl is a little lower than that in FeTPP-Cl. A second distinctive spectroscopic feature in these two molecules' PFY spectra is the relative intensity ratio of the two leading absorption peaks, marked by the same green dashed lines mentioned above. The difference of the peak-intensity ratio observed in the PFY spectra is corroborated in the corresponding RIXS measurements at the excitation energies of 708.8 eV and 710.5 eV in Figure 44(B). Quantification of additional spectral differences for the

two porphyrins, especially at the L_2 edge, would be difficult due to a fairly low signal-to-noise ratio. It is reminded that the low solute concentration requires a total data acquisition time of approximately 12-14 h per PFY spectrum, as presented in Figure 44(A).

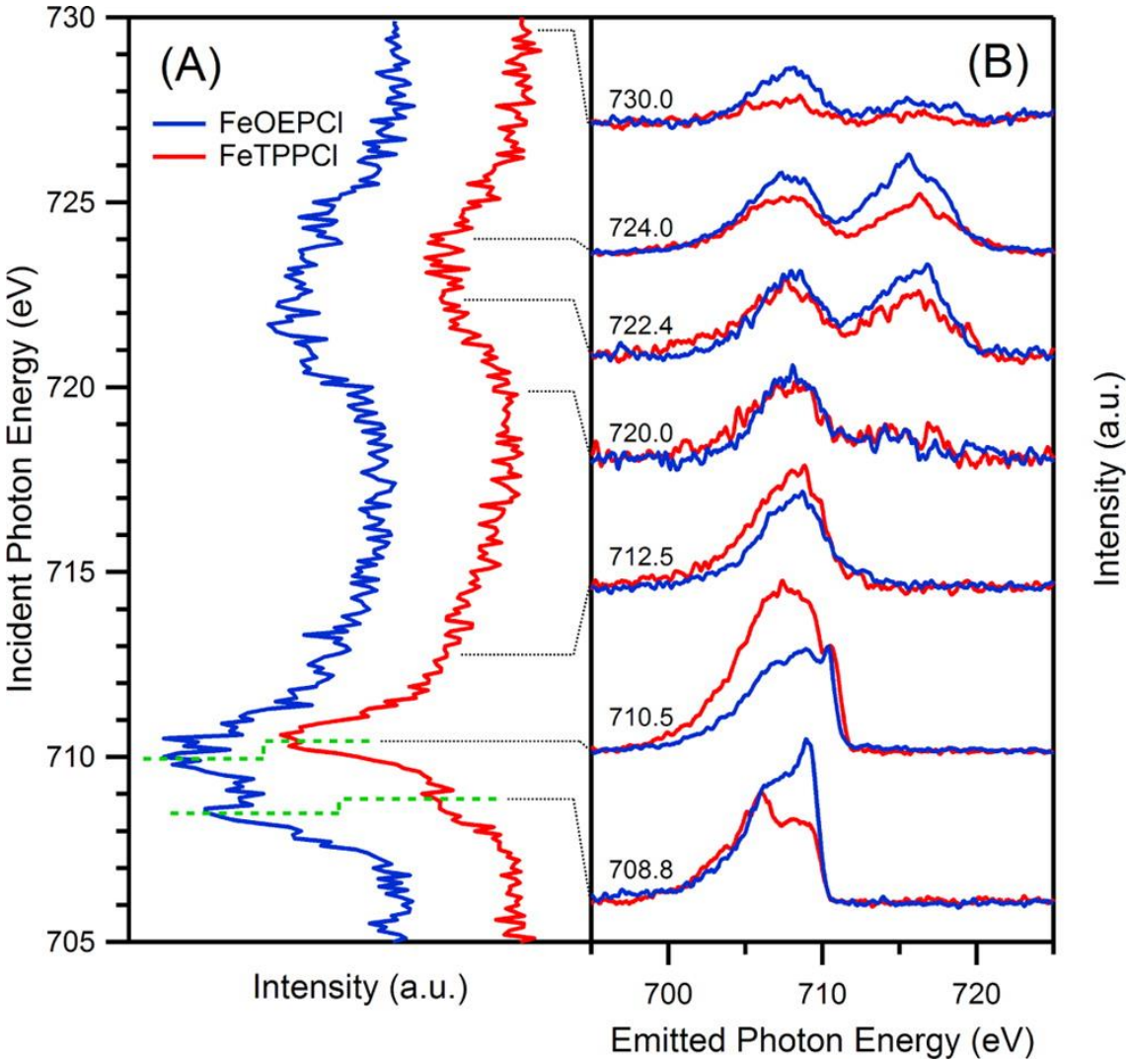

Figure 44. (A) PFY spectra of FeOEP-Cl with 15 mM concentration (blue trace) and FeTPP-Cl with 25 mM concentration (red trace), both dissolved in CH_2Cl_2. Green dashed lines mark the first two major absorption peaks and indicate an overall 0.4 eV shift relative to each other. (B) RIXS spectra of two porphyrins at indicated excitation energies. All RIXS spectra are plotted against emission photon energy instead of loss energy due to the constant emission energies of spectral features at various excitation energies. Each RIXS spectrum is normalized to its background signal for intensity comparison with others.

The general character of the RIXS spectra in Figure 44(B) is a broad featureless peak which is constant at a certain emission energy for each absorption edge, indicating that the Fe 3d electronic systems in both porphyrins have little correlation [186]. That is, the Fe 3d valence orbitals appear to be delocalized over the ligands for both molecules. Despite

the rather similar RIXS spectra for the two different molecules at most excitation energies, RIXS spectra at 708.8 eV and 710.5 eV in Figure 44(B) unambiguously reveal distinctly different behavior in the relative intensity. An opposite trend in signal intensities can be observed, i.e., larger overall intensity for the FeOEP-Cl than for FeTPP-Cl at 708.8 eV excitation energy, and the reverse for 710.5 eV. Such an effect cannot be explained by the different concentrations only. Unlike the XA spectra of Figure 44(A), the RIXS spectra, measured here at few selected excitation energies and over an extended sampling time, exhibit good signal-to noise ratio, and the quantitative comparison of the signal intensities for the two porphyrins is well justified. One has to note that signal integration of the RIXS spectrum at a given excitation energy yields the PFY spectrum; for the measurement of the actual PFY spectrum of Figure 44(A), each data point (integrated from an actual RIXS spectrum) had to be collected over a much shorter time though, which is the reason for the unsatisfactory signal level. Hence, the above-mentioned opposite intensity trends in the good-quality RIXS spectra for excitation at the two leading XA peaks supports a corresponding intensity change in the PFY spectra; experimentally, this effect cannot be unequivocally resolved here, as have been argued above. This different intensity ratio for the two leading absorption peaks together with the aforementioned 0.4 eV energy shift in Figure 44(A) strongly indicates that the Fe ions in the two porphyrin centers have different chemical environments and hence different ligand fields altering the electronic structure of the Fe site.

The geometry optimizations from the DFT calculations, however, give almost identical bond distances and bond angles of Fe-N and Fe-Cl for both porphyrins (compare with Figure 45), which should result in very similar electronic structure of the Fe centers for both molecules. So the different ligand fields around the two porphyrin Fe centers are very unlikely caused by their original molecular geometric structures. Since the Fe center in each porphyrin molecule still has one absorption site vacant (opposite to the Cl^- in the original porphyrin), it can be hypothesized that the Fe ion in one of the porphyrin molecular centers has a stronger interaction with solvent molecules through that site than in the other, resulting in different ligand fields due to the different Fe coordinates of the octahedron. Since it is the FeOEP-Cl PFY spectrum (blue trace in Figure 44(A)) being shifted 0.4 eV to lower excitation energy, Cl from CH_2Cl_2 is thus most likely to bind to the Fe center of FeOEP-Cl and donates some electron charge to the Fe^{3+} ion. This slightly lowers the actual oxidation state of the Fe^{3+} in FeOEP-Cl. For FeTPP-Cl, on the other

hand, such an interaction of Fe center with small solvent molecules seems to be negligible or is at least less significant than in the FeOEP-Cl solution.

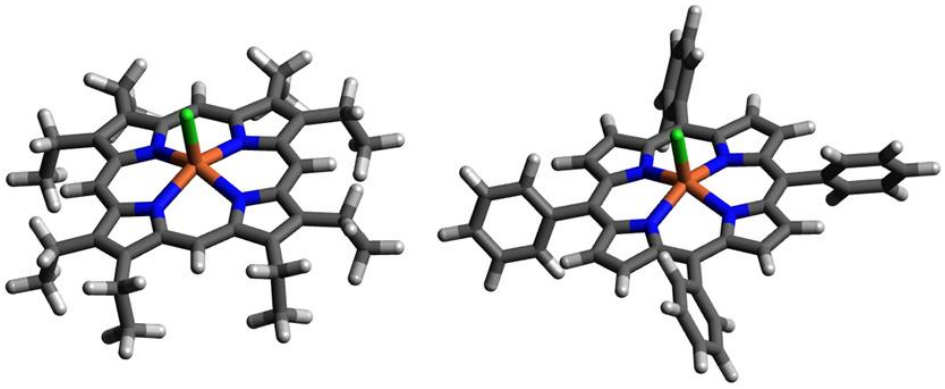

FeOEP-Cl		**FeTPP-Cl**	
Bond distance	Bond angle	Bond distance	Bond angle
Fe-Cl: 2.245 Å	Cl-Fe-N: 104.6°	Fe-Cl: 2.247 Å	Cl-Fe-N: 104.4°
Fe-N: 2.105 Å	N-Fe-N: 86.3°	Fe-N: 2.100 Å	N-Fe-N: 86.5°
Total dipole moment: 3.77 Debye		Total dipole moment: 3.09 Debye	

Figure 45. DFT-optimized molecular geometries for high spin 2s + 1 = 6 with the bond parameters of the Fe center to the nearest ligand atoms for FeOEP-Cl (left) and FeTPP-Cl (right). Both porphyrins have a 4-fold symmetry C_{4v} in the molecular center part which contains Fe, four N and one Cl. The dipole moments of the two porphyrin molecules are also indicated in the individual table.

The DFT/ROCIS calculations for various molecular configurations also support aforementioned hypothesis that the two Fe centers have considerably different affinities of binding Cl from solvent molecule. The various molecular configurations include three possible Fe-Cl bonding situations, each of which has three possible spin multiplicities. The original Cl^- ion in both porphyrin complexes either remains bound to Fe^{3+}, or the halide detaches when dissolved in the polar solvent dichloromethane. The Cl from solvent CH_2Cl_2 may also bind to Fe^{3+} to complete all six coordination sites around the Fe center in an approximate octahedral symmetry. Therefore, three Fe-Cl bonding situations in solution can be distinguished: Fe binding to (1) no Cl, (2) one Cl, or (3) two Cl ions. Since Fe^{3+} oxidation state has d^5 electronic configuration, there are three possible spin multiplicities for each Fe-Cl bonding situation, i.e., 2s + 1 = 2, 4, 6 [40,44,45,207]. Therefore,

a total of nine different molecular configurations may exist for each porphyrin complex when dissolved in CH_2Cl_2 solvent.

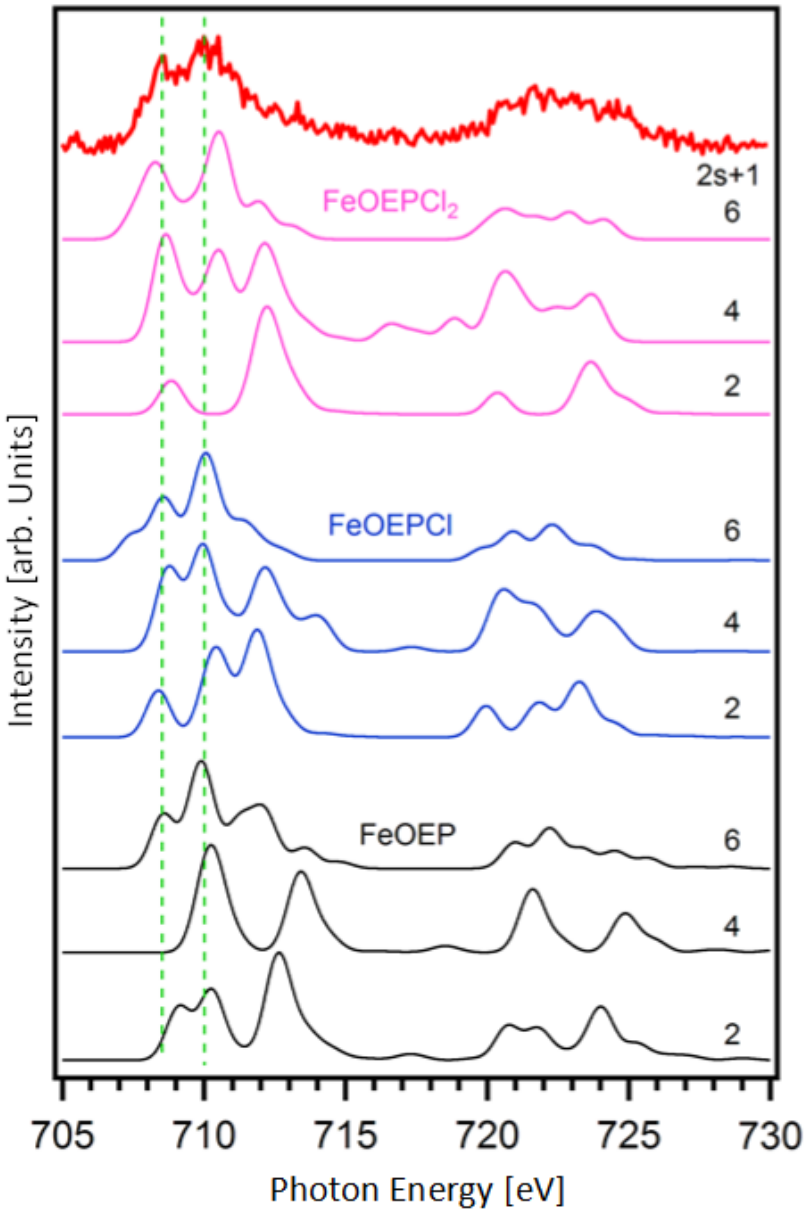

Figure 46. DFT/ROCIS calculations at the Fe L-edge for FeOEP-Cl complex. Three different Cl^- coordinations to the Fe center, *i.e.* 1) Fe binding to no Cl (black traces), 2) Fe binding to one Cl (blue traces, original porphyrin structure) and 3) Fe binding to two Cl (pink traces), with three possible spin multiplicities 2s+1 = 2, 4, 6 for each Cl coordination situation are presented, along with the experimental PFY spectrum on the top for comparison. The top PFY spectrum is identical to the blue trace in Figure 44(A) and Figure 48a. All the calculated spectra are shifted to higher energies to align with the experimental spectrum on the top. The green dashed lines are used to mark the first two major absorption features (t_{2g} and e_g) in the spectra.

All nine structures were calculated and are presented in Figure 46 and Figure 47 along with the respective experimental PFY spectrum shown at the top of each figure for

comparison. It is noted that the theoretical simulation of the two-Cl case (3) was done for the molecular structure of two isolated Cl^- ions attached to the Fe center from opposite sides. This symmetry, corresponding to maximized interaction between the Fe center and the Cl^- from the solvent molecule, is the preferred structure obtained from geometry optimization.

Our simple structure model represents one single relevant snapshot of the many existing dynamical structures in the real solution, but it is yet useful in the theoretical simulation of the qualitative binding interactions. This simple model might be unsuitable though to predict accurate bond strengths or solute and ligand contributions to the bond. Quantification of these effects would exceed current computational capabilities.

Overall shapes of the measured PFY spectra are yet distinct enough to allow for the quantitative comparison with the calculated spectra (see Figure 46 and Figure 47). The best matching theoretical calculations, along with their experimental spectra are reproduced in Figure 48 for both porphyrins. Colors in Figure 48b and Figure 48e follow the same color codes used in Figure 46 and in Figure 47. Judged by the peak positions and intensities of the first two leading absorption peaks at the L_3 edge, marked by green dashed lines in Figure 48 (and also in Figure 46 and Figure 47), the best matching calculated spectrum for FeTPP-Cl is the one from the original molecular structure (Fe binds to a single Cl) with high spin multiplicity $2s + 1 = 6$, as shown in Figure 48e (also the top blue trace in Figure 47), and importantly no other calculated spectrum matches the experimental data or would contribute significantly to it.

For FeOEP-Cl, the same computed spectrum of the original molecular structure with high spin multiplicity 6 (blue trace in Figure 48b) seems to also reproduce the respective experimental data. However, the blue trace in Figure 48b (also the top blue trace in Figure 46) is almost identical to Figure 48e, and this cannot explain the observed difference of the intensity ratio of the two leading absorption peaks for two porphyrin complexes. Hence, another theoretical spectrum, pink trace in Figure 48b (same as the top pink trace in Figure 46), representative of a configuration of Fe binding to two Cl with high spin multiplicity 6, needs to be invoked to account for the relatively enhanced first absorption peak at 708.4 eV for FeOEP-Cl. Moreover, the larger distance between the first and second absorption peak positions in the pink trace than found in the blue trace of Figure 48b could further explain the broader second absorption peak at 710.5 eV of the FeOEP-Cl PFY spectrum when compared to the FeTPP-Cl PFY spectrum, as shown in Figure

44(A) and Figure 48a,d. Traces in Figure 48c and Figure 48f are the calculations without spin-orbit coupling perturbation, which significantly reduces the number of transitions and allows to identify the unoccupied states contributing most to the X-ray absorption transitions at the Fe $L_{2,3}$ edge.

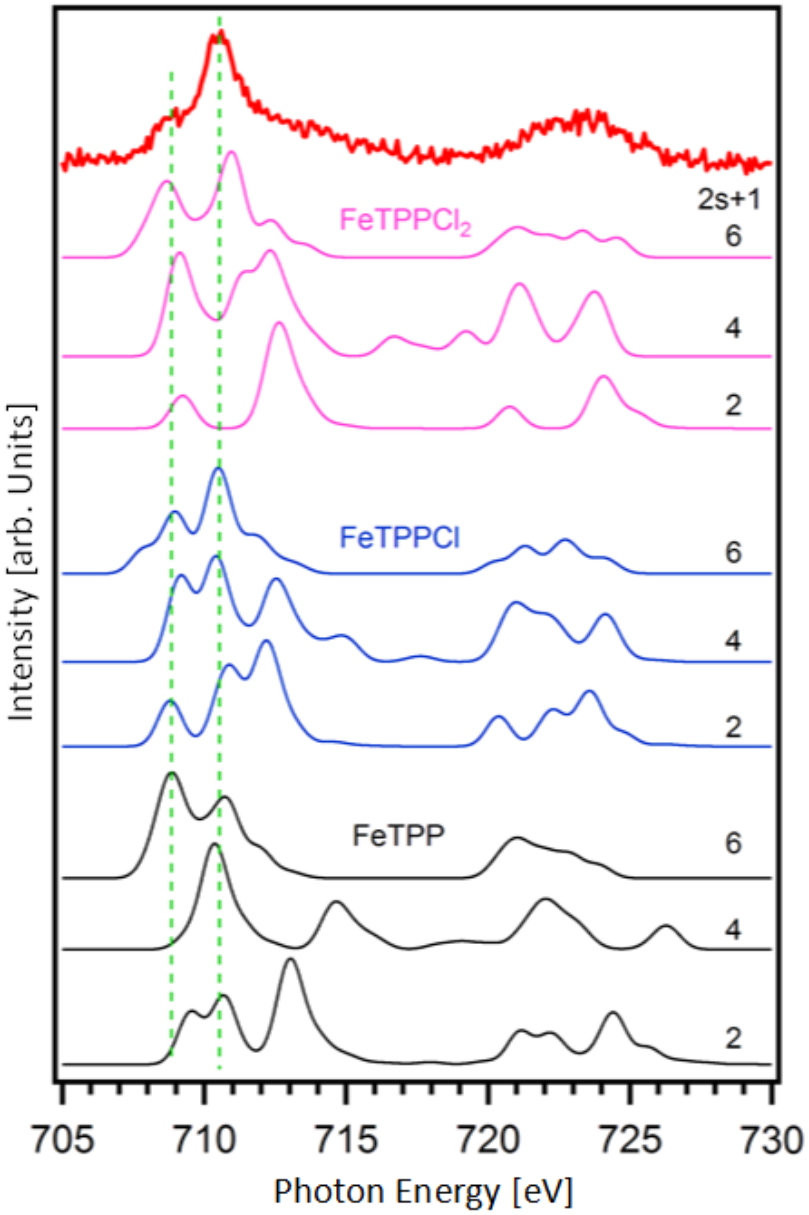

Figure 47. DFT/ROCIS calculations at the Fe L-edge for FeTPP-Cl complex. Three different Cl^- coordinations to the Fe center, *i.e.* 1) Fe binding to no Cl (black traces), 2) Fe binding to one Cl (blue traces, original porphyrin structure) and 3) Fe binding to two Cl (pink traces), with three possible spin multiplicities 2s+1 = 2, 4, 6 for each Cl coordination situation are presented, along with the experimental PFY spectrum on the top for comparison. The top PFY spectrum is identical to the red trace in Figure 44(A) and Figure 48d. All the calculated spectra are shifted to higher energies to align with the experimental spectrum on the top. The green dashed lines are used to mark the first two major absorption features (t_{2g} and e_g) in the spectra.

Five unoccupied Fe 3d orbitals, indicated inside the green squares in Figure 48, are found to have the most significant contributions to the observed X-ray absorption. The first absorption peak located near 708.4 eV for the FeOEP-Cl complex, and 708.8 eV for the FeTPP-Cl complex, mostly originate from t_{2_g} orbitals, while the second absorption peak at approximately 710.5 eV for both porphyrins arises from e_g orbitals, as indicated by green dashed squares in Figure 48. This is consistent with the assignment of previous calculations using a different method [41]. One has to refer to the Table in appendix 8.11 as well as Figure 50 in the appendix 8.12 for the detailed information about atomic and orbital contributions to each molecular orbital. Despite the quite good agreement between the theoretical simulations and the experimental spectra, binding strengths and the percentage of the two Cl bound complexes for FeOEP-Cl cannot be determined here, using a very simple structure model as explained above. In addition to the different binding situations, charge transfer at the Fe site also affects the relative peak intensities [142]. It will reduce the relative intensity of t_{2_g} spectral feature (the marked absorption peak around 708.8 eV), as is indeed observed when comparing Figure 48d with Figure 48e for FeTPP-Cl. It is not possible to quantify charge transfer on the level of the theory performed here. Given the almost identical geometrical structures for the central part of the two porphyrins (Figure 45), charge transfer is argued to lead to noticeable spectral differences only due to the extra binding discussed here.

The inclusion of an additional binding interaction between the Fe^{3+} center and a Cl from solvent molecule CH_2Cl_2 for FeOEP-Cl in solution, as quantified in our DFT/ROCIS calculations, well explains the observed differences of spectroscopic features in Figure 44(A). As mentioned above, any experimental and theoretical differences inferred from the comparison of the two porphyrin complexes studied here must originate from their side ligand groups. What remains to be discussed is how the side ligand connects to the observed differences described in the previous paragraphs. Specifically, why does FeOEP-Cl have such a binding interaction with small solvent molecules, while FeTPP-Cl does not? One can argue that this difference is due to the geometrical structures of these side ligands as well as their arrangements and locations with respect to the porphyrin molecular plane.

The geometry optimizations of the two porphyrin complexes indicate that both molecules have almost identical center parts, which defines the molecular plane containing the Fe center and all the N atoms and also defines the molecular axis along the Cl-Fe bond

direction perpendicular to the molecular plane (see Figure 45). Because of this similarity, DFT/ROCIS calculations give almost identical theoretical spectra for both porphyrin molecules, shown as blue traces in Figure 48b,e. For the side ligands, eight ethyl groups in FeOEP-Cl complex are all located on one side of the molecular plane with Cl^- ion on the other side, giving rise to a total dipole moment of 3.77 D according to the DFT geometry optimization. The four phenyl groups (with the phenol molecular plane being almost perpendicular to the porphyrin plane) in FeTPP-Cl, on the other hand, are symmetrically distributed on both sides of the porphyrin molecular plane, resulting in a total 3.09 D dipole moment. FeOEP-Cl has hence larger electrostatic attraction to the polar solvent molecule dichloromethane, which has a dipole moment of 1.65 D.

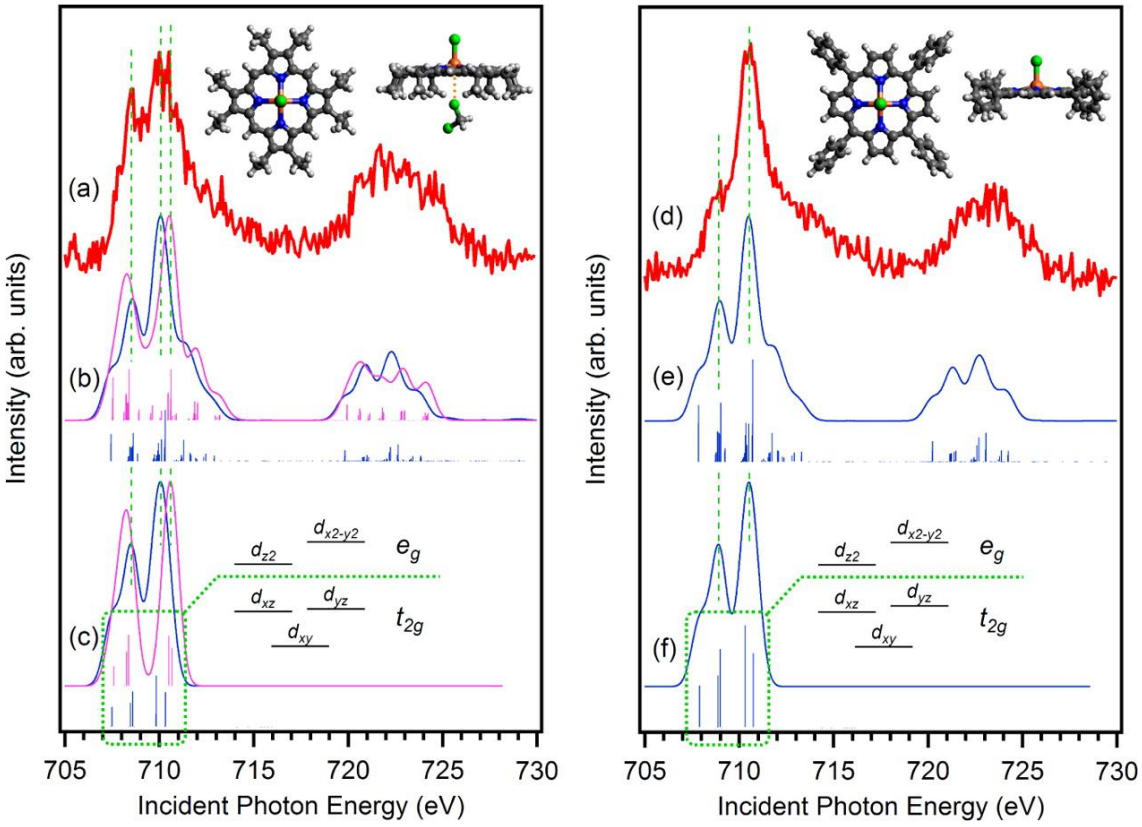

Figure 48. PFY spectra of FeOEP-Cl (a) and FeTPP-Cl (d), identical to the blue trace and red trace in Figure 44(A), respectively, compared with their corresponding DFT/ROCIS calculations. The calculated spectra (b) and (e) are duplicates of the top pink and top blue traces in Figure 46 for FeOEP-Cl and top blue trace for FeTPP-Cl in Figure 47 with spin-orbit coupling (SOC) perturbation included. (c) and (f) are calculated XAS spectra at L_3 edge only without SOC. The vertical bars under each simulated spectrum represent the transition moments from Fe 2p to valence orbitals. The insets on the top of the figure are the top and side views of the molecular structures after geometry optimizations. For FeOEP-Cl, an extra binding interaction with a solvent molecule is also illustrated.

When a CH_2Cl_2 molecule approaches the Fe center with one of its negatively charged Cl at the front, an extra Fe^{3+}-Cl^- ion pair may form, which is probable for both porphyrins in solution. The experimental data combined with the theoretical calculations suggest though that such an ion pair (CH_2Cl_2 binding to Fe center) is only stabilized in the FeOEP-Cl solution, creating a different ligand field around the Fe center that alters the Fe electronic structure. The stabilization of the binding interaction is probably assisted by the side ligands of FeOEP-Cl. The eight ethyl groups with positive charged H atoms terminating the side ligands could create an electrostatic field around the porphyrin molecule [208]. Such a field, when superimposed with the electrical field created by the Fe^{3+} in the molecular center, causes a local minimum in the energy potential directly below the Fe center along the molecular axis for negative charge. The proposed ligand-assisted binding process for FeOEP-Cl is illustrated in Figure 49. The ligand-induced electrostatic field may help keep the Cl of the approaching CH_2Cl_2 bound to the Fe center, similar to the "pocket" effect in the case of large protein present in hemoglobin or myoglobin [209]. The Fe^{3+}-Cl^- ionic attraction, indicated by the red arrows in Figure 49, is present in both porphyrin solutions but may not be strong enough to keep the approaching solvent molecule in the vicinity of the Fe centers if there is no assistance from the ligands. The H atoms in the phenyl groups of FeTPP-Cl cannot produce a similarly strong electrostatic field to assist the binding process because they are fewer in number and farther in distance to the Fe center. Also, the ethyl groups of FeOEP-Cl are less constrained and have a larger flexibility to orient their arms in liquid phase, reaching out for nearby Cl from the solvent molecule to "grab" the dichloromethane molecule. Some of the ethyl arms may also reach to the Cl^- ion of the porphyrin itself in solution due to the Coulombic attraction.

It is noteworthy that the left FeOEP-Cl geometric structure in Figure 49 (also the top inset in Figure 48) is DFT-optimized for the isolated molecule (gas phase). The arrangement of the ethyl groups in the liquid phase may differ when surrounded by numerous solvent molecules. For the extra binding interaction with the solvent molecules, the DFT geometry optimization and the following DFT/ROCIS calculations were only performed on the molecular configuration of the Fe center bound to two Cl^- ions (both Cl^- are single ions, none being part of CH_2Cl_2) in the gas phase for both porphyrins. The arrangement of the eight ethyl groups in the right molecular geometry of Figure 49 depicts the binding process in solution proposed here. It is concluded that such a molecular geometry can assist the binding process and explain the observed differences in the two porphyrins'

experimental spectra. The DFT simulation of the iron porphyrin surrounded by numerous CH_2Cl_2 solvent molecules, as occurring in real solutions, exceeds our computation capability. However, it is clear that solvent molecules bind more strongly to the FeOEP-Cl than to the FeTPP-Cl based on our experimental data and DFT/ROCIS calculations.

During the proposed binding process (Figure 49), the polar and flexible ethyl groups, combined with the larger molecular dipole moment (also induced by the polar side ligands), drive the increased electrostatic interaction between the Fe center of FeOEP-Cl and the small solvent molecule CH_2Cl_2 in solution. It should be noted that the chosen solvent molecule CH_2Cl_2 is just one example of a test molecule, representing a class of small molecules, such as O_2, CO, etc., existing in a real biological system. The finding of the extra binding between the Fe center and small solvent molecules is not specific to the Cl of the solvent. Hence, the binding interaction of the Fe center of FeOEP-Cl with other non-chlorinated small molecules is also expected under the ligand assistance.

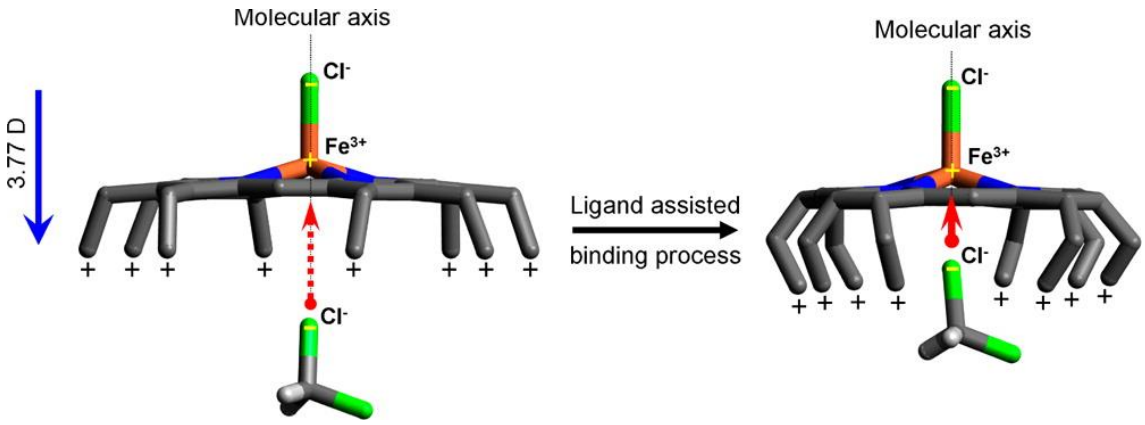

Figure 49. Illustration of the proposed ligand-assisted binding process of FeOEP-Cl with CH_2Cl_2 solvent molecule. The molecular dipole moment of 3.77 D is indicated by a blue arrow on the left for the DFT-optimized original molecular structure (left schematic). The H atoms in FeOEP-Cl are omitted for clearer view except for those terminating the ethyl ligand groups which are represented by "+" signs. Molecular axis is defined along the Cl-Fe bond direction and perpendicular to the molecular plane, marked by dashed black lines. The ionic interaction between the Fe^{3+} center and the Cl of CH_2Cl_2 is indicated by a dashed long red arrow (left) when the solvent molecule is far and the binding is weak and a solid short red arrow when the solvent molecule is close to the Fe^{3+} center and the binding becomes stronger (right).

5 Summary and Outlook

I have firstly presented the investigations of the electronic structure on a relatively simple system - ferrous and ferric aqueous solutions, using synchrotron based resonant photoelectron spectroscopy (RPES) and X-ray absorption/emsission spectroscopy (XAS/XES) on liquid micro-jet in vacuum. This is a relatively new route in a still young field of soft X-ray spectroscopies on highly volatile solutions. By combining photon in/ electron out and photon in/ photon out techniques important electronic structure details are revealed. Due to the combination we can considerably advance our understanding of electronic ground- and excited state properties. We have systematically compared all possible decay channels upon resonant excitation at the Fe L edge in iron aqueous solution, including radiative (i)PFY and non-radiative PEY both in valence and core-level emissions, in order to discover an undistorted detection method for XAS measurements.

Previously reported X-ray spectroscopy studies mostly relied on the photon detection or total electron yield (TEY) and did not consider the electronic structure information obtained from the individual electron-emission channels. The joint consideration of PFY and PEY spectra originating from various channels evidences large deviations from the true absorption spectra in case of the 3d → 2p relaxation and fairly good reliability of the "core" PFY and PEY spectra due to the 3s → 2p relaxation. In fact our measurements suggest that probing the 3s channel (investigated here for fluorescence) yields a more accurate true absorption spectrum. Looking at the 3d → 2p relaxation channel and using the alignment suggested in this work, one can determine the correspondence between RPE and RIXS spectral signatures. Comparing RPE and RIXS intensities one may obtain information on the competition between the radiative and non-radiative decay channels. Our analysis suggests a new protocol for investigation of X-ray spectra and its implications for the study of transition metal solute - solvent electronic interactions, being important to promote understanding structure and rational design of catalytic and other functional materials.

Furthermore my PhD study was extended onto the electronic structure investigations of a more complex system - porphyrins in solution. Here the available instrumental techniques are limited to flow cell due to low sample volume and concentration. We have reported the first L edge RIXS spectra of monomeric iron protoporphyrin IX chloride (FePPIX-Cl/ hemin) and cobalt protoporphyrin IX chloride (CoPPIX-Cl) in dimethyl sulfoxide.

Aided by ab initio calculations the emission spectra can be almost quantitatively interpreted in terms of the orbitals involved in the excitation and de-excitation processes. From the RIXS spectra we also constructed the so-called partial fluorescence yield X-ray absorption spectrum which can be interpreted more accurately than previous spectra based on total-yield measurements. Overall, our experimental and computational findings for FePPIX are in qualitative accordance with previous results, essentially supporting a hemin-Cl structure in high-spin configuration.

The study about CoPPIX shows that the cobalt center-ion adopts a low-spin configuration. In addition, the calculations reveal that the cobalt ion is 5-coordinated, binding to four nitrogen atoms and one chloride ion, or 6-coordinated where cobalt binds additionally to an oxygen of the DMSO solvent. The local HOMO-LUMO gap at the Co site was revealed by RIXS measurements with the excitation energy at the pre-absorption edge. By changing the solvent from DMSO to H_2O the FePPIX forms dimers. A local energy gap opening at the Fe center is observed experimentally, when compared with hemin in DMSO.

The orbital localization induced by hemin dimerization in water through π-π stacking of the porphyrin outer ligands is argued to be responsible for the observed gap opening, as well as for associated peak narrowing in XES spectra. When applying N K edge X-ray spectroscopy, characteristic features in the spectra are identified and associated with electronic structure changes arising from hemin intermolecular bonding interactions. The spectral evolutions of these features upon the development of hemin-hemin interactions were further analyzed at the molecular orbital level derived from the DFT calculations. The results show that N K edge X-ray spectroscopies provide experimental access to porphyrin intermolecular interactions in solution by tracking the energy shifts of the characteristic N K edge XA features, crucially permitting in situ detection for electronic structure investigations. The exact energy positions of these characteristic features also provide a reference to help identify hemin oligomer species in solution, e.g. monomer in DMSO or dimer in aqueous solution.

Investigations were carried on, concerning outer ligand effects on the electronic structure of central metal ions in porphyrins. We studied manganese octaethyl porphyrin (MnOEP) and manganese tetraphenyl porphyrin (MnTPP) dissolved in CH_2Cl_2 (DCM). Metal-to-ligand charge-transfer (MLCT) is directly observed in MnOEP solution, owing to the RIXS measurements. It is a clear indication of strong Mn-N valence orbital mixing that

plays a significant role in the metalloporphyrin functionality. By comparing the experimental and theoretical spectra of MnOEP to those of MnTPP the influence of the outer ligands on the MLCT as well as the electronic structure of the Mn center is demonstrated. The flexible ethyl groups of MnOEP in solution are more capable of assisting the binding of the solvent molecules to the Mn center, resulting in the distinctive MLCT feature. This study may inspire a new approach of tuning the charge-transfer property in metalloporphyrins by artificially designing their outer ligands.

When comparing iron octaethyl porphyrin chloride (FeOEP-Cl) with iron tetraphenyl porphyrin chloride (FeTPP-Cl), our soft X-ray absorption and emission spectroscopy measurements, combined with DFT/ROCIS calculations, strongly indicate that the Fe center of FeOEP-Cl porphyrin has a stronger binding interaction with the solvent molecule CH_2Cl_2 in solution when compared to FeTPP-Cl. This difference is mainly attributed to the different extent of the ligand assistance to the binding process. Our finding will help understand, on the microscopic level, how O_2 or other small molecules bind to iron porphyrin in biologically relevant systems. This work also motivates future researches on the artificial tuning of the porphyrin functionality by modifying the outer ligands.

Liquid phase is an interesting as well as realistic environment for chemistry as it hosts many of the chemical processes in nature and in industrial applications. We have demonstrated in this perspective by various examples how an understanding of the nature of different chemical behaviors in liquid phase can be achieved by combining the recent developed soft X-ray spectroscopic techniques for liquid samples. In the future newly developed recycle micro-jets combined with pump-probe spectroscopy will help observe the dynamics of biochemical functions under real conditions (room temperature and pressure). In future research this setup will be used on the one hand for studying molecular dynamics in solution in tens of picoseconds time scale at the soft X-ray synchrotron facilities, where the core-levels of the elements of interest can be probed. For these experiments, a femtosecond laser pump pulse is combined with the ~70 picosecond soft X-ray probe. Valence band dynamics in the range of the tens of femtoseconds on the other hand will be addressed by using ultra- and extreme ultra-violet light pulses obtained by high-harmonic-generation (HHG) in laser based table-top experiments. Here a ~20 fs laser pump source will be used to excite the sample, followed by an HHG pulse in the energy range up to 100 eV to probe the change in the valence band of the excited systems.

The first demonstration of this technique on a micro-jet has been presented by Abel and co-workers [210]. While the HHG will reveal dynamics of the valence band, the XFEL can probe such dynamics at the core level (beyond the water window).

6 Bibliography

1. Röntgen, W. C. Ueber eine neue Art von Strahlen. *Ann. Phys.* **300,** 12–17 (1898).
2. The Nobel Prize in Physics 1901. (2015). at <http://www.nobelprize.org/nobel_prizes/physics/laureates/1901/>
3. The Nobel Prize in Physiology or Medicine 1962. (2015). at <http://www.nobelprize.org/nobel_prizes/medicine/laureates/1962/>
4. Day, C. Ultrafast x-ray diffraction tracks molecular shape-shifting. *Phys. Today* **54,** 19–20 (2001).
5. Milgrom, L. R. *The Colours of Life: An Introduction to the Chemistry of Porphyrins and Related Compounds*. (Oxford University Press, 2001).
6. Itagaki, Y., Deki, K., Nakashima, S.-I. & Sadaoka, Y. Toxic gas detection using porphyrin dispersed polymer composites. *Sens. Actuators B Chem.* **108,** 393–397 (2005).
7. Sonoyama, N., Kirii, M. & Sakata, T. Electrochemical reduction of CO2 at metal-porphyrin supported gas diffusion electrodes under high pressure CO2. *Electrochem. Commun.* **1,** 213–216 (1999).
8. Tributsch, H. & Calvin, M. Electrochemistry of Excited Molecules: Photo-Electrochemical Reactions of Chlorophylls*. *Photochem. Photobiol.* **14,** 95–112 (1971).
9. O'Regan, B. & Grätzel, M. A low-cost, high-efficiency solar cell based on dye-sensitized colloidal TiO2 films. *Nature* **353,** 737–740 (1991).
10. Imahori, H., Mori, Y. & Matano, Y. Nanostructured artificial photosynthesis. *J. Photochem. Photobiol. C Photochem. Rev.* **4,** 51–83 (2003).
11. Udal'tsov, A. V., Kazarin, L. A., Sinani, V. A. & Sweshnikov, A. A. Water–porphyrin interactions and their influence on self assembly of large scale porphyrin aggregates. *J. Photochem. Photobiol. Chem.* **151,** 105–119 (2002).
12. Alvarez, M. G., Príncipe, F., Milanesio, M. E., Durantini, E. N. & Rivarola, V. Photodynamic damages induced by a monocationic porphyrin derivative in a human carcinoma cell line. *Int. J. Biochem. Cell Biol.* **37,** 2504–2512 (2005).
13. Berg, J. M., Stryer, L. & Tymoczko, J. L. *Stryer Biochemie*. (Springer Spektrum, 2012).
14. Huber, R. A structural basis of light energy and electron transfer in biology. *Eur. J. Biochem.* **187,** 283–305 (1990).
15. Phillips, S. E. Structure and refinement of oxymyoglobin at 1.6 A resolution. *J.Mol.Biol.* **142,** 531–554 (1981).
16. Hasnain, S. S. & Hodgson, K. O. Structure of metal centres in proteins at subatomic resolution. *J. Synchrotron Radiat.* **6,** 852–864 (1999).
17. Perutz, M. F. Myoglobin and haemoglobin: role of distal residues in reactions with haem ligands. *Trends Biochem. Sci.* **14,** 42–44 (1989).
18. Kendrew, J. C. *et al.* A Three-Dimensional Model of the Myoglobin Molecule Obtained by X-Ray Analysis. *Nature* **181,** 662–666 (1958).
19. The Nobel Prize in Chemistry 1962. (2015). at <http://www.nobelprize.org/nobel_prizes/chemistry/laureates/1962/>
20. Horton, H. R., Moran, L. A., Scrimgeour, K. G., Perry, M. D. & Rawn, J. D. *Biochemie*. (Pearson Studium, 2008).
21. Aronoff, S. Perchloric. Acid Titrations of Porphyrins in Nitrobenzene. *J. Phys. Chem.* **62,** 428–431 (1958).
22. Becker, E. D. & Bradley, R. B. Effects of ``Ring Currents'' on the NMR Spectra of Porphyrins. *J. Chem. Phys.* **31,** 1413–1414 (1959).
23. JANSON, T. R. & KATZ, J. J. in *The Porphyrins* (ed. DOLPHIN, D.) 1–59 (Academic Press, 1979). at <http://www.sciencedirect.com/science/article/pii/B9780122201042500089>

24. Hoard, J. L. Stereochemistry of Hemes and Other Metalloporphyrins. *Science* **174,** 1295–1302 (1971).
25. Woodward, R. B. Totalsynthese des Chlorophylls. *Angew. Chem.* **72,** 651–662 (1960).
26. Woodward, R. B. *et al.* THE TOTAL SYNTHESIS OF CHLOROPHYLL. *J. Am. Chem. Soc.* **82,** 3800–3802 (1960).
27. Takeda, J. & Sato, M. Effect of Ring Distortion upon Redox Potentials of Metalloporphyrins: Electrochemical Studies of Metallododecaphenylporphyrins. *Chem. Lett.* **24,** 939–940 (1995).
28. Barkigia, K. M. *et al.* Nonplanar porphyrins. X-ray structures of (2,3,7,8,12,13,17,18-octaethyl- and -octamethyl-5,10,15,20-tetraphenylporphinato)zinc(II). *J. Am. Chem. Soc.* **112,** 8851–8857 (1990).
29. Winter, B. & Faubel, M. Photoemission from Liquid Aqueous Solutions. *Chem. Rev.* **106,** 1176–1211 (2006).
30. Winter, B. Liquid microjet for photoelectron spectroscopy. *Nucl. Instrum. Methods Phys. Res. Sect. Accel. Spectrometers Detect. Assoc. Equip.* **601,** 139–150 (2009).
31. Lange, K. M. *et al.* High resolution X-ray emission spectroscopy of water and aqueous ions using the micro-jet technique. *Chem. Phys.* **377,** 1–5 (2010).
32. Gotz, M. D. *et al.* Probing Coster–Kronig Transitions in Aqueous Fe2+ Solution Using Inverse Partial and Partial Fluorescence Yield at the L-Edge. *J. Phys. Chem. Lett.* **3,** 1619–1623 (2012).
33. Casci, J. L., Lok, C. M. & Shannon, M. D. Fischer–Tropsch catalysis: The basis for an emerging industry with origins in the early 20th Century. *Catal. Today* **145,** 38–44 (2009).
34. Gärtner, F. *et al.* Light-Driven Hydrogen Generation: Efficient Iron-Based Water Reduction Catalysts. *Angew. Chem. Int. Ed.* **48,** 9962–9965 (2009).
35. Thomson, A. J. & Gray, H. B. Bio-inorganic chemistry. *Curr. Opin. Chem. Biol.* **2,** 155–158 (1998).
36. Wasserscheid, P. & Keim, W. Ionic Liquids—New 'Solutions' for Transition Metal Catalysis. *Angew. Chem. Int. Ed.* **39,** 3772–3789 (2000).
37. Ashcroft, A. T. *et al.* Selective oxidation of methane to synthesis gas using transition metal catalysts. *Nature* **344,** 319–321 (1990).
38. Ikariya, T. & Blacker, A. J. Asymmetric Transfer Hydrogenation of Ketones with Bifunctional Transition Metal-Based Molecular Catalysts †. *Acc. Chem. Res.* **40,** 1300–1308 (2007).
39. Marcus, Y. Effect of Ions on the Structure of Water: Structure Making and Breaking. *Chem. Rev.* **109,** 1346–1370 (2009).
40. Charkin, O. P., Klimenko, N. M., Charkin, D. O., Chang, H.-C. & Lin, S.-H. Theoretical DFT Study of Fragmentation and Association of Heme and Hemin†. *J. Phys. Chem. A* **111,** 9207–9217 (2007).
41. Aziz, E. F. *et al.* Probing the Electronic Structure of the Hemoglobin Active Center in Physiological Solutions. *Phys. Rev. Lett.* **102,** 068103 (2009).
42. Bergmann, N. *et al.* On the enzymatic activity of catalase: an iron L-edge X-ray absorption study of the active centre. *Phys. Chem. Chem. Phys.* **12,** 4827–4832 (2010).
43. Vzorov, A. N., Dixon, D. W., Trommel, J. S., Marzilli, L. G. & Compans, R. W. Inactivation of Human Immunodeficiency Virus Type 1 by Porphyrins. *Antimicrob. Agents Chemother.* **46,** 3917–3925 (2002).
44. Koenig, D. F. The structure of α-chlorohemin. *Acta Crystallogr.* **18,** 663–673 (1965).
45. Suchkova, S. A., Soldatov, A., Dziedzik-Kocurek, K. & Stillman, M. J. The role of spin state on the local atomic and electronic structures of some metalloporphyrin complexes. *J. Phys. Conf. Ser.* **190,** 012211 (2009).
46. Gütlich, P., Gaspar, A. B. & Garcia, Y. Spin state switching in iron coordination compounds. *Beilstein J. Org. Chem.* **9,** 342–391 (2013).
47. Harada, Y. *et al.* Ligand Energy Controls the Heme-Fe Valence in Aqueous Myoglobins. *J. Phys. Soc. Jpn.* **78,** 044802 (2009).
48. Aziz, E. F., Ottosson, N., Faubel, M., Hertel, I. V. & Winter, B. Interaction between liquid water and hydroxide revealed by core-hole de-excitation. *Nature* **455,** 89–91 (2008).

49. Mitzner, R. *et al.* L-Edge X-ray Absorption Spectroscopy of Dilute Systems Relevant to Metalloproteins Using an X-ray Free-Electron Laser. *J. Phys. Chem. Lett.* **4,** 3641–3647 (2013).

50. Suljoti, E. *et al.* Direct Observation of Molecular Orbital Mixing in a Solvated Organometallic Complex. *Angew. Chem. Int. Ed.* **52,** 9841–9844 (2013).

51. Hocking, R. K. *et al.* Fe L-Edge X-ray Absorption Spectroscopy of Low-Spin Heme Relative to Non-heme Fe Complexes: Delocalization of Fe d-Electrons into the Porphyrin Ligand. *J. Am. Chem. Soc.* **129,** 113–125 (2007).

52. Wilson, S. A. *et al.* Iron L-Edge X-ray Absorption Spectroscopy of Oxy-Picket Fence Porphyrin: Experimental Insight into Fe–O2 Bonding. *J. Am. Chem. Soc.* **135,** 1124–1136 (2013).

53. Krasnikov, S. A. *et al.* Electronic structure of Ni(II) porphyrins and phthalocyanine studied by soft X-ray absorption spectroscopy. *Chem. Phys.* **332,** 318–324 (2007).

54. Xiao, J. *et al.* Assistance of the Iron Porphyrin Ligands to the Binding Interaction between the Fe Center and Small Molecules in Solution. *J. Phys. Chem. B* **118,** 9371–9377 (2014).

55. Boucher, L. J. Manganese porphyrin complexes. *Coord. Chem. Rev.* **7,** 289–329 (1972).

56. Oyaizu, K., Haryono, A., Yonemaru, H. & Tsuchida, E. Catalytic behavior of a μ-oxo dimanganese(III) octaethylporphyrin in O2 reduction. *J. Chem. Soc. Faraday Trans.* **94,** 3393–3399 (1998).

57. Elemans, J. A. A. W., Bijsterveld, E. J. A., Rowan, A. E. & Nolte, R. J. M. Manganese Porphyrin Hosts as Epoxidation Catalysts – Activity and Stability Control by Axial Ligand Effects. *Eur. J. Org. Chem.* **2007,** 751–757 (2007).

58. Pratviel, G., Pitié, M., Bernadou, J. & Meunier, B. Mechanism of DNA cleavage by cationic manganese porphyrins: hydroxylations at the 1'-carbon and 5'-carbon atoms of deoxyriboses as initial damages. *Nucleic Acids Res.* **19,** 6283–6288 (1991).

59. Bernadou, J., Pratviel, G., Bennis, F., Girardet, M. & Meunier, B. Potassium monopersulfate and a water-soluble manganese porphyrin complex, [Mn(TMPyP)](OAc)5, as an efficient reagent for the oxidative cleavage of DNA. *Biochemistry (Mosc.)* **28,** 7268–7275 (1989).

60. Pitie, M., Bernadou, J. & Meunier, B. Oxidation at Carbon-1' of DNA Deoxyriboses by the Mn-TMPyP/KHSO5 System Results from a Cytochrome P-450-type Hydroxylation Reaction. *J. Am. Chem. Soc.* **117,** 2935–2936 (1995).

61. Meunier, B. Metalloporphyrins as versatile catalysts for oxidation reactions and oxidative DNA cleavage. *Chem. Rev.* **92,** 1411–1456 (1992).

62. Konarev, D. V., Khasanov, S. S., Saito, G. & Lyubovskaya, R. N. Design of Molecular and Ionic Complexes of Fullerene C60 with Metal(II) Octaethylporphyrins, MIIOEP (M = Zn, Co, Fe, and Mn) Containing Coordination M−N(ligand) and M−C(C60−) Bonds. (--). at <http://pubs.acs.org/doi/abs/10.1021/cg8010184@proofing>

63. Klein, A. T. J., Rösch, F., Coenen, H. H. & Qaim, S. M. Labelling of manganese-based magnetic resonance imaging (MRI) contrast agents with the positron emitter 51Mn, as exemplified by manganese-tetraphenyl-porphin-sulfonate (MnTPPS4). *Appl. Radiat. Isot.* **62,** 711–720 (2005).

64. Gozet, T., Huynh, L. & Bohme, D. K. Collision-induced dissociation of tetraphenyl iron and manganese porphyrin ions by electrospray ionization mass spectrometry. *Int. J. Mass Spectrom.* **279,** 113–118 (2009).

65. Gardner, P. R., Nguyen, D.-D. H. & White, C. W. Superoxide Scavenging by Mn(II/III) Tetrakis (1-Methyl-4-pyridyl) Porphyrin in Mammalian Cells. *Arch. Biochem. Biophys.* **325,** 20–28 (1996).

66. Willmott, P. *An Introduction to Synchrotron Radiation: Techniques and Applications*. (John Wiley & Sons, 2011).

67. Krause, M. O. Atomic radiative and radiationless yields for K and L shells. *J. Phys. Chem. Ref. Data* **8,** 307–327 (1979).

68. Chantler, C. T. Detailed Tabulation of Atomic Form Factors, Photoelectric Absorption and Scattering Cross Section, and Mass Attenuation Coefficients in the Vicinity of Absorption Edges in the Soft X-

Ray (Z=30–36, Z=60–89, E=0.1 keV–10 keV), Addressing Convergence Issues of Earlier Work. *J. Phys. Chem. Ref. Data* **29,** 597–1056 (2000).

69. Chantler, C. T. Theoretical Form Factor, Attenuation, and Scattering Tabulation for Z=1–92 from E=1–10 eV to E=0.4–1.0 MeV. *J. Phys. Chem. Ref. Data* **24,** 71–643 (1995).
70. US Department of Commerce, N. NIST X-Ray Form Factor, Atten., and Scattering Database. at <http://www.nist.gov/pml/data/ffast/index.cfm>
71. Bunker, G. *Introduction to XAFS: A Practical Guide to X-ray Absorption Fine Structure Spectroscopy*. (Cambridge University Press, 2010).
72. Als-Nielsen, J. *Elements of Modern X-ray Physics, 2nd Edition*. (Wiley, 2011).
73. Thompson, A. C. & Vaughan, D. X-Ray Data Booklet. (2001). at <http://xdb.lbl.gov/>
74. Attwood, D. *Soft X-Rays and Extreme Ultraviolet Radiation: Principles and Applications*. (Cambridge University Press, 2007).
75. Jaklevic, J. *et al.* Fluorescence detection of exafs: Sensitivity enhancement for dilute species and thin films. *Solid State Commun.* **23,** 679–682 (1977).
76. Krol, A. *et al.* X-ray-absorption studies of Y-Ba-Cu-O and Bi-Sr-Ca-Cu-O films at oxygen K edge by means of fluorescence and total electron yield: A comparison of two techniques. *Phys. Rev. B* **42,** 2635–2638 (1990).
77. Achkar, A. J. *et al.* Bulk sensitive x-ray absorption spectroscopy free of self-absorption effects. *Phys. Rev. B* **83,** 081106 (2011).
78. Duda, L.-C., Schmitt, T., Augustsson, A. & Nordgren, J. Resonant soft X-ray emission of solids and liquids. *J. Alloys Compd.* **362,** 116–123 (2004).
79. Kotani, A. Resonant inelastic X-ray scattering in d and f electron systems. *Eur. Phys. J. B - Condens. Matter Complex Syst.* **47,** 3–27 (2005).
80. Kramers, H. A. & Heisenberg, W. Über die Streuung von Strahlung durch Atome. *Z. Für Phys.* **31,** 681–708 (1925).
81. Rubensson, J.-E., Lüning, J., Eisebitt, S. & Eberhardt, W. It's always a one-step process. *Appl. Phys. A* **65,** 91–96 (1997).
82. Hüfner, S. *Photoelectron Spectroscopy: Principles and Applications*. (Springer Science & Business Media, 2003).
83. de Groot, F. M. F. & Kotani, A. *Core Level Spectroscopy of Solids*. (Crc Pr Inc, 2008).
84. Fano, U. Effects of Configuration Interaction on Intensities and Phase Shifts. *Phys. Rev.* **124,** 1866–1878 (1961).
85. Brown, M. A., Faubel, M. & Winter, B. X-Ray photo- and resonant Auger-electron spectroscopy studies of liquid water and aqueous solutions. *Annu. Rep. Sect. C Phys. Chem.* **105,** 174–212 (2009).
86. Seidel, R. Electronic-Structure Interactions in Aqueous Solutions: A Liquid-Jet Photoelectron-Spectroscopy Study. (Technische Universität Berlin, Germany, 2011).
87. Hergenhahn, U. Interatomic and intermolecular coulombic decay: The early years. *J. Electron Spectrosc. Relat. Phenom.* **184,** 78–90 (2011).
88. Schwartz, C. P., Fatehi, S., Saykally, R. J. & Prendergast, D. Importance of Electronic Relaxation for Inter-Coulombic Decay in Aqueous Systems. *Phys. Rev. Lett.* **105,** 198102 (2010).
89. Schwinger, J. On the Classical Radiation of Accelerated Electrons. *Phys. Rev.* **75,** 1912–1925 (1949).
90. Lange, K. M. Structure and dynamics of water and ions in solution. (Freie Universität Berlin, Germany, 2012).
91. Jung, C. *et al.* First results of the soft X-ray microfocus beamline U41-PGM. *Nucl. Instrum. Methods Phys. Res. Sect. Accel. Spectrometers Detect. Assoc. Equip.* **467–468, Part 1,** 485–487 (2001).
92. Jung, C. *et al.* U41-PGM: commissioning results.

93. Rowland, H. A. XXIX. On concave gratings for optical purposes. *Philos. Mag. Ser. 5* **16,** 197–210 (1883).

94. Born, M. *et al. Principles of Optics: Electromagnetic Theory of Propagation, Interference and Diffraction of Light*. (Cambridge University Press, 1999).

95. Peatman, W. B. & Peatman, W. B. *Gratings, Mirrors and Slits: Beamline Design for Soft X-Ray Synchrotron Radiation Sources*. (Crc Press, 1997).

96. Gotz, M. Electronic Structure in Solution. Soft X-ray Absorption and Emission for Fe2+ in Water. (Freie Universität Berlin, Germany, 2012).

97. Bergmann, L., Schaefer, C. & Kleinermanns, K. *Ludwig Bergmann; Clemens Schaefer: Lehrbuch der Experimentalphysik: Lehrbuch der Experimentalphysik: Lehrbuch der Experimentalphysik 5. Gase, ... Lehrbuch Der Experimentalphysik): Band 5*. (Gruyter, 2005).

98. Faubel, M., Schlemmer, S. & Toennies, J. P. A molecular beam study of the evaporation of water from a liquid jet. *Z. Für Phys. At. Mol. Clust.* **10,** 269–277 (1988).

99. Faubel, M. & Kisters, T. Non-equilibrium molecular evaporation of carboxylic acid dimers. *Nature* **339,** 527–529 (1989).

100. Weber, C. Zum Zerfall eines Flüssigkeitsstrahles. *ZAMM - J. Appl. Math. Mech. Z. Für Angew. Math. Mech.* **11,** 136–154 (1931).

101. Haenlein, A. Über den Zerfall eines Flüssigkeitsstrahles. *Forsch. Auf Dem Geb. Ingenieurwesens A* **2,** 139–149 (1931).

102. Microliquids GmbH Advanced micro jet technologies for science and industry - Microliquids GmbH. (2015). at <http://www.microliquids.com/>

103. Guo, J.-H. *et al.* X-Ray Emission Spectroscopy of Hydrogen Bonding and Electronic Structure of Liquid Water. *Phys. Rev. Lett.* **89,** 137402 (2002).

104. Heske, C. *et al.* Monitoring chemical reactions at a liquid–solid interface: Water on CuIn(S,Se)2 thin film solar cell absorbers. *J. Chem. Phys.* **119,** 10467–10470 (2003).

105. Odelius, M. *et al.* Ultrafast Core-Hole-Induced Dynamics in Water Probed by X-Ray Emission Spectroscopy. *Phys. Rev. Lett.* **94,** 227401 (2005).

106. Fuchs, O. *et al.* A liquid flow cell to study the electronic structure of liquids with soft X-rays. *Nucl. Instrum. Methods Phys. Res. Sect. Accel. Spectrometers Detect. Assoc. Equip.* **585,** 172–177 (2008).

107. Henke, B. L., Gullikson, E. M. & Davis, J. C. X-Ray Interactions: Photoabsorption, Scattering, Transmission, and Reflection at E = 50-30,000 eV, Z = 1-92. *At. Data Nucl. Data Tables* **54,** 181–342 (1993).

108. Heinrich, C. A. & Seward, T. M. A spectrophotometric study of aqueous iron (II) chloride complexing from 25 to 200°C. *Geochim. Cosmochim. Acta* **54,** 2207–2221 (1990).

109. Apted, M. J., Waychunas, G. A. & Brown, G. E. Structure and specification of iron complexes in aqueous solutions determined by X-ray absorption spectroscopy. *Geochim. Cosmochim. Acta* **49,** 2081–2089 (1985).

110. Tokushima, T. *et al.* Selective observation of the two oxygen atoms at different sites in the carboxyl group (–COOH) of liquid acetic acid. *Phys. Chem. Chem. Phys.* **11,** 1679–1682 (2009).

111. Brown, S. B., Jones, P. & Lantzke, I. R. Infrared Evidence for an Oxo-bridged (Fe-O-Fe) Haemin Dimer. *Nature* **223,** 960–961 (1969).

112. Collier, G. S., Pratt, J. M., Wet, C. R. D. & Tshabalala, C. F. Studies on haemin in dimethyl sulphoxide/water mixtures. *Biochem. J.* **179,** 281–289 (1979).

113. Soldatov, M. A. *et al.* On the origin of dips in total fluorescence yield X-ray absorption spectra: Partial and inverse partial fluorescence yield at the L-edge of cobalt aqueous solution. *Chem. Phys. Lett.* **546,** 164–167 (2012).

114. Golnak, R. *et al.* Local electronic structure of aqueous zinc acetate: oxygen K-edge X-ray absorption and emission spectroscopy on micro-jets. *Phys. Chem. Chem. Phys.* **15,** 8046–8049 (2013).

115. Neese, F. The ORCA program system. *Wiley Interdiscip. Rev. Comput. Mol. Sci.* **2,** 73–78 (2012).

116. Becke, A. D. Density-functional exchange-energy approximation with correct asymptotic behavior. *Phys. Rev. A* **38,** 3098–3100 (1988).

117. Becke, A. D. Density-functional thermochemistry. III. The role of exact exchange. *J. Chem. Phys.* **98,** 5648–5652 (1993).

118. Weigend, F. & Ahlrichs, R. Balanced basis sets of split valence, triple zeta valence and quadruple zeta valence quality for H to Rn: Design and assessment of accuracy. *Phys. Chem. Chem. Phys.* **7,** 3297–3305 (2005).

119. Roemelt, M., Maganas, D., DeBeer, S. & Neese, F. A combined DFT and restricted open-shell configuration interaction method including spin-orbit coupling: Application to transition metal L-edge X-ray absorption spectroscopy. *J. Chem. Phys.* **138,** 204101 (2013).

120. Vahtras, O., Almlöf, J. & Feyereisen, M. W. Integral approximations for LCAO-SCF calculations. *Chem. Phys. Lett.* **213,** 514–518 (1993).

121. Eichkorn, K., Treutler, O., Öhm, H., Häser, M. & Ahlrichs, R. Auxiliary basis sets to approximate Coulomb potentials (Chem. Phys. Letters 240 (1995) 283-290). *Chem. Phys. Lett.* **242,** 652–660 (1995).

122. Eichkorn, K., Weigend, F., Treutler, O. & Ahlrichs, R. Auxiliary basis sets for main row atoms and transition metals and their use to approximate Coulomb potentials. *Theor. Chem. Acc.* **97,** 119–124 (1997).

123. Weigend, F. Accurate Coulomb-fitting basis sets for H to Rn. *Phys. Chem. Chem. Phys.* **8,** 1057–1065 (2006).

124. Hanwell, M. D. *et al.* Avogadro: an advanced semantic chemical editor, visualization, and analysis platform. *J. Cheminformatics* **4,** 17 (2012).

125. Karlström, G. *et al.* MOLCAS: a program package for computational chemistry. *Comput. Mater. Sci.* **28,** 222–239 (2003).

126. Malmqvist, P. A., Rendell, A. & Roos, B. O. The restricted active space self-consistent-field method, implemented with a split graph unitary group approach. *J. Phys. Chem.* **94,** 5477–5482 (1990).

127. Roos, B. O., Lindh, R., Malmqvist, P.-Å., Veryazov, V. & Widmark, P.-O. Main Group Atoms and Dimers Studied with a New Relativistic ANO Basis Set. *J. Phys. Chem. A* **108,** 2851–2858 (2004).

128. Roos, B. O., Lindh, R., Malmqvist, P.-Å., Veryazov, V. & Widmark, P.-O. New Relativistic ANO Basis Sets for Transition Metal Atoms. *J. Phys. Chem. A* **109,** 6575–6579 (2005).

129. Malmqvist, P. Å., Roos, B. O. & Schimmelpfennig, B. The restricted active space (RAS) state interaction approach with spin–orbit coupling. *Chem. Phys. Lett.* **357,** 230–240 (2002).

130. Bokarev, S. I. *et al.* Unraveling the Electronic Structure of Photocatalytic Manganese Complexes by L-Edge X-ray Spectroscopy. *J. Phys. Chem. C* **119,** 19192–19200 (2015).

131. Grell, G. *et al.* Multi-reference approach to the calculation of photoelectron spectra including spin-orbit coupling. *J. Chem. Phys.* **143,** 074104 (2015).

132. Baerends, E. J., Ellis, D. E. & Ros, P. Self-consistent molecular Hartree Fock Slater calculations I. The computational procedure. *Chem. Phys.* **2,** 41–51 (1973).

133. Dunlap, B. I., Connolly, J. W. D. & Sabin, J. R. On some approximations in applications of Xα theory. *J. Chem. Phys.* **71,** 3396–3402 (1979).

134. Stöhr, J. *NEXAFS Spectroscopy*. (Springer, 2003).

135. Gudat, W. & Kunz, C. Close Similarity between Photoelectric Yield and Photoabsorption Spectra in the Soft-X-Ray Range. *Phys. Rev. Lett.* **29,** 169–172 (1972).

136. Achkar, A. J., Regier, T. Z., Monkman, E. J., Shen, K. M. & Hawthorn, D. G. Determination of total x-ray absorption coefficient using non-resonant x-ray emission. *Sci. Rep.* **1,** 182 (2011).

137. Eisebitt, S., Böske, T., Rubensson, J.-E. & Eberhardt, W. Determination of absorption coefficients for concentrated samples by fluorescence detection. *Phys. Rev. B* **47,** 14103–14109 (1993).

138. Błachucki, W. *et al.* High Energy Resolution Off-Resonant Spectroscopy for X-Ray Absorption Spectra Free of Self-Absorption Effects. *Phys. Rev. Lett.* **112,** 173003 (2014).

139. Tröger, L. *et al.* Full correction of the self-absorption in soft-fluorescence extended x-ray-absorption fine structure. *Phys. Rev. B* **46,** 3283–3289 (1992).

140. de Groot, F. M. F. Dips and peaks in fluorescence yield X-ray absorption are due to state-dependent decay. *Nat. Chem.* **4,** 766–767 (2012).

141. Nakajima, R., Stöhr, J. & Idzerda, Y. U. Electron-yield saturation effects in L-edge x-ray magnetic circular dichroism spectra of Fe, Co, and Ni. *Phys. Rev. B* **59,** 6421–6429 (1999).

142. Bokarev, S. I., Dantz, M., Suljoti, E., Kühn, O. & Aziz, E. F. State-Dependent Electron Delocalization Dynamics at the Solute-Solvent Interface: Soft-X-Ray Absorption Spectroscopy and ab Initio Calculations. *Phys. Rev. Lett.* **111,** 083002 (2013).

143. Föhlisch, A., de Groot, F. M. F., Odelius, M., Techert, S. & Wernet, P. Comment on ``State-Dependent Electron Delocalization Dynamics at the Solute-Solvent Interface: Soft-X-ray Absorption Spectroscopy and Ab Initio Calculations''. *Phys. Rev. Lett.* **112,** 129302 (2014).

144. Green, R. J. *et al.* Comment on ``State-Dependent Electron Delocalization Dynamics at the Solute-Solvent Interface: Soft-X-Ray Absorption Spectroscopy and Ab initio Calculations''. *Phys. Rev. Lett.* **112,** 129301 (2014).

145. Bokarev, S. I. *et al.* Bokarev et al. Reply. *Phys. Rev. Lett.* **112,** 129303 (2014).

146. Atak, K. *et al.* Nature of the Chemical Bond of Aqueous Fe2+ Probed by Soft X-ray Spectroscopies and ab Initio Calculations. *J. Phys. Chem. B* **117,** 12613–12618 (2013).

147. Stöhr, J. EXAFS and surface-EXAFS studies in the soft x-ray region using electron yield spectroscopy. *J. Vac. Sci. Technol.* **16,** 37–41 (1979).

148. Thürmer, S., Seidel, R., Eberhardt, W., Bradforth, S. E. & Winter, B. Ultrafast Hybridization Screening in Fe3+ Aqueous Solution. *J. Am. Chem. Soc.* **133,** 12528–12535 (2011).

149. Seidel, R. *et al.* Valence Photoemission Spectra of Aqueous Fe2+/3+ and [Fe(CN)6]4–/3– and Their Interpretation by DFT Calculations. *J. Phys. Chem. B* **115,** 11671–11677 (2011).

150. Aziz, E. F., Rittmann-Frank, M. H., Lange, K. M., Bonhommeau, S. & Chergui, M. Charge transfer to solvent identified using dark channel fluorescence-yield L-edge spectroscopy. *Nat. Chem.* **2,** 853–857 (2010).

151. Vlachos, D., Craven, A. J. & McComb, D. W. Specimen charging in X-ray absorption spectroscopy: correction of total electron yield data from stabilized zirconia in the energy range 250–915 eV. *J. Synchrotron Radiat.* **12,** 224–233 (2005).

152. Kotani, A. & Shin, S. Resonant inelastic x-ray scattering spectra for electrons in solids. *Rev. Mod. Phys.* **73,** 203–246 (2001).

153. Freiwald, M., Cramm, S., Eberhardt, W. & Eisebitt, S. Soft X-ray absorption spectroscopy in liquid environments. *J. Electron Spectrosc. Relat. Phenom.* **137–140,** 413–416 (2004).

154. Nagasaka, M., Hatsui, T., Horigome, T., Hamamura, Y. & Kosugi, N. Development of a liquid flow cell to measure soft X-ray absorption in transmission mode: A test for liquid water. *J. Electron Spectrosc. Relat. Phenom.* **177,** 130–134 (2010).

155. Aziz, E. F. The solvation of ions and molecules probed via soft X-ray spectroscopies. *J. Electron Spectrosc. Relat. Phenom.* **177,** 168–180 (2010).

156. Seidel, R. *et al.* Origin of Dark-Channel X-ray Fluorescence from Transition-Metal Ions in Water. *J. Am. Chem. Soc.* **134,** 1600–1605 (2012).

157. Siegbahn, H. & Siegbahn, K. ESCA applied to liquids. *J. Electron Spectrosc. Relat. Phenom.* **2,** 319–325 (1973).

158. Faubel, M., Steiner, B. & Toennies, J. P. Photoelectron spectroscopy of liquid water, some alcohols, and pure nonane in free micro jets. *J. Chem. Phys.* **106,** 9013–9031 (1997).

159. Lange, K. M., Kothe, A. & Aziz, E. F. Chemistry in solution: recent techniques and applications using soft X-ray spectroscopy. *Phys. Chem. Chem. Phys.* **14,** 5331–5338 (2012).

160. Wilson, K. R. *et al.* X-ray Spectroscopy of Liquid Water Microjets. *J. Phys. Chem. B* **105,** 3346–3349 (2001).

161. Regier, T. Z., Achkar, A. J., Peak, D., Tse, J. S. & Hawthorn, D. G. Dark channel fluorescence observations result from concentration effects rather than solvent-solute charge transfer. *Nat. Chem.* **4,** 765–766 (2012).

162. Luo, Y., Ågren, H. & Gel'mukhanov, F. Polarization anisotropy in resonant x-ray emission from molecules. *Phys. Rev. A* **53,** 1340–1348 (1996).

163. de Groot, F. M. F., Arrio, M. A., Sainctavit, P., Cartier, C. & Chen, C. T. Fluorescence yield detection: Why it does not measure the X-ray absorption cross section. *Solid State Commun.* **92,** 991–995 (1994).

164. Kurian, R. *et al.* Intrinsic deviations in fluorescence yield detected x-ray absorption spectroscopy: the case of the transition metal L 2,3 edges. *J. Phys. Condens. Matter* **24,** 452201 (2012).

165. Kuleff, A. I. & Cederbaum, L. S. Radiation Generated by the Ultrafast Migration of a Positive Charge Following the Ionization of a Molecular System. *Phys. Rev. Lett.* **106,** 053001 (2011).

166. Thürmer, S. *et al.* On the nature and origin of dicationic, charge-separated species formed in liquid water on X-ray irradiation. *Nat. Chem.* **5,** 590–596 (2013).

167. Kurahashi, N. *et al.* Photoelectron spectroscopy of aqueous solutions: Streaming potentials of NaX (X = Cl, Br, and I) solutions and electron binding energies of liquid water and X−. *J. Chem. Phys.* **140,** 174506 (2014).

168. Winter, B. *et al.* Electron Binding Energies of Aqueous Alkali and Halide Ions: EUV Photoelectron Spectroscopy of Liquid Solutions and Combined Ab Initio and Molecular Dynamics Calculations. *J. Am. Chem. Soc.* **127,** 7203–7214 (2005).

169. Gottfried, J. M., Flechtner, K., Kretschmann, A., Lukasczyk, T. & Steinrück, H.-P. Direct Synthesis of a Metalloporphyrin Complex on a Surface. *J. Am. Chem. Soc.* **128,** 5644–5645 (2006).

170. Shubina, T. E. *et al.* Principle and Mechanism of Direct Porphyrin Metalation: Joint Experimental and Theoretical Investigation. *J. Am. Chem. Soc.* **129,** 9476–9483 (2007).

171. Maines, M. D. & Kappas, A. Enzymic oxidation of cobalt protoporphyrin IX: observations on the mechanism of heme oxygenase action. *Biochemistry (Mosc.)* **16,** 419–423 (1977).

172. Smith, A., Alam, J., Escriba, P. V. & Morgan, W. T. Regulation of heme oxygenase and metallothionein gene expression by the heme analogs, cobalt-, and tin-protoporphyrin. *J. Biol. Chem.* **268,** 7365–7371 (1993).

173. Adams, P. A., Baldwin, D. A., Hepner, C. E. & Pratt, J. M. Coordination of imidazole by hemin in organic and aqueous organic solvents. *Bioinorg. Chem.* **9,** 479–494 (1978).

174. Jensen, F. *Introduction to Computational Chemistry: Second Edition*. (JW, 2011).

175. Nordgren, J. & Rubensson, J.-E. Resonant soft X-ray emission for studies of molecules and solids. *J. Electron Spectrosc. Relat. Phenom.* **188,** 3–9 (2013).

176. Gel'mukhanov, F. & Ågren, H. Resonant X-ray Raman scattering. *Phys. Rep.* **312,** 87–330 (1999).

177. Roemelt, M. & Neese, F. Excited States of Large Open-Shell Molecules: An Efficient, General, and Spin-Adapted Approach Based on a Restricted Open-Shell Ground State Wave function. *J. Phys. Chem. A* **117,** 3069–3083 (2013).

178. Atak, K. *et al.* Electronic Structure of Hemin in Solution Studied by Resonant X-ray Emission Spectroscopy and Electronic Structure Calculations. *J. Phys. Chem. B* **118,** 9938–9943 (2014).

179. Lewis, D. F. V. *Guide to Cytochromes: Structure and Function*. (CRC Press, 1996).

180. Golnak, R. *et al.* Local Energy Gap Opening Induced by Hemin Dimerization in Aqueous Solution. *J. Phys. Chem. B* **119,** 3058–3062 (2015).

181. Maehly, A. C. *et al.* Stabilization of Aqueous Hemin Solutions. *Acta Chem Scand* **12,** 1259–1273 (1958).

182. Villiers, K. A. de, Kaschula, C. H., Egan, T. J. & Marques, H. M. Speciation and structure of ferriprotoporphyrin IX in aqueous solution: spectroscopic and diffusion measurements demonstrate dimerization, but not μ-oxo dimer formation. *JBIC J. Biol. Inorg. Chem.* **12,** 101–117 (2006).

183. Aziz, E. F. X-ray Spectroscopies Revealing the Structure and Dynamics of Metalloprotein Active Centers. *J. Phys. Chem. Lett.* **2,** 320–326 (2011).

184. Lange, K. M. & Aziz, E. F. Electronic structure of ions and molecules in solution: a view from modern soft X-ray spectroscopies. *Chem. Soc. Rev.* **42,** 6840–6859 (2013).

185. Stevens, J. S. *et al.* Chemical Speciation and Bond Lengths of Organic Solutes by Core-Level Spectroscopy: pH and Solvent Influence on p-Aminobenzoic Acid. *Chem. – Eur. J.* **21,** 7256–7263 (2015).

186. de Groot, F. High-Resolution X-ray Emission and X-ray Absorption Spectroscopy. *Chem. Rev.* **101,** 1779–1808 (2001).

187. Röckert, M. *et al.* Abrupt Coverage-Induced Enhancement of the Self-Metalation of Tetraphenylporphyrin with Cu(111). *J. Phys. Chem. C* **118,** 1661–1667 (2014).

188. Nardi, M. V. *et al.* XAS of tetrakis(phenyl)- and tetrakis(pentafluorophenyl)-porphyrin: an experimental and theoretical study. *Phys. Chem. Chem. Phys.* **17,** 2001–2011 (2014).

189. Schmidt, N., Fink, R. & Hieringer, W. Assignment of near-edge x-ray absorption fine structure spectra of metalloporphyrins by means of time-dependent density-functional calculations. *J. Chem. Phys.* **133,** 054703 (2010).

190. Stevens, J. S. *et al.* Incisive Probing of Intermolecular Interactions in Molecular Crystals: Core Level Spectroscopy Combined with Density Functional Theory. *J. Phys. Chem. B* **118,** 12121–12129 (2014).

191. Thomason, M. J. *et al.* Self-association of organic solutes in solution: a NEXAFS study of aqueous imidazole. *Faraday Discuss.* **179,** 269–289 (2015).

192. Xiao, J. & Dowben, P. A. Changes in the adsorbate dipole layer with changing d-filling of the metal (II) (Co, Ni, Cu) phthalocyanines on Au(111). *J. Phys. Condens. Matter* **21,** 052001 (2009).

193. Xiao, J. & Dowben, P. A. The role of the interface in the electronic structure of adsorbed metal(II) (Co, Ni, Cu) phthalocyanines. *J. Mater. Chem.* **19,** 2172–2178 (2009).

194. Freund, H.-J. & Neumann, M. Photoemission of molecular adsorbates. *Appl. Phys. A* **47,** 3–23 (1988).

195. Stevens, J. S. *et al.* Proton Transfer, Hydrogen Bonding, and Disorder: Nitrogen Near-Edge X-ray Absorption Fine Structure and X-ray Photoelectron Spectroscopy of Bipyridine–Acid Salts and Co-crystals. *Cryst. Growth Des.* **15,** 1776–1783 (2015).

196. Atak, K. *et al.* Co(III) protoporphyrin IX chloride in solution: spin-state and metal coordination revealed from resonant inelastic X-ray scattering and electronic structure calculations. *Phys. Chem. Chem. Phys.* **17,** 3409–3414 (2015).

197. Weinhardt, L. *et al.* RIXS investigations of liquids, solutions, and liquid/solid interfaces. *J. Electron Spectrosc. Relat. Phenom.* **188,** 111–120 (2013).

198. Besora, M. *et al.* A Combined Theoretical and Experimental Study on the Role of Spin States in the Chemistry of Fe(CO)5 Photoproducts. *J. Am. Chem. Soc.* **131,** 3583–3592 (2009).

199. Ghiringhelli, G. *et al.* Resonant inelastic x-ray scattering of MnO: L2,3 edge measurements and assessment of their interpretation. *Phys. Rev. B* **73,** 035111 (2006).

200. Butorin, S. M., Guo, J.-H., Magnuson, M., Kuiper, P. & Nordgren, J. Low-energy d-d excitations in MnO studied by resonant x-ray fluorescence spectroscopy. *Phys. Rev. B* **54,** 4405–4408 (1996).

201. Xiao, J. *et al.* Enhancing Catalytic Activity by Narrowing Local Energy Gaps—X-Ray Studies of a Manganese Water Oxidation Catalyst. *ChemSusChem* **8,** 872–877 (2015).

202. Moulder, J. F., Chastain, J. & King, R. C. *Handbook of x-ray photoelectron spectroscopy: a reference book of standard spectra for identification and interpretation of XPS data*. (Physical Electronics, 1995).

203. Grush, M. M. *et al.* Manganese L-Edge X-ray Absorption Spectroscopy of Manganese Catalase from Lactobacillus plantarum and Mixed Valence Manganese Complexes. *J. Am. Chem. Soc.* **118,** 65–69 (1996).

204. Ament, L. J. P., van Veenendaal, M., Devereaux, T. P., Hill, J. P. & van den Brink, J. Resonant inelastic x-ray scattering studies of elementary excitations. *Rev. Mod. Phys.* **83,** 705–767 (2011).

205. Brandenburg, T. *et al.* Fluorination-dependent molecular orbital occupancy in ring-shaped perfluorocarbons. *Phys. Chem. Chem. Phys.* **17,** 18337–18343 (2015).

206. Engel, N. *et al.* Chemical Bonding in Aqueous Ferrocyanide: Experimental and Theoretical X-ray Spectroscopic Study. *J. Phys. Chem. B* **118,** 1555–1563 (2014).

207. Kotani, M. Electronic Structure of Iron in Porphyrin Complexes*. *Ann. N. Y. Acad. Sci.* **158,** 20–49 (1969).

208. Zypman, F. R. Off-axis electric field of a ring of charge. *Am. J. Phys.* **74,** 295–300 (2006).

209. Springer, B. A., Sligar, S. G., Olson, J. S. & Phillips, G. N. J. Mechanisms of Ligand Recognition in Myoglobin. *Chem. Rev.* **94,** 699–714 (1994).

210. Siefermann, K. R. *et al.* Binding energies, lifetimes and implications of bulk and interface solvated electrons in water. *Nat. Chem.* **2,** 274–279 (2010).

211. Plakhutin, B. N. & Davidson, E. R. Koopmans' Theorem in the Restricted Open-Shell Hartree−Fock Method. 1. A Variational Approach†. *J. Phys. Chem. A* **113,** 12386–12395 (2009).

212. Plakhutin, B. N. & Davidson, E. R. Canonical form of the Hartree-Fock orbitals in open-shell systems. *J. Chem. Phys.* **140,** 014102 (2014).

7 List of Figures

8 Appendix

8.1 Auger-Electron Channels of Aqueous Ferrous Solution

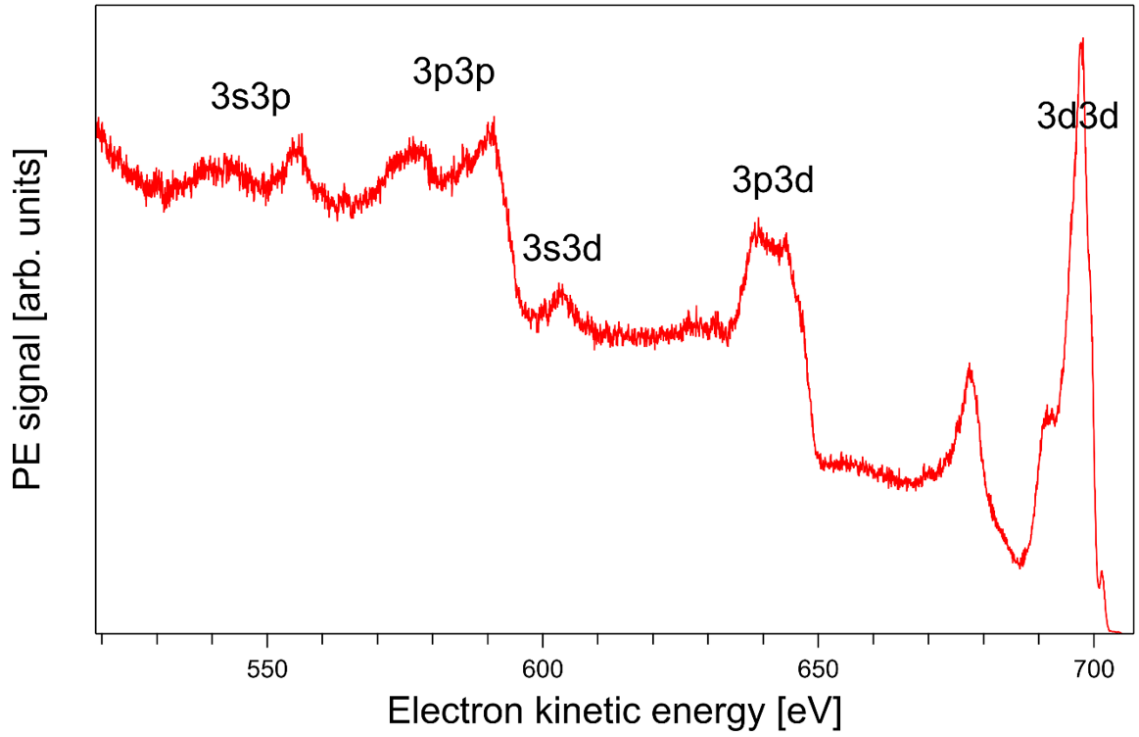

Assignment of the different Auger-electron channels for aqueous solution of 1M $FeCl_2$

8.2 Coordination of Fe in FePPIX-Cl at Different Spin Configurations

During the optimization of the molecular geometries and the subsequent application of DFT/ ROCIS for obtaining the XA spectra, the spin-unrestricted Kohn-Sham (UKS) method (available in the ORCA software) was used due to the open-shell nature of the TM complex under investigation. This leads to a good agreement with the experiment. Yet the interpretation suffers from the unrestricted nature of the method; the orbitals are split into two sets with α and β spin wave functions, with no restriction on the spatial part of the orbitals. This does not present a theoretical problem as individual MOs are not observables, but the spectra are. On the other hand, to be able to interpret the orbitals in the sense of bonding structure or energy levels, the use of one orbital set is more convenient, and can be provided by applying a restricted open-shell Kohn-Sham (ROKS) method. ORCA itself creates a similar set of orbitals called the quasi-restricted orbital set for the DFT/ROCIS part, but ROKS can provide human readable orbital visualizations

and population analyses in a straightforward fashion. However, ROKS calculations are more difficult to perform, during which self-consistent-field (SCF) convergence becomes problematic. Therefore, the spectra for different spin states and conformations using UKS method were calculated. Then the best matching spectrum to the experimental result was selected. In a next step the XAS calculation was repeated for that particular case with ROKS method, and verified the spectrum to be essentially the same. The orbital energies presented by ROKS and the quasi restricted orbital method by DFT/ROCIS are found to be very similar. Unfortunately both of the methods suffer from the same well-known drawback: the violation of the Aufbau principle in determining the energies of the SOMOs [174,211,212]. Therefore, when regarding the MO energies in the following table, it should be kept in mind that, the relative energies between these orbitals should be considered more physical than the absolute values.

	FePPIXCl S=2.5	FePPIXCl S=1.5	FePPIXCl S=0.5
Fe-Cl bond distance [Å]	2.239	2.292	2.236
Fe-N bond distance [Å]	2.101, 2.107, 2.094, 2.103	2.025, 2.032, 2.016, 2.025	2.005, 2.016, 2.010, 2.012
Cl-Fe-N bond angle [°]	106.0, 105.5, 103.0, 103.1	100.2, 100.3, 97.8, 97.9	97.5, 100.8, 94.6, 96.9
N-Fe-N bond angle [°]	86.4, 86.7, 86.1, 86.6	88.5, 88.8, 88.3, 88.8	89.0, 89.4, 88.3, 89.6
Total dipole moment [Debye]	4.14	4.85	3.92
Total single point energy [eV]	-96826.98	-96826.90	-96826.38
	FePPIX S=2.5	FePPIX S=1.5	FePPIX S=0.5
Fe-N bond distance [Å]	2.062, 2.056, 2.059, 2.055	1.977, 1.973, 1.974, 1.970	1.994, 1.999, 1.990, 1.993
N-Fe-N bond angle [°]	90.0, 90.2, 89.5, 90.3	90.1, 90.2, 89.6, 90.3	89.9, 90.3, 89.7, 90.2
Total dipole moment [Debye]	7.39	6.98	7.05
Total single point energy [eV]	-84298.21	-84298.59	-84297.96

The coordination of iron in FePPIX chloride/ FePPIX varying with different spin configurations according to the B3LYP/def2-TZVP(-f)/def2-TZV/J unrestricted open shell DFT optimization calculations.

8.3 Iron d-Orbital Characters in FePPIX-Cl

No.	Energy [eV]	Atomic contribution	Fe 3d orbital contribution
171	-8.38	N 19.0%, Fe 74.3%	73.4% d_{x2-y2}
170	-8.74	N 8.2%, Fe 72.0%, Cl 12.8%	69.2% d_{z2}
169	-10.37	N 4.1%, Fe 86.3%, Cl 6.7%	83.1% d_{xz}
168	-10.39	N 4.0%, Fe 86.4%, Cl 6.7%	83.9% d_{yz}
167	.11.70	N 1.2%, Fe 97.6%	96.6% d_{xy}
165	-5.84	N 8.8%, Fe 3.3%, Cl 1.3%	2.7% d_{z2}
161	-6.98	N 23.5%, Fe 5.1%, Cl 5.6%	3.2% d_{z2}
157	-7.94	N 3.1%, Fe 11.1%, Cl 61.3%	6.4% d_{xz} , 3.1% d_{yz}
155	-7.98	N 3.0%, Fe 7.3%, Cl 36.5%	2.3% d_{xz} , 4.0% d_{yz}
152	-9.01	N 32.4%, Fe 6.2%	0.9% d_{xz} , 2.4% d_{yz}
151	-9.04	N 16.7%, Fe 4.5%	1.4% d_{xz} , 1.1% d_{yz}
147	-9.25	N 10.0%, Fe 7.8%	7.5% d_{x2-y2}
146	-9.41	Fe 24.8%, Cl 72.8%	20.1% d_{z2}

Shown are the characters of MOs of the single-point DFT calculations illustrating the mixing of the iron d-orbitals in FePPIX Chloride as inferred from restricted open-shell single-point DFT calculation, combined with Löwdin population analysis.

8.4 Iron d-Orbital Plots of FePPIX-Cl

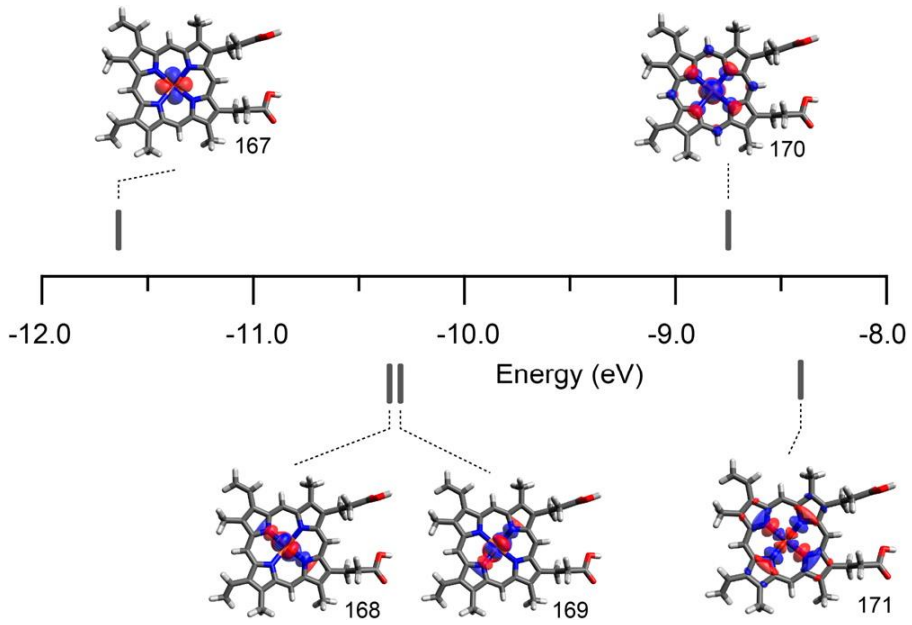

Presented are the Fe 3d-orbitals of FePPIX chloride with S = 2.5 according to the B3LYP/def2-TZVP(-f)/def2-TZV/J restricted open-shell single-point DFT calculation.

8.5 Inner Valence Orbital Plots of FePPIX-Cl

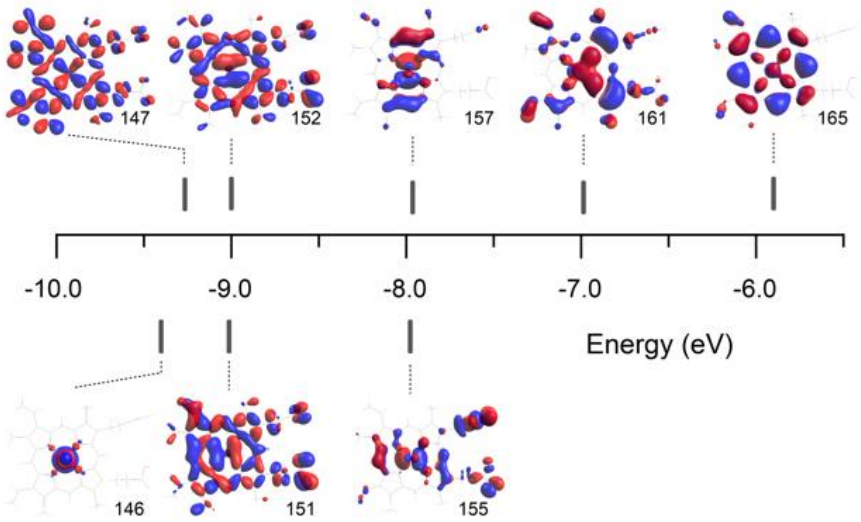

Shown are the inner valence molecular orbitals of FePPIX chloride (in high spin configuration, S=2.5) with prominent Fe contribution (refer to table under 8.3) according to the B3LYP/def2-TZVP(-f)/def2-TZV/J restricted open shell single point DFT calculation.

8.6 Molecular Geometry Variations of CoPPIX-Cl

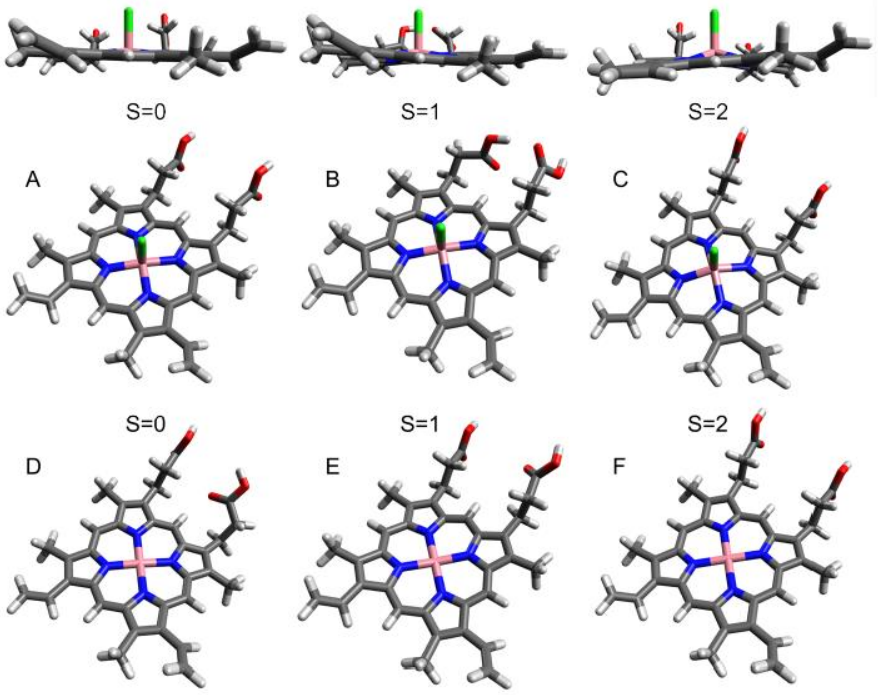

Molecular geometries of Co(III) protoporphyrin IX with (A-C) and without (D-F) a chloride bound to the cobalt center. Spin states are: S=0 (A), S=1 (B), S=2 (C), S=0 (D), S=1(E), S=2 (F).

8.7 Bond Lengths and Angles of CoPPIX-Cl for different Spin States

	CoPPIX-Cl S = 2	CoPPIX-Cl S = 1	CoPPIX-Cl S = 0
Co-Cl bond distance [Å]	2.225	2.303	2.201
Co-N bond distance [Å]	2.101, 2.087, 2.093, 2.082	2.003, 2.008, 1.994, 2.003	1.994, 1.995, 1.989, 1.992
Cl-Co-N bond angle [°]	104.9, 102.3, 106.7, 104.7	93.6, 99.3, 95.4, 101.2	93.8, 95.2, 95.8, 96.7
N-Co-N bond angle [°]	86.4, 86.4, 86.1, 86.5	89.3, 89.2, 89.1, 89.2	89.6, 89.5, 89.3, 89.6
Total dipole moment [Debye]	1.14	3.69	1.38
Total single point energy [eV]	-100065.96	-100066.18	-100066.12

The coordination of cobalt in CoPP-IX chloride varying with different spin configurations according to the B3LYP/def2-TZVP(-f)/def2-TZV/J (un)restricted (open shell)DFT optimization calculations.

8.8 Inner Valence Orbital Plots of CoPPIX-Cl

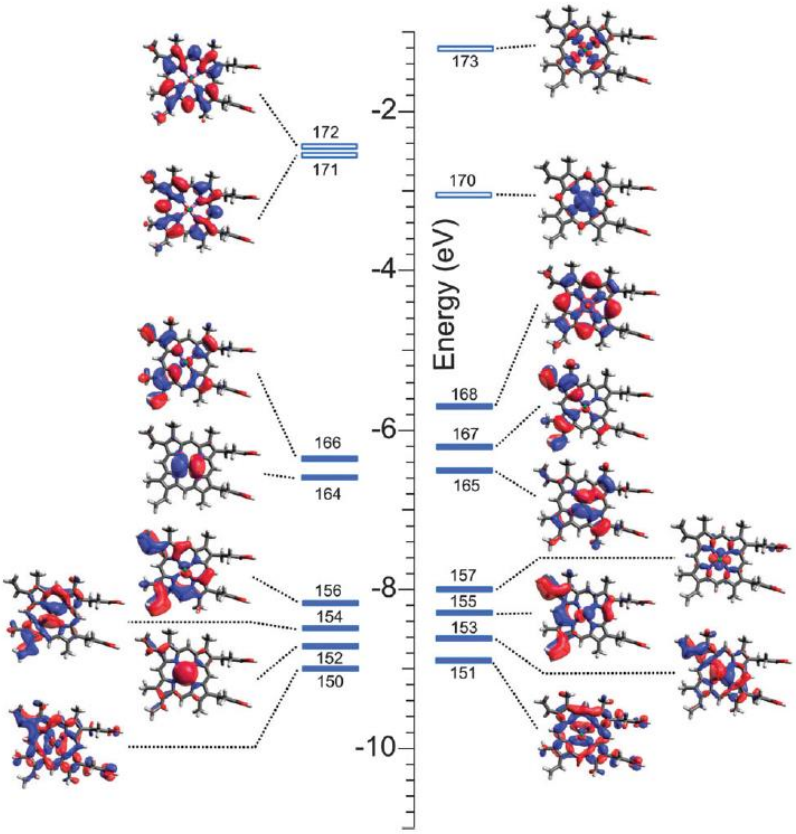

Shown are the calculated valence orbitals (and their energies) with significant Co contributions for CoPPIX-Cl in the ground state for 5-coordination, and lowest-spin, S = 0, as obtained from the restricted closed shell single point DFT calculations.

8.9 DMSO Coordination towards CoPPIX-Cl

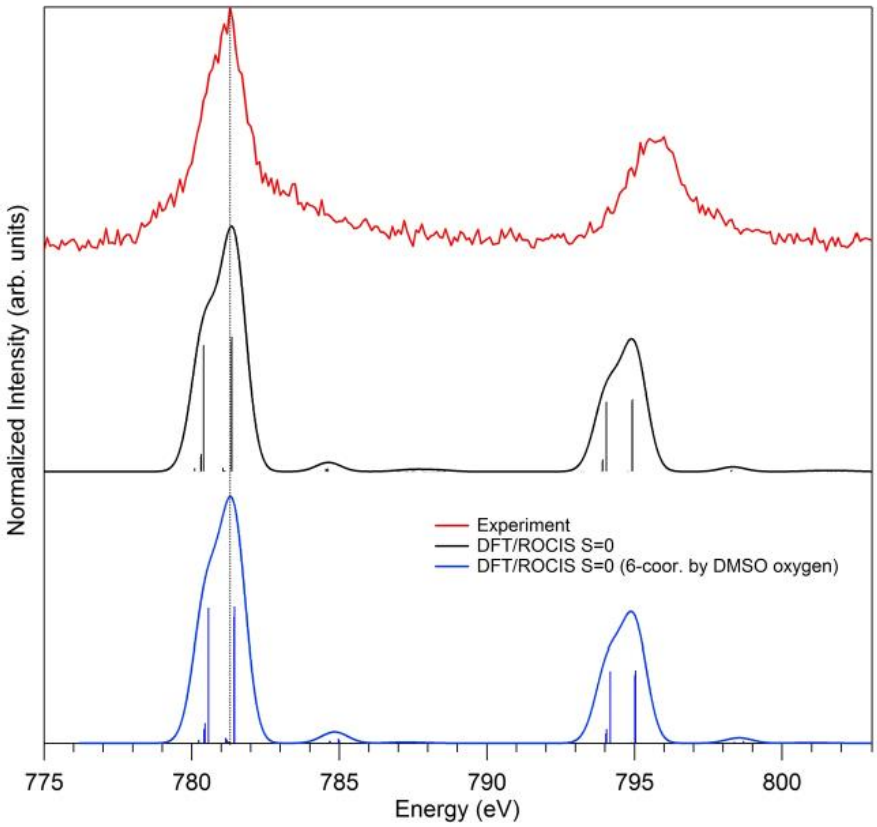

Experimental Co L edge PFY spectrum of 50 mM CoPPIX chloride solution in DMSO and DFT/ROCIS XA calculations for spin S = 0 for the 5- and 6-coordinated species. The 6th coordination is provided by the oxygen atom of dimethyl-sulfoxide. The computed spectra are shifted *ad hoc* by 16.35 eV (black trace) and 16.2 eV (blue trace).

8.10 Bond Length and Angles of MnOEP-Cl and MnTPP-Cl

	MnOEP S = 2	MnTPP S = 2
Mn-N bond distance [Å]	2.005, 2.006, 2.006, 2.006	2.000, 2.000, 2.000, 2.002
N-Mn-N bond angle [°]	90.0, 90.0, 90.0, 90.0	90.1, 90.0, 90.0, 89.9

Shown are the Mn-N bond lengths and bond angles of the MnOEP and MnTPP gas phase after the geometry optimizations for the molecular configuration of high spin S = 2 with Cl detached.

8.11 Atomic and 3d-Orbital Contributions in FeTPP-Cl and FeOEP-Cl

No.	Occupation	Energy [eV]	Atomic contribution	Fe 3d orbital contribution
FeOEP-Cl				
167	1	-8.1309	N 19.2, Cl 0%, Fe 74.2%	d_{x2-y2} 74.1%
166	1	-8.527	N 8.4%, Cl 12.6%, Fe 72.2%	d_{z2} 70.2%
165	1	-10.1501	N 4.2%, Cl 6.6%, Fe 86.5%	d_{xz} 29.5%, d_{yz} 56.5%
164	1	-10.1501	N 4.2%, Cl 6.6%, Fe 86.5%	d_{xz} 56.5%, d_{yz} 29.5%
163	1	-11.4604	N 1.2%, Cl 0%, Fe 97.6%	d_{xy} 97.5%
161	2	-5.5997	N 10.4%, Cl 1.5%, Fe 4.7	d_{z2} 3.2%
157	2	-6.8541	N 24.8%, Cl 1.4%, Fe 6.6	d_{z2} 4.1%
154	2	-7.708	N 3.4%, Cl 68%, Fe 12.7%	d_{xz} 1.7%, d_{yz} 9.3%
153	2	-7.7081	N 3.4%, Cl 68%, Fe 12.7%	d_{xz} 9.3%, d_{yz} 1.7%
152	2	-8.6881	N 29%, Cl 0.2%, Fe 7.6%	d_{xz} 2.9%, d_{yz} 1.4%
151	2	-8.6882	N 29%, Cl 0.2%, Fe 7.6%	d_{xz} 1.4%, d_{yz} 2.9%
149	2	-8.8861	N 8%, Cl 0%, Fe 7.6%	d_{x2-y2} 7.6%
147	2	-9.1554	N 1.2%, Cl 72%, Fe 24.8%	d_{z2} 13.3%
FeTPP-Cl				
183	1	-8.3221	N 19.2, Cl 0%, Fe 74.3%	d_{x2-y2} 74.2%
182	1	-8.6272	N 8.4%, Cl 12.8%, Fe 71.2%	d_{z2} 69.3%
181	1	-10.3594	N 4%, Cl 6.5%, Fe 86.8%	d_{xz} 42.8%, d_{yz} 43.6%
180	1	-10.3596	N 4%, Cl 6.5%, Fe 86.8%	d_{xz} 43.6%, d_{yz} 42.8%
179	1	-11.6506	N 1.2%, Cl 0%, Fe 97.6%	d_{xy} 97.5%
177	2	-5.6544	N 10%, Cl 1.9%, Fe 5.9%	d_{z2} 4.3%
165	2	-7.4295	N 26.4%, Cl 1.2%, Fe 5.8%	d_{z2} 3.5%
162	2	-7.9531	N 4%, Cl 64.4%, Fe 13.5%	d_{xz} 11.8%
161	2	-7.9532	N 4%, Cl 64.4%, Fe 13.5%	d_{yz} 11.8%
159	2	-9.1559	N 40.9%, Cl 0.2%, Fe 9.7%	d_{xz} 2.9%, d_{yz} 2.4%
158	2	-9.1571	N 40.8%, Cl 0.2%, Fe 9.6%	d_{xz} 2.4%, d_{yz} 2.9%
157	2	-9.3488	N 1.2%, Cl 73.3%, Fe 24.9%	d_{z2} 20.4%
FeOEP-Cl$_2$				
176	1	-4.7553	N 18.8%, Cl 0%, Fe 75.1%	d_{x2-y2} 75.1%
175	1	-4.7677	N 5.6%, Cl 22.5%, Fe 70.4%	d_{z2} 70.2%
174	1	-7.4055	N 1.4%, Cl 6%, Fe 90.7%	d_{xz} 40%, d_{yz} 50.6%
173	1	-7.4056	N 1.4%, Cl 6%, Fe 90.7%	d_{xz} 50.6%, d_{yz} 40%
172	1	-8.2698	N 1.6%, Cl 0%, Fe 97.5%	d_{xy} 97.4%
163	2	-4.2624	N 12.2%, Cl 29.5%, Fe 12.4%	d_{xz} 9.2%, d_{yz} 3.1%
162	2	-4.2624	N 12.1%, Cl 29.5%, Fe 12.4%	d_{xz} 3.1%, d_{yz} 9.2%
158	2	-5.4429	N 1.2%, Cl 68.1%, Fe 30.2%	d_{z2} 28.1%
154	2	-6.2139	N 13.6%, Cl 0%,Fe 12.1%	d_{x2-y2} 12.1%

Atomic (Fe and its closest ligand atoms) and Fe 3d orbital contributions to each molecular orbital of FeTPP-Cl, FeOEP-Cl and FeOEP-Cl_2 complexes with high spin multiplicity 2s+1 = 6. The first column is just the numbering used in ORCA program for labeling orbitals. Occupation in the second column means the amount of electrons on each orbital: 2 means doubly occupied and 1 singly occupied. The singly occupied orbitals correspond to the vertical bars in Figure 48c and Figure 48**Error! Reference source not found.**f. Those vertical bars represent the transition oments of the Fe 2p core levels to the singly occupied valence orbitals. For doubly occupied orbitals, only those with significant Fe atomic contributions are presented here. Energy levels and atomic/orbital contributions are calculated by restricted open-shell single point DFT after the geometry optimization for each molecule.

8.12 Singly Occupied Molecular Orbitals of FeTPP-Cl and FeOEP-Cl

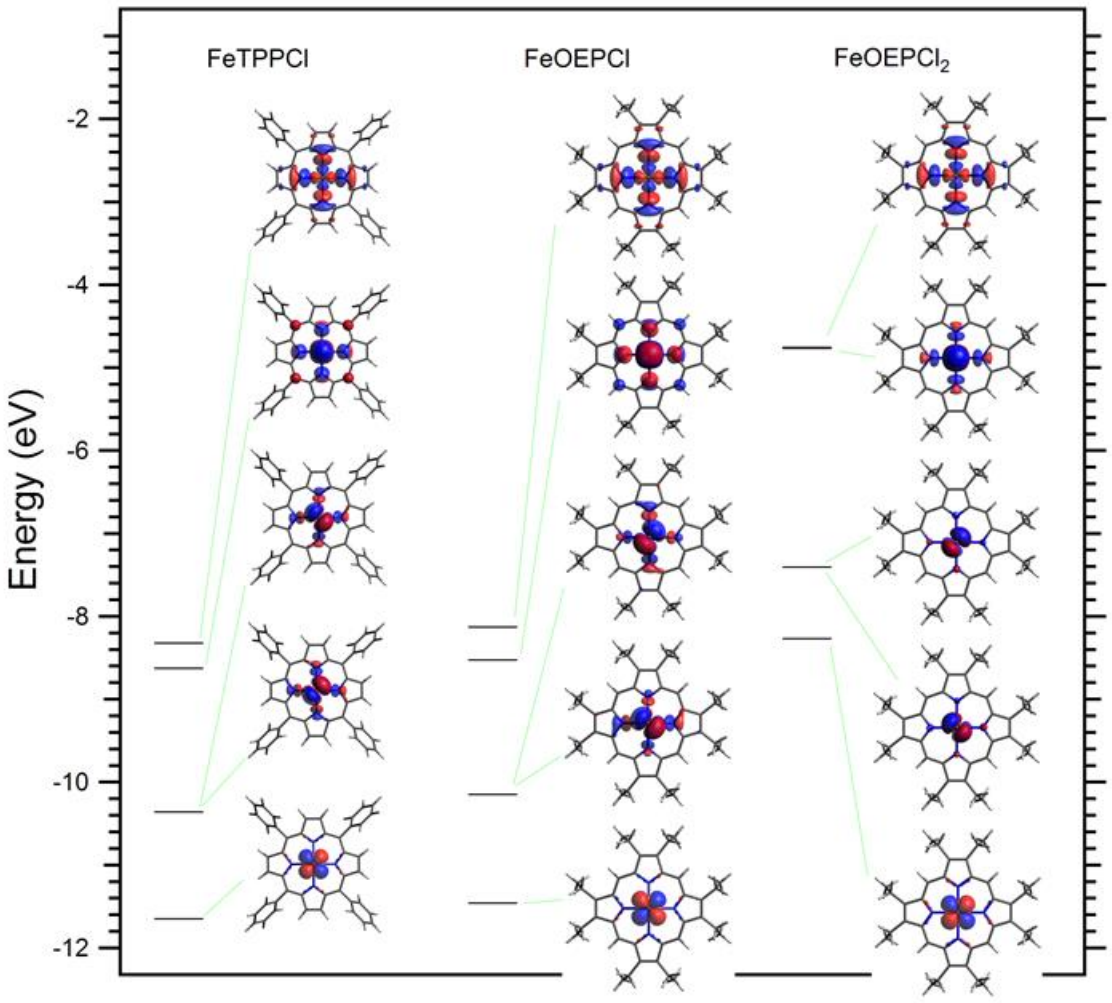

Figure 50. Singly occupied molecular orbitals of FeTPP-Cl (left), FeOEP-Cl (middle) and FeOEP-Cl_2 (right). Energy levels are extracted from the table in appendix 8.11 and represented by horizontal bars. The detailed property of each molecular orbital is in the table in appendix Atomic and 3d-Orbital Contributions in FeTPP-Cl and FeOEP-Cl, too.

8.13 Flow Cell Drawing

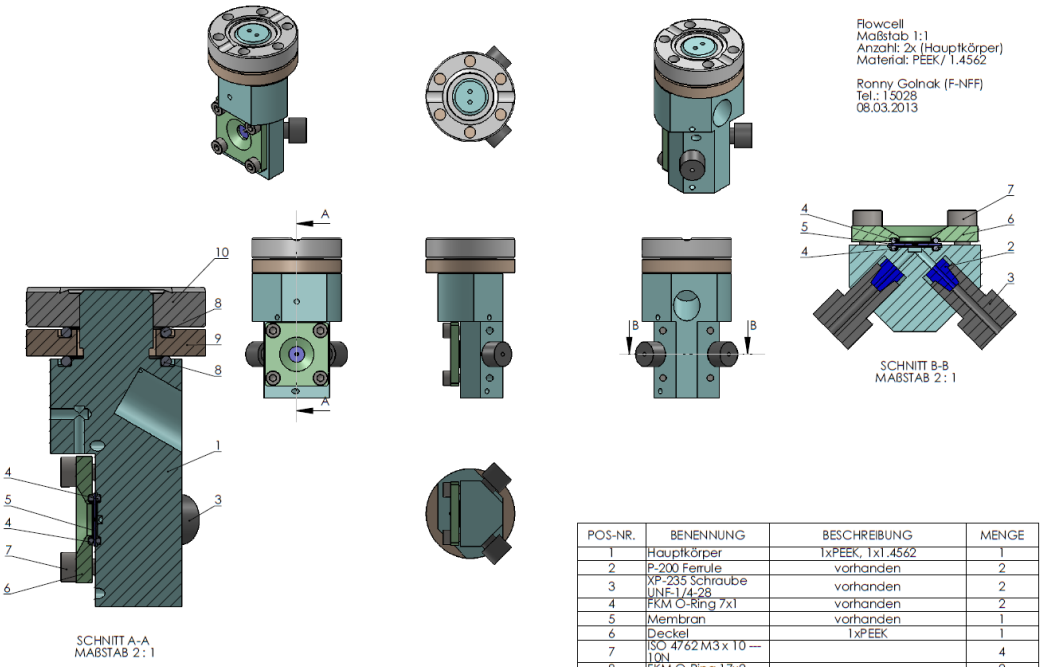

POS-NR.	BENENNUNG	BESCHREIBUNG	MENGE
1	Hauptkörper	1xPEEK, 1x1.4562	1
2	P-200 Ferrule	vorhanden	2
3	XP-235 Schraube UNF-1/4-28	vorhanden	2
4	FKM O-Ring 7x1	vorhanden	2
5	Membran	vorhanden	1
6	Deckel	1xPEEK	1
7	ISO 4762 M3 x 10 --- 10N		4
8	FKM O-Ring 17x2		2
9	Distanzstück	1xPEEK	1
10	DN 16 BF	vorhanden	1

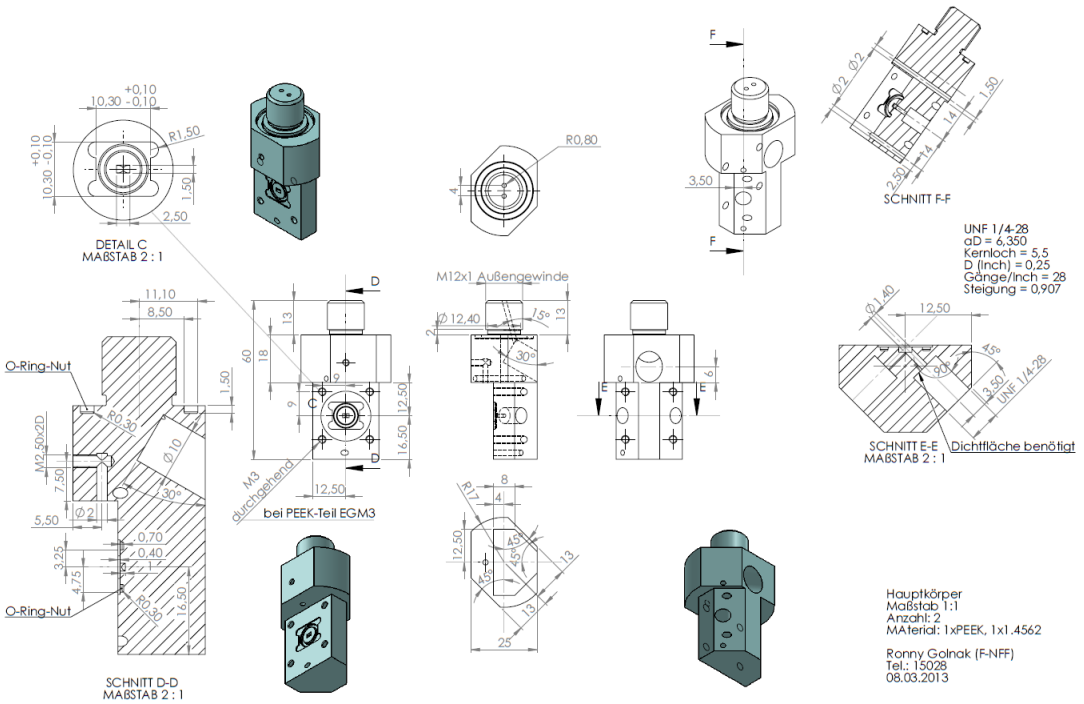
DETAIL C
MAßSTAB 2 : 1
R0,80
SCHNITT F-F
UNF 1/4-28
aD = 6,350
Kernloch = 5,5
D (Inch) = 0,25
Gänge/Inch = 28
Steigung = 0,907
M12x1 Außengewinde
O-Ring-Nut
O-Ring-Nut
M3
durchgehend
bei PEEK-Teil EGM3
SCHNITT D-D
MAßSTAB 2 : 1
SCHNITT E-E
MAßSTAB 2 : 1
Dichtfläche benötigt
Hauptkörper
Maßstab 1:1
Anzahl: 2
MAterial: 1xPEEK, 1x1.4562
Ronny Golnak (F-NFF)
Tel.: 15028
08.03.2013